# Device Modeling and Characterization for CIGS Solar Cells

A DISSERTATION
SUBMITTED TO THE FACULTY OF THE GRADUATE SCHOOL
OF THE UNIVERSITY OF MINNESOTA
BY

Sang Ho Song

IN PARTIAL FULFILLMENT OF THE REQUIREMENTS
FOR THE DEGREE OF
DOCTOR OF PHILOSOPY DOCTOR

Stephen A. Campbell, Adviser

June, 2013

**Acknowledgements**

I would like to express my deepest gratitude to those who contribute, encourage and support me and my works for my entire doctoral degree periods.

First of all, I would like to thank sincerely to advisor, Professor Stephen A. Campbell. Without his deep understanding, hearty advice, persistent encouragement, and strong support, I could not complete this long journey.

I would like to thank to professor Eray S. Aydil for his detailed advice, reviews and comments on research. And I would like to also thank professor Paul P. Ruden, professor Bethanie J. Hills Stadler for their in-depth reviews and comments on this thesis. I would like to also thank to professor Sang-Hyung Oh for having served in my preliminary oral examination as a committee member.

I would like to thank to our former our group members. With Dr. Richard Liptak, we shared the longest time in Campbell group. He always enjoys helping someone unconditionally. I am also one of whom are indebted to him and express my gratitude to him. I am grateful to Dr. Maryam Jalali-Mousavie. Her warm heart and kindness support me to complete my Ph. D. I also would like to thank to Dr. Dan Yu and Gagan Aggrawal. I am grateful our group members, Forrest Johnson, Liyuan Zhang, Brian Benton, and Mandip Sibakoti. I wish all to finish their graduate terms successfully. I would like to thank to Dr. An-Jen Cheng and Dr. Sreejith Karthikeyan, post doctorate researchers, for valuable discussions.

I would like to special thank to Dr. Rebeccah Feist for allowing a chance to study CIGS solar cells and supporting on do research.

I am very grateful to Dr. Min-Woo Jang and Jun-Young Lim. We shared not only knowledge and experience but also difficulties and challenge. They helped and supported me a lot when I was in difficulty. I would like to thank to Mr. Brijesh Kumar. He is a good colleague, friend and teacher. I could learn and improve myself with him. I would like to thank Dr. SeongHo Jeong for his help for setup and thermal admittance spectroscopy measurement.

I am very grateful to Dr. Sukgeun Choi and his family. Without his help and care, I could not settle down in Minnesota and it was very valuable for my research to discuss and share the knowledge. I especially thank to Dr. Kang-Hyun Baek, Dr. Woo-Bin Song and their family for their kindness, support and encouragement. I would like to thank to Dr. Dongjin Lee for his kindness and support. I also thank to Dr. Hyun Chul Jang for his help to settle down in Minnesota.

I would like deeply thank to Dr. Dong-Myong Kim. Without his dedicated support and everlasting encouragement, I could not be here and finish my doctoral degree.

Finally, most of all, I would like to express my sincere gratitude to my parents and bothers. They always understand and encourage me for all my life and

This work was partially supported by Dow Chemical, Initiative of Renewable Energy and the Environment program of University of Minnesota and the sunshot initiative program supported by Department of Energy.

**Sang Ho Song**

**Dedication**

To my parents and brother

for their unconditional supports, continuous encouragements, and devoted love.

**Abstract**

We studied the way to achieve high efficiency and low cost of $CuIn_{1-x}Ga_xSe_2$ (CIGS) solar cells. The Fowler–Nordheim (F-N) tunneling currents at low bias decreased the shunt resistances and degraded the fill factor and efficiency. The activation energies of majority traps were directly related with F-N tunneling currents by the energy barriers. Air anneals decreased the efficiency from 7.74% to 5.18% after a 150 $^oC$, 1000 hour anneal. The decrease of shunt resistance due to F-N tunneling and the increase of series resistance degrade the efficiencies of solar cells. Air anneal reduces the free carrier densities by the newly generated Cu interstitial defects ($Cu_i$). Mobile $Cu_i$ defects induce the metastability in CIGS solar cell. Since oxygen atoms are preferred to passivate the Se vacancies thus Cu interstitial defects ($Cu_i$) explains well metastability of CIGS solar cells.

Lattice mismatch and misfit stress between layers in CIGS solar cells can explain the particular effects of CIGS solar cells. The misfits of 35.08$^o$ rotated (220/204) CIGS to r-plane (102) $MoSe_2$ layers are 1% ~ -4% lower than other orientation and the lattice constants of two layers in short direction are matched at Ga composition x=0.35. This explains well the preferred orientation and the maximum efficiency of Ga composition effects. Misfit between CIGS and CdS generated the dislocations in CdS layer as the interface traps. Thermionic emission currents due to interface traps limit the open circuit voltage at high Ga composition. The trap densities were calculated by critical thickness and dislocation spacing and the numerical device simulation results were well matched with the experimental results.

A metal oxide broken-gap p-n heterojunction is suggested for tunnel junction for multi-junction polycrystalline solar cells and we examined the characteristics of broken-gap tunnel junction by numerical simulation. Ballistic transport mechanism explains well I-V characteristics of broken-gap junction. P-type $Cu_2O$ and n-type $In_2O_3$ broken-gap heterojunction is effective with the CIGS tandem solar cells. The junction has linear I-V characteristics with moderate carrier concentration ($2\times10^{17}$ $cm^{-3}$) and the resistance is lower than GaAs tunnel junction. The efficiency of a CGS/CIS tandem solar cells was 24.1% with buffer layers. And no significant degradations are expected due to broken gap junction.

## Table of Contents

## List of Tables

## List of Figures

# Chapter 1

# Motivation

### 1.1. Energy consumption and global warming in the 20$^{th}$ century.

The industrial revolution has brought about not only an explosion in world population but also in energy consumption per capita. The total energy consumption of the world has increased by almost a factor of twenty since the industrial revolution [1-3]. Biomass, which was a major established energy source before the industrial revolution, including woods and grasses could not satisfy this rapid increase in energy consumption. Thus, new high energy density sources were highly required to fill the gap between supply and consumption, with the major energy sources moving from biomass to fossil fuels including coal. The improvement of mining technology accelerated this movement in 19$^{th}$ century [3]. In the early 20$^{th}$ century, crude oil and natural gas were also developed. Because of their higher energy density than coal and their ease of portability, oil and natural gas become the major energy sources in the world. Fossil fuels have been the dominant sources of energy from late 18$^{th}$ century onward. They cover over 80% of energy consumption not only in United States but also in the world in 2011 [3,4]. This excessive reliance on fossil fuels raises serious economic and environmental problems in 21th century, however.

Reservoirs of most fossil fuels are located underground in limited areas and in limited quantities. In spite of continuous exploration for deposits, these fuels will be depleted someday. Although the technology for the development of fossil fuel exploration has improved, their exploration is still costly, risky, and requires long time horizons, even if sophisticated geophysical survey and drilling or mining processes are used. Hence the supply of fossil fuel is unlikely to increase within a short period of time. For example, the production of crude oil increased only 40% from 1973 to 2011.I In the case of natural gas, production increased 2.7 times in same period due to the development in new areas such as Asia, Africa, the Middle East and Russia.

Until early 2000, the supply chain of fossil fuels – exploitation, development and mass production - satisfied the increase in demand for energy and the balance between supply and consumption makes fossil fuels an affordable energy source. However, from 2002 onward, economic development in China and other developing countries has increased energy consumption. This unexpected increase of consumption has broken the balance between supply and consumption of energy. As a result, energy prices have increased steeply. Oil and natural gas prices increased by a factor of five inform 2002 to 2008. The average price of crude oil reached historical records in 2008 [5]. Hence fossil fuels are not affordable anymore and, therefore, other affordable and sustainable energy sources are highly required.

The dramatic increase of fossil fuel consumption in the 20$^{th}$ century has also led to environmental concerns including global warming [6]. The earth gets most of its energy from the sun. The average temperature in the atmosphere stays stable when the

absorbed solar energy in the earth is balanced with radiated energy from the earth. However, energy that is normally emitted from the earth is captured in the atmosphere then the atmosphere stores solar energy and the temperature of the atmosphere increases. The global warming is suspected by the increase of greenhouse gas (GHG) concentration in the atmosphere [6]. Greenhouse gases are the gases which can absorb and store solar energy. These include water vapor ($H_2O$), carbon dioxide ($CO_2$), ozone ($O_3$), nitrous oxide ($N_2O$), methane ($CH_4$), chlorofluorocarbons (CFC) and etc. The increase of GHG concentration can capture the more solar energy in atmosphere and this increases the temperature of atmosphere.

The global warming melts the ice in the North Pole so that average sea levels in the world increase. According to the survey of United Nations, 10~23% population of the world lives within 100 km from the coast thus sea level elevation make large population of peoples be endanger [7]. And the global warming affects the climate directly. Climate change makes weather more unpredictable and increases the chance of climate disaster such as hurricane and drought. Therefore, there is a world-wide effort to reduce the global warming [8,9], especially by reducing GHG emissions. Among the GHGs, the significant increase of concentration in the atmosphere is $CO_2$ and about 56% of $CO_2$ is generated by fossil fuel consumption [6]. Thus, further increases in $CO_2$ emission should be minimized if at all possible, clearly and low GHG emission energy sources are more highly required than ever. Nuclear energy was a primary candidate as a replacement energy source however, after the Fukushima nuclear accident in 2011, the stability and

safety of nuclear energy have become big issues and many countries are trying to reduce the number of nuclear plants [10,11].

From the problems described above, new energy sources which are

- low GHG emissive,
- sustainable,
- safe and stable,
- eco-friendly

are highly desired. Renewable energy becomes the best energy source which satisfies above requirements if solutions can be found to overcome problems associated with its production, distribution, and usage.

**1.2. Renewable energies.**

To be commercially valuable, the renewable energy restoration cycle should be short and any byproducts of the energy harvesting process must decompose in the natural cycle within a short time so that the effects on nature are minimized. Solar, biopower, geothermal, hydropower, wind and ocean energies are considered as major renewable energy sources [12].These renewable energies are the part of various natural energy cycles so they have particular characteristics and developed for specific applications due to their characteristics.

The common pros of renewable energy are sustainability and low GHG emissions. And, the biggest common con is the expense of energy generation for sources other than hydropower since renewable energy technologies are not matured as much as fossil fuels

technology. Hydorpower is an attractive economical renewable energy source however it is not safe against natural disaster and the impacts on the environment must be considered. The supply of hydropower is expected to increase only slightly in spite of low generation cost and $CO_2$ emission [ 13 ]. The ocean power also has the serious impacts on environment and the technology is not proven in commercial-scale applications. Wind can be an unstable energy source. Geothermal energy is stable, but the energy source is primarily located near volcanic belts, generally far from population centers.

On the contrary, solar energy can be used in most places on the earth and it has few impacts on the environment. The solar energy systems have well proven safety and survivability against hurricanes such as Sandy and Katrina. One obvious disadvantage of solar energy is that it is available primarily in daytime and depends on cloud cover. However the daily electricity consumption cycle matches the daily electricity generation of solar cells. Thus solar is a power choice for an exclusive source of power, but can be a very good choice as one of a portfolio of energy sources.

Table 1.1. Theoretical and technical estimates of renewable energy in the earth.

| | Geothermal (Electricity) | Hydro | Ocean | Wind | Geothermal (Heat) | Biomass | Solar |
|---|---|---|---|---|---|---|---|
| Theoretical [EJ/yr] | | 147 | | 6,000 | | 2,900 | 3,900,000 |
| Tech. Max [EJ/yr] | 1,109 | 52 | 331 | 580 | 312 | 500 | 49,837 |
| Tech. Min [EJ/yr] | 118 | 50 | 7 | 85 | 10 | 50 | 1,575 |

Considering the available amount of energy in nature, solar energy has the largest energy capacity among the other renewable sources as shown in Table 1.1. Theoretically, about 3,900,000 exajoule ($\times 10^{18}$J; EJ) /yr of solar energy is absorbed in the earth. About 2900 EJ/yr out of the absorbed solar energy is transferred to biomass energy and about 6000 EJ/yr generate wind energy. Ideally, this amount of renewable energy is enough to supply the world energy consumption but the technically available amount is much less than the theoretical amount. Nevertheless, the minimum technically available amount of solar energy is about 1575 EJ/yr. Considering the world-wide energy supply (492 EJ/yr) in 2008, any other renewable energy sources cannot satisfy this requirement except solar energy [14].

Renewable energies are not a big portion of the world energy supply at about 16.7% in 2010. About half (8.5%) is primary biomass such as wood and charcoals, while 3.3% is hydropower. These two are the dominant renewable sources in the energy supply [15]. The share of modern renewable energy such as wind and solar cells is 4.9%. Since 2007, the global energy shortage has increased the cost of fossil fuels and accelerated the renewable energy use, increasing the share of renewable energy from 12.9% in 2008. The share of solar energy in world energy supply is about 0.1%, however its rate of growth in the energy supply is the highest among renewable energy sources. It expanded by 74% grows in 2010 and is expected to the fastest-growing source of renewable energy in future. The major obstacle to the rate of expansion is the expense of power generation in these alternative technologies.

### 1.3. Solar cells.

Solar cells (SC) are the electrical devices which convert light energy to electric energy directly using the photovoltaic effect. In this effect, free carriers are generated inside materials when they are illuminated. Solar cells generate power by collecting these photo-generated carriers and delivering them at a potential difference. Thus, the photoelectric material that absorbs photons and generates electrons and holes, either free or paired in an exciton, play a key role in solar cells. In most solar cells, light absorbing material is a semiconductor. The energy conversion efficiency is determined by the ratio of electric generation power to illuminating solar powers. To obtain a high energy conversion efficiency, most of the photo-generated carriers must be collected. A common carrier loss mechanism is carrier recombination by defects. Therefore, materials with a low defect density and high carrier mobility are strongly preferred. However, high quality materials tend to be expensive. Thus a trade-off exists between quality and cost.

Table 1.2. Advantages and disadvantages of solar cells

| Advantages | Disadvantages |
|---|---|
| • Infinite energy source<br>• No emission and or noise<br>• Low maintenance cost<br>• Scalable size<br>• High endurance and reliability (>25 yrs)<br>• Quick installation<br>• Off power grid capability<br>• Safety | • Low density energy source<br>• High initial investment cost<br>• Work only during the day<br>• Power varies with cloud cover, angle of the sun, obstacles such as snow<br>• Encapsulation requirement<br>• Poor power grid infrastructure |

The advantages and disadvantages of solar cells are summarized in Table 1.2. No GHG emissions in operation, eco-friendly and infinite large amount of energy are the major merits. Also, solar cells can be installed in areas that are isolated from the power grid. Most of the drawbacks relate to high costs, both in initial investment and in energy generation. Many countries have used incentive plans and research programs to reduce the cost and to promote the use of solar energy. In United States, the Department of Energy (DoE) instiuted the Solar America Initiative (SAI) and the SunShot Initiative to promote cost reduction in photovoltaic energy.

### 1.3.1. Energy generation costs of solar cells.

The cost of electricity generation for solar cells is defined by the ratio of the total life cycle cost to the total energy generation costs. This produces the lifetime levelized cost of electricity (LCOE) [16].

LCOE is calculated as

$$LCOE = \frac{\sum_{t=1}^{n} \frac{I_t + M_t + O_t + F_t}{(1-r)^t}}{\sum_{t=1}^{n} \frac{E_t}{(1-r)^t}} \text{ [\$/kWh]}, \tag{1-1}$$

where, $t$ is time (in years), $n$ is lifetime (in years), $I_t$ is initial investment cost, $M_t$ is the maintenance cost, $O_t$ is the operation cost, $F_t$ is financial cost such as interest, $r$ is the discount rate and $E_t$ is the energy production per unit time (years). Various factors such as financial costs, the installation location, and the availability of tax credits can strongly affect the LCOE.

According to an analysis by the United States (US) Department of Energy (DoE), the LCOE of fossil fuel plants entering service 2017 in the US range from 6.31 cents/kWh to 13.9 cents/kWh depending on the energy source and technology [13]. In contrast, the LCOE of solar cells is expected about 15.3 cents/kWh. Recent efforts to reduce the price have met with some success; the LCOE of solar has decreased to 14~16 cents/kWh in 2010, however it is still almost twice as high as the lowest cost fossil fuel - natural gas. Thus, further reductions in cost are required for solar energy production to become widespread.

From equation (1-1), the potential methods to reduce the LCOE are

- Reducing the initial investment cost,
- Increasing the energy production, and
- Increasing the lifetime of solar cells.

There are various ways to understand the cost distribution. One that is useful is to divide costs into the cost of the solar modules (on which the solar cells are mounted) themselves, and everything else. The latter is called the balance of system (BOS). BOS costs can include installation, land acquisition, the power system including inverters, controls, and cables, and solar tracking, if used [17]. The module cost is about from 50% to 72% of total installed costs and the cell cost is about 60% of module costs on average in 2011 [18]. It is important to note that many of these costs (installation, land, some of the power components, and tracking) scale with the number of modules installed, not the power generated. Thus, while low cost solar cells are helpful, high efficiency cells that can be

delivered at low cost can dramatically reduce the LCOE of solar cells, particularly is lifetimes can be pushed to 50 years or more.

### 1.3.2. Solar cell technologies and generations.

Since the energy generation cost is the most important metric in solar cells, in a classic paper, Green classified solar cells generation in three categories (Figure 1.1) [19]. Even though Green's classification might be less meaningful in the energy generation cost because the differences of energy generation cost between generations are reduced, it is still meaningful in technological classification to understand the limitation of generations.

First generation solar cells are high efficiency, but high cost solar cells. This generation includes single and multi-crystalline Si solar cells. From the beginning Si has been the dominant material in solar cells, currently making up about 80% of solar cells in production. The commercial success of Si based microelectronic technology established a broad and deep industrial infrastructure for the mass production of high quality Si ingots and wafers. Furthermore, silicon is the most heavily studied material in history, providing a deep understanding of the behavior of the material and its defects. Since industrial standard of Si solar cells are almost same with microelectronics industry the size of Si solar cells is limited by microelectronic standards – the maximum size is 12" in diameter. Thus, a module process, making a single panel from many solar cells, is required for large area and high power generation.

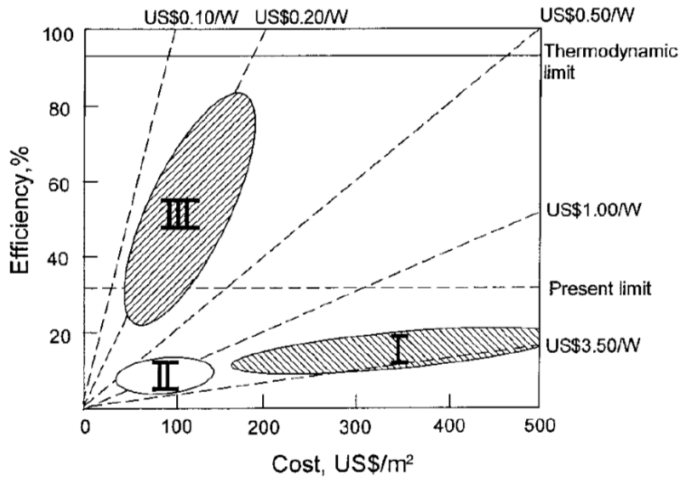


Figure 1.1. Efficiency and cost due to solar cell generations [19].

The maximum efficiencies of single crystal and multi crystalline Si solar cells are 25% and 20.4% respectively [20]. However, the material has several inherent limitations. The material preparation and process fabrication steps of the Si solar cell require very high temperature processes (>1500 $^{o}$C). Since the optical absorption coefficient is low in silicon, thick absorber layers are required. As a result, the total cost of fabricating silicon solar cells is high. This results in the high cost of installed single crystal Si solar cells solar systems, about 3.5 $/W as shown in Figure 1.1 [17].

Second generation solar cells have lower efficiency however their cost is lower than the first generation solar cells. Thus its power generation cost is about 0.5 ~ 1.0 $/W as shown in Figure 1.1. The absorber layers of thin film solar cells are high absorption coefficient semiconductor materials such as CdTe, $CuIn_{1-x}Ga_xSe_2$ (CIGS) and amorphous Si, thus thin absorber layer (<10 μm) are enough to absorb 95% of the solar spectrum. Since the absorber layers are thin, the material costs of thin film solar cells are low; the

module costs with CdTe solar cells is 0.75 $/W in 2011 [21]. The efficiency of the best of these devices is comparable with the efficiency with multi-crystalline Si solar cells; the maximum efficiency of $CuIn_{1-x}Ga_xSe_2$ solar cells is 20.3% [22].

Third generation solar cells provide much lower energy generation cost than second generation cells – about 0.2 $/W - and higher efficiency than the theoretical limit of single junction solar cells. To overcome the theoretical efficiency limit, new concepts and technologies are required. There are multiple concepts that have the potential to push the efficiency higher than theoretical limit of single junction solar cells, however few concepts have been experimentally proven.

The dominant proven third generation technology is the multi-junction solar cell. A multi-junction solar cell uses multiple junctions in semiconductors with different band gaps that are stacked on same area and connected in series electrically. Thus they share the solar spectrum. In single junction solar cells, the energy of photon in excess of the band gap energy is lost as thermal energy as the electron and/or hole relax to the band edge through collisions. As a result, the efficiency of single-junction thin film solar cells is constrained by the Shockley-Queisser limit [23]. In multi-junction solar cells, thermal energy loss is reduced since higher energy photons are absorbed in wider bandgap materials. The problems to be solved in creating a high efficiency multi-junction cell are the efficiency of wide bandgap (top) cell and current matching between solar cells. Currently, multi-junction cells are generally fabricated using hetero epitaxial growth. The device is made by stacking high efficiency single crystal solar cells and interconnection junctions alternately. The current maximum efficiency of a multi-junction solar cell is

43.5% from an epitaxially grown GaInP/GaAs/GaInNAs stack. This efficiency is the highest for any solar cell [20]. However, epitaxial growth is a very expensive process, making the $/watt metric relatively poor for these devices [24]. As a result, multi-junction solar cells are only used in special applications such as aerospace that are not cost sensitive. To reduce the cost while retaining the high efficiency advantage, one can concentrate sun light (concentrated photovoltaics or CPV) systems can be used with multi-junction solar cells. Sun light over a large area is concentrated onto a small, high efficiency multi-junction solar cell. Concentrated solar cells require optical equipments, however the low energy generation costs due to very high efficiency solar cells has the potential to compensate for the added BOS cost, making the LCOE competitive. The LCOE of concentrated solar cells is 12.2~24.9 cents/kWh in 2009, a value close to the LCOE of thin films solar cells [16].

Another potential technology is multiple carrier generation solar cells. As described above, when the energy of the absorbed photon is higher that the band gap, the excess energy is typically lost to heat. In multiple carrier generation solar cells, the absorbed photons can generate multiple electron-hole pairs if the photon energy is sufficient. Multiple carrier generation effects are observed in PbSe nanoparticles. Solar cells made from PbSe nanoparticles show over 100% quantum efficiency in wide band gap range [25]. However, the best reported efficiency for the entire solar spectrum is about 7% in 2012. Thus while the effect has been confirmed the device needs to be improved to become a commercial technology [26].

To summarize, second generation solar cells are the most cost effective however, they have an obvious efficiency limitation. Third generation solar cells have achieved the most efficient solar cells, however their cost of power ($/watt) is unacceptable for most applications since they are the most expensive solar cells. Thus, it is reasonable to attempt to merge two generation solar cells, developing third generation solar cell structures with second generation materials. Such solar cells are of considerable current interest [27,28].

### 1.4. Thin film solar cells and CIGS thin film solar cells.

Although currently a small part of the current PV market, thin film solar cells have very strong potential. They have the lowest cost, high efficiency and are promising for the future of solar [29]. Three materials – CdTe, $CuIn_xGa_{1-x}Se_2$ (CIGS) and amorphous Si – are major semiconductor materials in thin film solar cells. The general structures as well as the advantages and disadvantages of thin film solar cell technologies are shown in Table 1.3.

The oldest technology of the three is hydrogenated amorphous silicon (a-Si). The advantage of this approach is that Si is both nontoxic and one of the most abundant materials on earth. Fabrication processes are compatible with Si microelectronic processes. However, amorphous films are defective, so hydrogen is used to passivate defects. H passivation is not enough to passivate all defects in absorber layer thus the maximum efficiency is only 13.5% in 2012 [20]. Even more critically however, these devices suffer a degradation mechanism that leads to a loss of about 20% of their as-

manufactured efficiency with light exposure. Thus the degraded efficiency is closer to 11%.

Table 1.3. General structures, advantages and disadvantages of thin film solar cell technologies.

| | $CuIn_{1-x}Ga_xSe_2$ | CdTe | Amorphous-Si |
|---|---|---|---|
| General Structure | 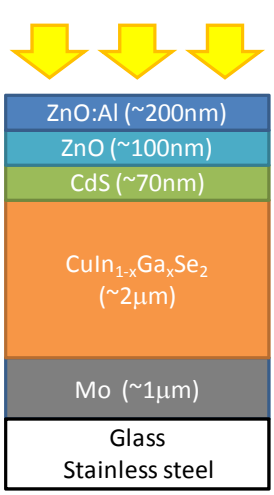 | 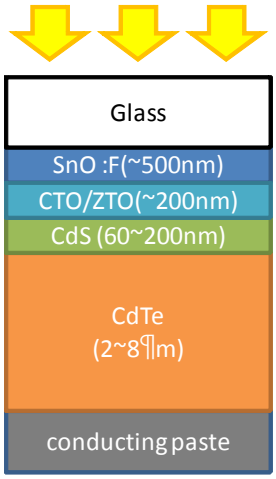 | 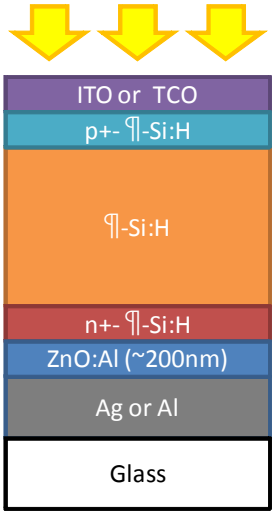 |
| Pros | • High efficiency<br>• Variable bandgap<br>• Low Cd content<br>• Potential for low cost | • Currently in volume production at low cost | • Nontoxic material<br>• Abundant material<br>• Variable bandgap<br>• Multi-junction capability<br>• Compatible with Si process |
| Cons | • In availability | • Cd toxicity<br>• Low efficiency<br>• Te availability | • Low efficiency<br>• Defective absorber<br>• Unstable<br>• Complex process |

The CdTe solar cell is currently the dominant thin film technology. It has the second largest market share after Si solar cells because of its low cost. However it has

several problems. One is the toxicity problems of Cd. It causes serious organ damage and health problems when humans are exposed. Thus CdTe solar cells should be controlled from the very beginning of solar cell production to module disposal. Currently, vendors guarantee the disposal and recycling of CdTe solar cells like Ni-Cd rechargeable batteries, but this guarantee carries some skepticism since the lifetime of solar cells (>25 years) is much longer than the average lifespan of solar companies (~15 years) [30]. In the worst case, abandoned CdTe PV installations may require remediation, a problem reminiscent of today's concerns with asbestos. Another problem of CdTe solar cells is relatively low maximum efficiency compared crystalline Si and CIGS solar cells. The maximum laboratory efficiency of CdTe solar cells is 18.3% in 2012 [20]. Generally, mass produced module efficiencies are about 60% of the best lab device efficiency. (a-Si is a little better due to the maturity of its production.) Even when considering only the production goals, the maximum device efficiency is important since it sets an upper bound on future module production.

$CuIn_{1-x}Ga_xSe_2$ (CIGS) solar cells are known for their high efficiency. First, CIGS is a direct band gap material like other thin film solar cells materials however absorption coefficient is higher than $10^5$ $cm^{-5}$ – this is about 10 times higher than CdTe. Thus more than 90% of solar spectrum can be corrected with less than 2.5 μm of absorber layer while the thickness of CdTe is typically 2 to 8 μm [31]. Second, the band gap can be changed by the composition ratio of In to (In+Ga). from 1.01 eV ($CuInSe_2$) to 1.67 eV ($CuGaSe_2$). And, the compositional change of Ga in absorber layer induces an electric field in charge neutral region of absorber layer. Thus photo-generated electrons and holes

in charge neutral region will drift in opposite directions, improving collection efficiency as well as overall conversion efficiency [32]. The band gap range can be further widened by incorporating other materials such as S and Al [32]. Third, one can obtain a low resistance back contact. During CIGS deposition, a deposited layer of Mo reacts with Se forming $MoSe_2$ at the interface between CIGS and Mo. $MoSe_2$ makes good ohmic contact with CIGS due to its low band gap [32]. Fourth, the Cd content is much less than in CdTe solar cells. CdS is used to form the n-type side of the p-n heterojunction. The thickness of CdS layer, however, is about 70nm, a factor of 100 less than the thickness of typical CdTe absorbers. It is unclear why CdS produces such a high quality p-n heterojunction with CIGS but it significantly improves the efficiency of CIGS solar cells. One of the primary disadvantages of CIGS is the difficulty of manufacture. A quaternary compound, one must develop techniques for controlling composition and morphology in a high-rate production environment.

### 1.5. Thin film multi-junction solar cells.

The multi-junction solar cell is only commercially proven technology capable of overcoming the Shockley-Queisser limit [19]. Thin film multi-junction solar cells are the most promising structures for third-generation photovoltaic (PV) devices because they have the potential to merge the advantages of the low cost of thin films and the high efficiency of multi-junction solar cells in single device [29,33]. However, there are several problems to achieve high efficiency multi-junction solar cells. First, wide band gap (>1.6 eV) thin film solar cells such as $Cu(In_{1-x}Ga_x)(Se_{1-y}S_y)_2$ and $Cu(In_{1-x}Al_x)(Se_{1-}$

$_{y}S_{y})_{2}$ have low generally efficiency. The band gap of CIGS can be an ideal band gap (1.4 eV) for theoretical maximum efficiency however the band gap of maximum efficiency CIGS solar cells is about 1.1 eV. The efficiencies of wide band gap CIGS decrease monotonically above 1.1 eV with increasing band gaps. The total efficiency of multi-junction solar cell is determined by adding full efficiencies of each cell whose short circuit currents are reduced by number of solar cells. Since the efficiency of top solar cells is only the efficiency under full solar spectrums and the efficiencies of other solar cells are the efficiency under partial solar spectrum, thus the portion of top solar cell in total efficiency is about 66% in tandem solar cells. Thus the efficiency of solar cells of the widest band gap is the most important in multi-junction solar cells. However, wide band gap thin film solar cells have low efficiencies [34]. This problem also inhibits the improvement of efficiency in single junction CIGS solar cell. The second major problem is the interconnection between cells. Each cell should be connected to the next cell in the stack with transparent low resistance contacts. When two solar cells are stacked monolithically, a reverse biased p-n junction forms at the interface between them. Typically, heavily doped p-n tunnel junction (TJ) diodes are used between epitaxially grown solar cells to solve this problem. However, thin film solar cells have a polycrystalline structure making it difficult to sustain the abrupt doping profile needed for a TJ.

The component solar cells in a multi-junction stack should have different band gaps and good efficiency. Since a stacked solar cells share the same solar spectrum, there are optimum band gap combinations to match the short circuit currents of each solar cell.

Comparing thin film materials for multi-junction solar cells, CdTe has only one fixed band gap of 1.4 eV. Thus other solar cells with different band gaps are required to make a multi-junction solar cell. While a 1.4eV band gap is the optimum value for a single junction device and a triple gap device, it is not optimal for the simplest multi junction device: the tandem junction solar cell [35]. Yet, this is almost certainly the first thin film multi junction device to be built.

In contrast, In the CIGS material system one can vary the band gap from 1.01 to 1.67 eV by changing the Ga concentration. In a tandem cell, the optimal band gaps of the top and bottom cell are 0.94 and 1.64 eV under AM 1.5 sun [35]. CIGS comes close to being able to cover this range and also can be used in triple junction cells as well. Thus, CIGS is the preferred choice for the first demonstration of a true thin film multi-junction solar cell.

### 1.6. Outline of thesis.

This review suggests that CIGS is a promising absorber to achieve low cost high efficiency solar cells. The purpose of this work is to investigate the way to achieve low cost, high efficiency and long lifetime of CIGS solar cells, including multi junction CIGS cells.

Chapter 2 presents a study of the performance degradation mechanisms of CIGS solar cells. Even though, CIGS solar cells achieved the highest efficiencies in thin film solar cells, the average efficiency of CIGS solar cells is about 10~12% in mass production. Cost reduction is a key factor in mass production and is one of the factors in

the performance gap between research and mass production results. Thus the performance degradation mechanisms of CIGS solar cells on stainless steel substrates which are supplied by Dow Chemical are presented in chapter 2.

Chapter 3 presents the effect of air annealing on CIGS degradation. An understanding of the performance degradation mechanisms in solar cells is an important first step to extending their lifetime. This chapter studied the degradation mechanisms of CIGS solar cells by air anneal using elevated temperature to accelerate the mechanism.

Chapter 4 details an investigation on heteroepitaxy between layers in CIGS solar cells and its effects on CIGS solar cell performance using device simulation. (220/204) oriented CIGS films show the high efficiencies than other orientations and preferred orientations of CIGS films are related with the orientation of $MoSe_2$. Thus, heteroepitaxy between layers in CIGS solar cells strongly affects on the performance of CIGS solar cell. In this chapter, the lattice mismatch between layers in CIGS solar cells is examined. The modeling of bulk and interface traps due to lattice misfit is performed and the trap effects on solar cell performance are examined by numerical simulation.

Chapter 5 describes a device simulation study of the use of a broken gap junction to make electrical contact between the upper and lower cells of a CIGS tandem solar cell.

And, finally, Chapter 6 concludes this work and provides suggestions for future work.

**Reference**


[1] R. Fouquet, P. J.G. Pearson, Energ. Policy 50 (2012) 1–7

[2] P. R. Ehrlich, P. M. Kareiva, Gretchen C. Daily, Nature, 468 (2012) 68-73.

[3] EIA, History of energy consumption history in US, 2010.

[4] NREL, International energy outlook, Golden, 2011.

[5] IEA, Key energy world statistics, Paris, 2012.

[6] IPCC, Climate Change 2007: Synthesis Report, 2007.

[7] IPCC, Climate Change 2007: Working group II technical summary, 2007.

[8] UNFCC, Kyoto protocol to the united nations framework convention on climate change, 1998.

[9] UNFCC, United nations framework convention on climate change, 1992.

[10] The National Diet of Japan, The official report of Executive summary The Fukushima Nuclear Accident Independent Investigation Commission exclusive summary, 2011.

[11] Federal Ministry for the Environment, Nature Conservation and Nuclear Safety, http://www.bmu.de/english/nuclear_safety/response_to_fukushima/questions_and_answers/doc/49010.php, 2012.

[12] IPCC, Renewable Energy Sources and Climate Change Mitigation Special Report of the Intergovernmental Panel on Climate Change, Cambridge university press, New York,2012

[13] EIA, Annual energy outlook 2012, 2012.

[14] A. Luque, Handbook of photovoltaic science and engineering, John Wiley & Sons, West Essex,2003.

[15] REN21, Renewables 2012 Global status report, 2012.

[16] K. Brankera, M. J. M. Pathaka, J. M. Pearcea, Renew. Sust. Energ. Rev. 15 (2011) 4470– 4482.

[17] X. Wang, L. Kurdgelashvili, J. Byrne, Allen Barnett, Renew. Sust. Energ. Rev. 15 (2011) 4248– 4254.

[18] EIA, Average price of photovoltaic cells and modules, 2002-2011.

[19] M. A. Green, Prog. Photovolt.: Res. Appl. 9 (2001) 123-135.

[20] M. A. Green, K. Emery, Y. Hishikawa, W. Warta, E. D. Dunlop, Prog. Photovolt.: Res. Appl. 20 (2012) 606–614.

[21] First Solar Annual Report, Phoenix, 2011.

[22] P. Jackson, D. Hariskos, E. Lotter, S. Paetel, R. Wuerz, R. Menner, W. Wischmann, M. Powalla, Prog. Photovolt.: Res. Appl. 19 (2011) 894-897.

[23] W. Shockley, H. J. Queisser, J. Appl. Phys. 32 (1961) 510-519.

[24] H. Cotal, C. Fetzer, J. Boisvert, G. Kinsey, R. King, P. Hebert, H. Yoon, N. Karam, Energ. & Environmental Sci. 2 (2009) 174-192.

[25] O. E. Semonin, J. M. Luther, S. Choi, H. Chen, J. Gao, A. J. Nozik, Matthew C. Beard, Science 334 (2011) 1530-1533.

[26] NREL, Best research-cell efficiency chart, Golden, 2012.

[27] A. Banerjee, T. Su, D. Beglau, G. Pietka, F. S. Liu, S. Almutawalli, J. Yang, S. Guha, IEEE J. Photovolt. 2 (2011), 99-103.

[28] T. Ameri, G. Dennler, C. Lungenschmied, C. J. Brabec, Energy Environ. Sci. 2 (2009) 347–363.

[29] A. Shah, P. Torres, R. Tscharner, N. Wyrsch, H. Keppner, Science 30 (1999) 692-698.

[30] BBC, http://www.bbc.co.uk/news/business-16611040.

[31] S. R. Kodigala, $CuIn_{1-x}Ga_xSe_2$ Based Thin Film Solar Cells - Thin Films and Nanostructures Volume 35, Academic Press, New York, 2010.

[32] R. Scheer, H. Schock, Chalcogenide Photovoltaics Physics, Technologies, and Thin Film Devices, Wiley-VCH, Weinheim, 2011.

[33] R. M. Swanson, Science 324 (2009) 891-892.

[34] M. A. Contreras, L. M. Mansfield, B. Egaas, J. Li, M. Romero, R. Noufi, E. Rudiger-Voigt, W. Mannstadt, Prog. Photovolt.: Res. Appl. 20 (2012) 843–850.

[35] A. Martí, G. L. Araújo, Sol. Energy Mater. Sol. Cells 43 (1996) 203–222.

# Chapter 2

## Degradation Mechanisms of Copper Indium Gallium Diselenide Solar cells

### 2.1. Introduction

The efficiency limit and ideal band gap for the maximum efficiency of single junction solar cells are about 32% and 1.4 eV, respectively [ 1 ]. However, the experimental results are way below 32%. The highest efficiency single junction solar cell is 28.8% in single crystal thin film GaAs [2,3]. Monocrystalline solar cells have high efficiencies due to their ideal material properties and low defect densities, however are not affordable because of high production costs [4]. Thus, low cost and high efficiency multi-crystalline thin film solar cells are highly interesting [5]. Since multi-crystalline thin film solar cells are fabricated on various inexpensive substrates and consume a small amount of materials, the energy cost of making thin film solar cells are lower than any other mass production solar cell technology. The module manufacturing cost of CdTe solar cells is 75 cents/watt [5,6]. However the imperfect structure of materials that are not single crystal degrade the performance of solar cells making the maximum efficiency of thin film solar lower than monocrystalline solar cells. The maximum efficiency is about to 20% in $CuIn_{1-x}Ga_xSe_2$ (CIGS) solar cells [7]. Even though, the maximum efficiencies of CIGS and CdTe solar cells are 20.4% and 18.3% in lab, respectively. As of 2011, the

average efficiencies of mass produced solar cells were around 11~12% [6]. Thus, it is important to understand the degradation mechanisms in thin film multi-crystalline solar cells. The analysis and control of defect are important to improve the solar cell performance. Electrically active defects are mostly due to imperfections in the crystalline structure such as dislocations, grain boundaries and point defects. These defects capture and recombine the optically generated electron-hole pairs (EHPs) directly affecting solar cell performance.

There are several methods to analyze the electrical properties of defects [8-11]. Among those methods, deep level transient spectroscopy (DLTS) and thermal admittance spectroscopy (T-AS) are the most widely used. In DLTS the trap characteristics are characterized by measuring the change of the junction capacitance transient time due to temperature, applied pulsed bias, and bias levels [8]. In T-AS trap characteristics are characterized by measuring the junction capacitance change due with temperature and signal frequency [9]. DLTS can determine the polarity of defects and the activation energy with high resolution, however the measurement system is complicated and it is difficult to characterize the defect density profile. T-AS is simpler to set up and is easier to use to characterize trap characteristics and defect density profiles however, the polarity of defects is indistinguishable [9,12]. The previous admittance model due to traps in T-AS is obtained by solving recombination current without any electrostatic analysis [12]. However, in diodes the junction capacitance is the dominant term in total capacitance under reverse bias. The depletion width is changed by trap densities and activation energy

in depletion region thus junction capacitance should be considered by solving Poisson's equation in the depletion region.

We performed analytical modeling for T-AS by solving classical Poisson equation and charge neutrality with both minority and majority traps and we compared the result of analytical model with numerical simulation results. We also studied the effects of deep traps on the performances of CIGS solar cells fabricated on stainless steel substrates for Dow Chemical.

## 2.2. Solar cell characterization methods.

### 2.2.1. Temperature dependent current voltage characteristics (T-I-V).

The band gap of the absorber layer is the one of the most important physical parameters of a PV device because it determines the theoretical limit on efficiency. The material composition of CIGS can change the band gap so it is important to know the band gap in the device. This can be extracted by temperature-dependent current-voltage characteristics.

The basic current mechanisms of solid state solar cells are comprised of drift-diffusion currents of the p-n junction diode and optically generated current due to electron-hole pairs (EHPs). The general current – voltage equation of an ideal solar cell is

$$J = J_{df}\left[\exp\left(\frac{V}{kT}\right)-1\right]-J_{ph} \approx J_{df}\exp\left(\frac{V}{kT}\right)-J_{ph} \qquad (2\text{-}1)$$

where

$$J_{df} = qn_i^2\left(\frac{D_p}{L_P N_D} + \frac{D_n}{L_n N_A}\right) = qN_C N_V\left(\frac{D_p}{L_P N_D} + \frac{D_n}{L_n N_A}\right)\exp\left(-\frac{E_g}{kT}\right) = J_{df0}\exp\left(-\frac{E_g}{kT}\right), \quad (2\text{-}2)$$

$D_{n,p}$, $L_{n,p}$, and $N_{D,A}$, are diffusion coefficient, diffusion length, and majority carrier concentration of electron (n and D) and holes (p and A). $N_{C,V}$, $n_i$, $E_g$, $k$, and $T$ are the density of states of the conduction and valence bands, the intrinsic carrier concentration, the band gap, Boltzmann's constant and the temperature, respectively [13]. The general Shockley-Reed-Hall (SRH) recombination current equation is

$$J = J_{re}\left[\exp\left(\frac{V}{2kT}\right) - 1\right] - J_{ph} \approx J_{re0}\exp\left(\frac{V}{2kT}\right) - J_{ph} \quad (2\text{-}3)$$

where

$$J_{re} = \frac{qw}{2\tau}n_i = J_{re0}\exp\left(-\frac{E_g}{2kT}\right), \quad (2\text{-}4)$$

$\tau$, $w$ and $n_i$ are carrier lifetime, depletion width and intrinsic carrier concentration.

The open circuit voltages ($V_{OC}$) by drift-diffusion and SRH mechanisms are

$$V_{OC} = kT\ln\left(\frac{J_{ph}}{J_{df}}\right) = E_g - kT\ln\left(\frac{J_{df0}}{J_{ph}}\right) \quad (2\text{-}5)$$

and,

$$V_{OC} = 2kT\ln\left(\frac{J_{ph}}{J_{re}}\right) = E_g - kT\ln\left(\frac{J_{df0}}{J_{ph}}\right), \quad (2\text{-}6)$$

respectively. From T - $V_{OC}$ relationship in equation (2-5) and (2-6), the intercept point at 0 K is the band gap of absorber layer. [14].

### 2.2.2. Quantum efficiency (QE).

The short circuit current ($J_{SC}$) is the collection of EHPs which are photo-generated by the solar spectrum above the band gap of the absorber layer [15]. The quantum efficiency is the ratio of photo generated current to illuminated photon flux measured as a function of irradiating wavelength. By measuring the QE, the photon loss mechanism can be analyzed and also optical band gap can be estimated. In the ideal case, all illuminated photons above the band gap are completely absorbed and collected at the electrodes without loss. In such a device the QE is unity for these wavelengths. However, the effects of recombination of the photo-generated EHPs, reflection of sunlight, and the limit on absorption due to finite absorber thickness make this unrealistic. Thus, measuring QE as a function of wavelength allows the photon loss mechanism to be analyzed and reduced.

### 2.2.3. Thermal admittance spectroscopy (T-AS).

The junction capacitance is affected by traps because the activation and deactivation of traps in the depletion areas changes the charge distributions and depletion width at thermal equilibrium. The response of traps to an applied AC signal depends on the trap energy level, capture cross-section of traps, and thermal velocity of free carriers. The limit on the frequency response of traps causes the junction capacitance to change in the frequency domain. Thus, the trap characteristics are determined by analyzing the transition characteristics of the junction capacitance as functions of temperature and frequency of the applied AC signal [9,12,16].

**2.2.3.1. Previous works.**

Losee studied admittance spectroscopy in Schottky diodes by majority deep traps [9]. Walter et al. performed analytical modeling of T-AS data by solving the frequency response of the recombination currents due to traps and examined the results in CIGS solar cells [12, 17].

The current due to the recombination of traps is

$$\begin{aligned}\frac{dn_t}{dt} &= \sigma_n v_{th} n\left(N_T - n_t\right) - \sigma_p v_{th} p n_t \\ &\quad - \sigma_n v_{th} N_C n_t \exp\left(-\frac{E_C - E}{kT}\right) + \sigma_p v_{th} N_v \left(N_T - n_t\right)\exp\left(-\frac{E - E_v}{kT}\right),\end{aligned} \tag{2-7}$$

where, $N_{C,V}$, $E_{C,V}$ and $E$ are the density states, energy band edges of the conduction (C) and valence band (V), and the energy of carriers. $n$, $p$, $\sigma_{n,p}$, $n_t$, and $v_{th}$ are the free carrier concentrations and capture cross-sections of electrons (n) and holes (p), the trap density and the thermal velocity of free carriers, respectively.

The response of carriers and traps to the applied signal can be divided by two components, steady state and AC. Then the capacitance due to the AC component is

$$C = \frac{q}{\tilde{u}_{ext}} \frac{\omega_1}{\omega^2 + \omega_0^2}\left[\left(1 - f\left(E\right)\right)\sigma_n v_{th}\tilde{n} + \sigma_p v_{th}\tilde{p}\right]N_T \approx \frac{1}{\omega^2 + \omega_0^2} \tag{2-8}$$

where,

$$\omega_0 = \sigma_p v_{th}\overline{p}\left(1 + \exp\left(\frac{E_f - E}{kT}\right)\right) + \sigma_n v_{th}\overline{n}\left(1 + \exp\left(\frac{E - E_f}{kT}\right)\right), \tag{2-9}$$

$$\omega_1 = \sigma_p v_{th}\overline{p}\left(1 + \exp\left(\frac{E_f - E}{kT}\right)\right) - \sigma_n v_{th}\overline{n}\left(1 + \exp\left(\frac{E - E_f}{kT}\right)\right), \tag{2-10}$$

$\omega$, $f(E)$ and $E_f$ are angular frequency, Fermi-Dirac distribution and Fermi level, respectively [17]. $\tilde{u}_{ext}$, $\tilde{n}$, $\tilde{p}$, $\bar{n}$, and $\bar{p}$ are external applied AC bias, AC components of the free electron and hole densities, and steady state components of the free electron and hole densities, respectively [12]. $\omega_0$ is the escape frequency, approximately given by

$$\omega_0 \approx \sigma_{n,p} v_{th} N_{C,V} \exp\left(-\frac{\left|E_f - E_{C,V}\right|}{kT}\right) = \sigma_p v_{th} N_{C,V} \exp\left(-\frac{E_a}{kT}\right). \qquad (2\text{-}11)$$

From equation (2-8), the capacitance difference between high frequency and low frequency is proportional to $1/\omega_0^2$ and the inflection points of the capacitance on a logarithmic scale of frequency are determined by $\omega_0$. The activation energy of the trap is extracted by the logarithmic correlation between $\omega_0/T^2$ and q/kT as shown in equation (2-11).

When the potential in the depletion region is linear, the trap profile is

$$N_T = -\frac{V_{bi}}{qw}\frac{dC}{d\omega}\frac{\omega}{kT} = c(\omega)\frac{1}{kT}\frac{dC}{d\ln\omega}, \qquad (2\text{-}12)$$

where $V_{bi}$ is the built-in potential and $w$ is the depletion width [12].

The model of Walter et al. assumed a simple linear or quadratic dependence on position for the energy potential in depletion region. Thus the potential change due to traps was not considered. Thus, the extracted trap characteristics traps are the same for minority and majority traps. That is, the polarity of traps cannot be distinguished. However, the characteristics of junction capacitance due to majority and minority traps are different obviously.

**2.2.3.2. Analytical model.**

**2.2.3.2.1 Majority trap case.**

For a simple analytical calculation, we assume a one-sided abrupt junction ($N_D >> N_A+N_T$). Details of the calculations are shown in Appendix 1.

The total depletion width ($W$) with majority traps is

$$W \approx x_p = \sqrt{\frac{2\varepsilon_p}{q(N_A + N_T)}(V_{bi} - V) - m(1-m)\lambda^2} + m\lambda \tag{2-13}$$

where,

$$m = \frac{N_T}{N_A + N_T}, \tag{2-14}$$

$$\lambda = \sqrt{\frac{2\varepsilon_p}{qN_A}\Delta E_{TF}}, \tag{2-15}$$

$$\Delta E_{TF} = E_T - E_F, \tag{2-16}$$

and $N_A$, $N_T$, $V_{bi}$, $V$, $\varepsilon_p$, and $q$ are the dopant concentration in p-type region, trap concentration, built-in voltage, applied voltage, relative dielectric constant, and charge, respectively.

The junction capacitance ($C_{maj}$) is simply,

$$C_{maj} = \frac{\Delta Q}{\Delta V} = \frac{\varepsilon_p}{x_p - \lambda \dfrac{N_T(\omega)}{N_A + N_T(\omega)}} \tag{2-17}$$

The trap density in the frequency domain is

$$N_T(\omega) = \frac{N_T}{\dfrac{\omega}{\omega_0} + 1}, \tag{2-18}$$

$$\omega_0 = \frac{2\pi}{\tau} = 2\pi\sigma\upsilon_{th}N_v \exp\left(\frac{E_v - E_T}{kT}\right). \tag{2-19}$$

When the frequency is lower than the cutoff frequency ( $\omega_0$ ), the capacitance ( $C_{maj\_lf}$ ) is

$$C_{maj\_lf} = \frac{\varepsilon_p}{x_p - \lambda\dfrac{N_T}{N_A + N_T}} = \frac{\varepsilon_p}{\sqrt{\dfrac{2\varepsilon_p}{q(N_A + N_T)}(V_{bi} - V) - m(1-m)\lambda^2}}. \tag{2-20}$$

The capacitance at high frequency ( $C_{maj\_hf}$ ) is

$$C_{maj\_hf} = \frac{\varepsilon_p}{x_p} = \frac{\varepsilon_p}{\sqrt{\dfrac{2\varepsilon_p}{q(N_A + N_T)}(V_{bi} - V) - m(1-m)\lambda^2} + m\lambda}. \tag{2-21}$$

The ratio of capacitance difference at high and low frequency to high frequency capacitance is

$$\frac{C_{\min\_lf} - C_{\min\_hf}}{C_{\min\_hf}} = \frac{m\lambda}{\sqrt{\dfrac{2\varepsilon_p}{q(N_A + N_T)}(V_{bi} - V) - m(1-k)m^2}} = \frac{m}{\sqrt{(1-m)}\sqrt{\dfrac{V_{bi} - V}{\Delta E_{TF}} - m}}. \tag{2-22}$$

**2.2.3.2.2 Minority trap case.**

The depletion width ($W$) with minority traps is

$$W = x_p \approx \sqrt{\frac{2\varepsilon_p}{qN_A}(V_{bi} - V) - n(1-n)\lambda^2} + n\lambda \tag{2-23}$$

where

$$n = \frac{N_T}{N_A}, \tag{2-24}$$

$$\lambda = \sqrt{\frac{2\varepsilon_p}{q(N_A - N_T)}(\Delta E_{TF} - V)}, \tag{2-25}$$

and

$$\Delta E_{TF} = E_T - E_F . \tag{2-26}$$

The junction capacitance due to minority traps ($C_{min}$) is

$$C_{\min} = \frac{\varepsilon_p}{x_p}\left[1 + \frac{N_T(\omega)}{N_A}\left(\frac{x_p}{\lambda} - 1\right)\right] \tag{2-27}$$

The capacitance in low frequency ( $C_{\min\_lf}$ ) is

$$C_{\min\_lf} = \frac{N_T}{N_A}\varepsilon_p\left(\frac{1}{\lambda} - \frac{1}{x_p}\right) + \frac{\varepsilon_p}{x_p} = \frac{N_T}{N_A}\frac{\varepsilon_p}{\lambda} + \left(1 - \frac{N_T}{N_A}\right)\frac{\varepsilon_p}{x_p} = n\frac{\varepsilon_p}{\lambda} + (1-n)\frac{\varepsilon_p}{x_p}. \tag{2-28}$$

The capacitance at high frequency ( $C_{\min\_hf}$ ) is simply

$$C_{\min\_hf} = \frac{\varepsilon_P}{x_P} \tag{2-29}$$

The ratio of capacitance difference at high and low frequency to high frequency capacitance is

$$\frac{C_{\min\_lf} - C_{\min\_hf}}{C_{\min\_hf}} = n\left(\frac{x_p}{\lambda} - 1\right) = n\left[\sqrt{1-n}\sqrt{\frac{V_{bi} - V}{\Delta E_{TF} - V} - n} + n - 1\right]. \tag{2-30}$$

**2.2.3.3 Modeling and simulation results.**

To verify our analytical model, we compared the results of our analytical model with numerical simulation. We used 1D numerical simulator AFORS-HET for numerical simulations of junction capacitance with minority and majority traps [18]. We used a

CIGS p-n homojunction diode with a single trap density at the trap energy. For simplification, we assumed one side $n^+$-p homojunction i.e. $1\times10^{19}$ $cm^{-3}$ heavy carrier concentration in n-type region and traps existed only in p-type region. To examine the effects due to trap types, the trap concentrations, activation energies from the each band edge and capture cross sections of majority (acceptor like) and minority (donor like) trap were same, 0.3 eV , $9\times10^{15}$ $cm^{-3}$ and $1\times10^{-14}$ $cm^{-2}$. The carrier concentrations of shallow acceptors were decided to have similar free carrier concentration with majority and minority traps at the charge neutral region. Since majority traps were inactivated at charger neutral region, the carrier concentration of shallow acceptors with majority traps was $1\times10^{15}$ $cm^{-3}$. On the contrary, minority traps were activated and compensated the shallow acceptor traps at charger neutral region thus the carrier concentration of shallow acceptors with minority traps was $1\times10^{16}$ $cm^{-3}$. The free carrier concentrations of majority and minority traps at charge neutral region were $1.65\times10^{15}$ $cm^{-3}$ and $9\times10^{14}$ $cm^{-3}$, respectively at 300 K as shown in Figure 2.1. Device structures and parameters for simulation are shown in Table 2.1. The thicknesses of n-type and p-type region were 0.1 μm and 1.5 μm respectively. The relative dielectic constant, density states of electrons and holes of CIGS are 13.6, $6.3\times10^{18}$ $cm^{-3}$ and $1.4\times10^{19}$ $cm^{-3}$.

Figure 2.1 show the comparisons of junction capacitances and carrier profiles of our model and the numerical simulation results with minority and majority traps at thermal equilibrium state due to minority and majority traps. The capacitance characteristics of our analytical model matched well with simulation results. Junction

capacitances are modeled by the parallel connection of two capacitances corresponding to free carriers and traps, respectively.

Table 2.1. The structures and parameters of $n^+$-p junction diodes with majority and minority traps.

| Type | | n-type | p-type | |
|---|---|---|---|---|
| Traps | | | Majority | Minority |
| Thickness [μm] | | 0.1 | 1.5 | |
| Shallow carrier concentration [$cm^{-3}$] | | $1\times10^{19}$ | $1\times10^{15}$ | $1\times10^{16}$ |
| Trap | $N_T$ [$cm^{-3}$] | | $9\times10^{15}$ | |
| | $E_T$ [eV] | | 0.3 eV above $E_V$ | 0.3 eV below $E_C$ |
| | σ [$cm^{-2}$] | | $1\times10^{14}$ | |

At low temperature, capture and emission process of traps were frozen and only free carriers at the depletion edge responded to the AC signal. Thus junction capacitances were low. With increasing temperature, traps start to respond to the AC signal, thus total junction capacitance increased for both minority and majority traps as shown in Figure 2.1 (a) and (b). The frequency response of the traps changes the inflection temperature of the temperature-capacitance characteristics. The inflection temperatures were 233 K, 173K, and 143 K at 1 MHz, 100 kHz, and 10 kHz AC signals with majority traps, respectively. As low applied frequency, the trap states can respond to the AC signal with the low thermal velocity of the free carriers. The inflection temperatures with minority

trap junction were high since the density of states of the conduction band and valences band are different.

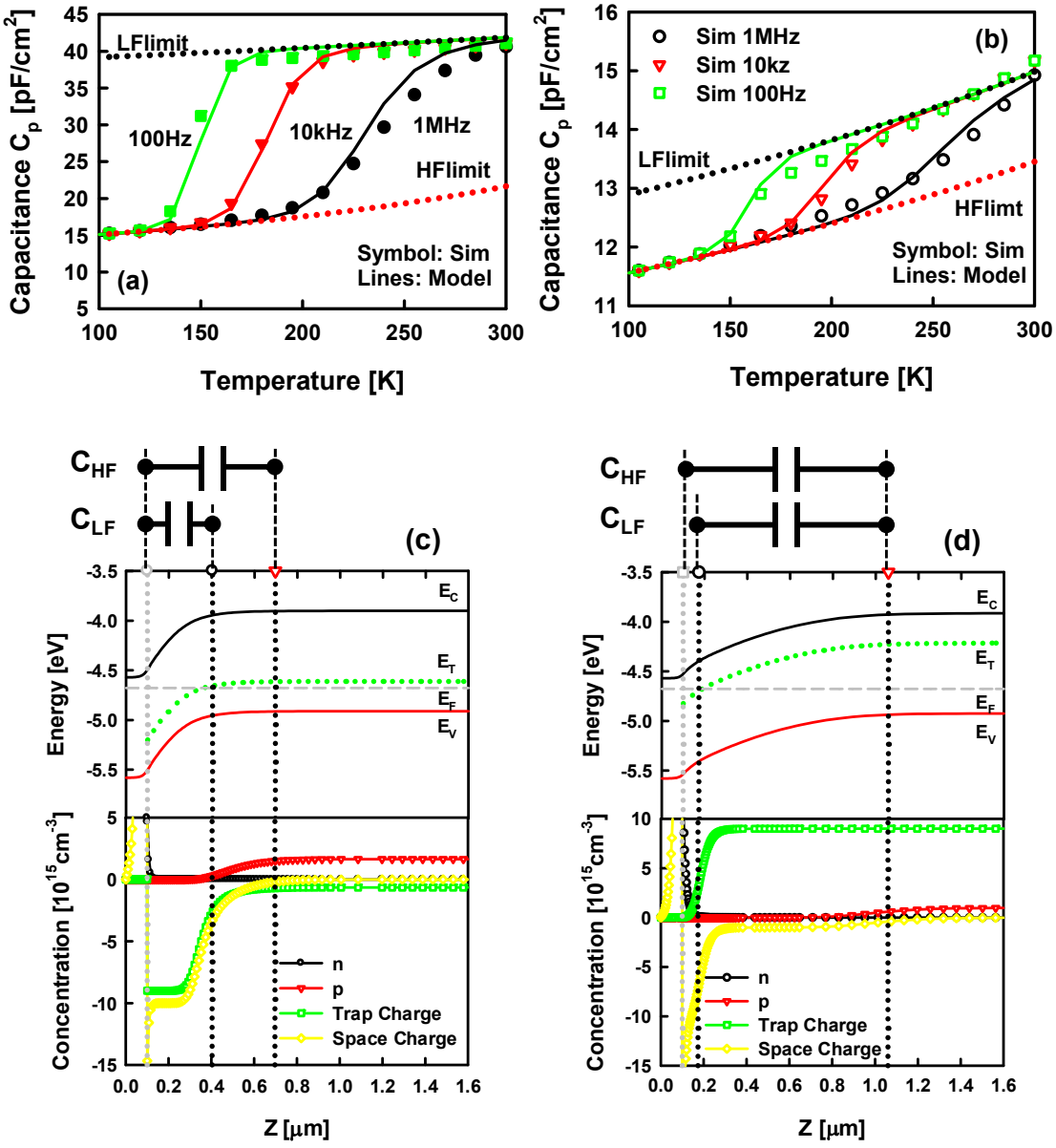


Figure 2.1. Junction capacitance of with (a) majority traps and (b) minority traps due to temperature and frequency.

As shown in Figure 2.1 (c) and (d), even if the activation energies of the majority and minority traps are the same, the locations in depletion region where the Fermi level was at the same energy as the trap level were different. Thus this difference in distances from the depletion edges created a difference in the junction capacitance for different polarity traps. Figure 2.2 shows the ratio of the capacitance difference at high and low frequency to high frequency capacitance at 300 K due to majority and minority trap densities when the dopant concentration is $1\times10^{16}$ $cm^{-3}$.

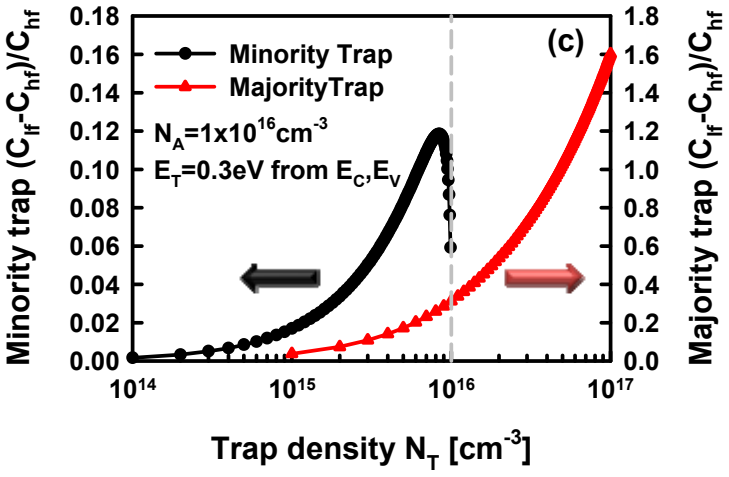


Figure 2.2. The ratio of capacitance difference at high and low frequency to low frequency capacitance due to majority and minority trap densities.

As the trap density increases, the capacitance difference between the high and low frequency saturated capacitance increase. The significant difference in capacitance characteristics between majority and minority traps is due to the possible maximum trap

densities of minority and majority traps. The minority trap density cannot be higher the total majority carrier density, while there is no limit in majority trap densities. Thus, the capacitance difference due to minority traps can be only 0.12 times of the high frequency capacitance. By contrast, the capacitance difference due to majority traps can be several times that of the high frequency capacitance. As shown in Figure 2.1 (a) and (b), the capacitance difference was 0.93 times of high frequency capacitance with majority traps while it is 0.11 times of high frequency capacitance with minority traps. From this results, both majority and minority traps can exist inside the junction when the ratio of the capacitance difference to high frequency capacitance is lower than 0.12 however if it is higher than 0.12, only majority traps are possible. Thus, the polarity of traps may be distinguishable if the ratio of capacitance difference to high frequency capacitance is large.

**2.3. Solar cells measurement and characterization.**

We analyzed the electrical characteristics of four CIGS solar cells fabricated on stainless steel substrates using co-sputtering, supplied by Dow Chemical. Analysis was done using temperature dependence current – voltage (I-V) measurement (T-I-V), external quantum efficiency (EQE), and thermal admittance spectroscopy (T-AS) methods. The area of solar cells was 0.416 $cm^2$. Samples were obtained from two different efficiency points on two different substrates (batch 36 and 41).

### 2.3.1. Thermal admittance spectroscopy (T-AS) measurement setup.

Figure 2.3 shows the schematic diagram for thermal admittance spectroscopy. Solar cells were measured in Janis ST-500-2(6TX) cryogenic probe station. The probe station was cooled by liquid nitrogen ($LN_2$) and heated electrically. The temperature was controlled by a Scientific instrument 9700 temperature controller. The solar cell measurement was performed inside the vacuum chamber with six probe positioner and tips. The vacuum level was about $5\times10^{-5}$ Torr. To measure the precise temperature of samples, we attached a resistance temperature detector (RTD) on the top of samples. The RTD was calibrated and measured by an Agilent 4155C semiconductor parameter analyzer. The solar cells were probed using Kelvin probe configurations to remove the parasitic electrical elements. The admittance was measured using Agilent 4294A precision impedance analyzer.

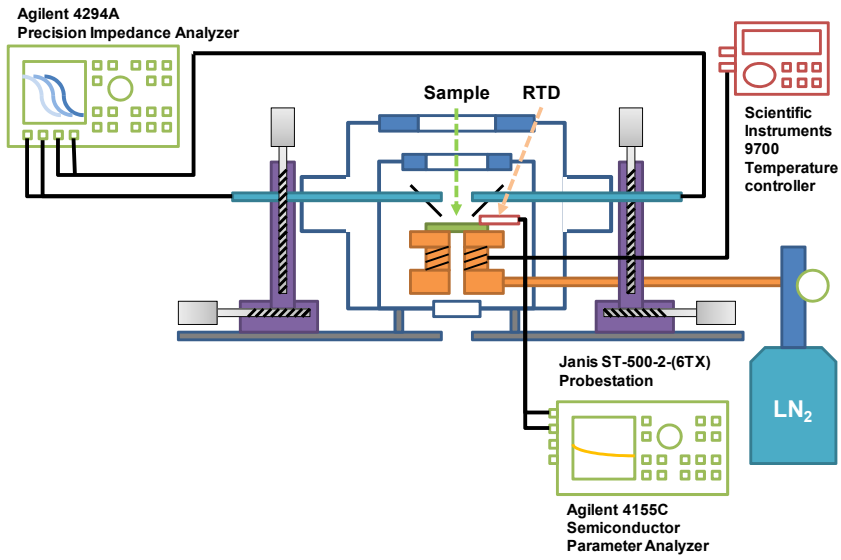


Figure 2.3. Schematic diagram of thermal admittance spectroscopy measurement setup.

### 2.3.2. Temperature - current - voltage (T-I-V), solar cell performance and external quantum efficiency (EQE) measurement setup.

Figure 2.4 and 2.5 shows a schematic diagram of the DC measurement and a photograph of the measurement system. An Oriel Series Q Xe arc lamp was used for the solar simulator with an Oriel 81092 AM1.5 optical filter. For external quantum efficiency measurement, a Cornerstone 120 1/8 m monochromator was used to select the specific wavelength. The width of light from the monochromator was 5 nm in wavelength. I-V characteristics were measured using Agilent 4155C semiconductor parameter analyzer.

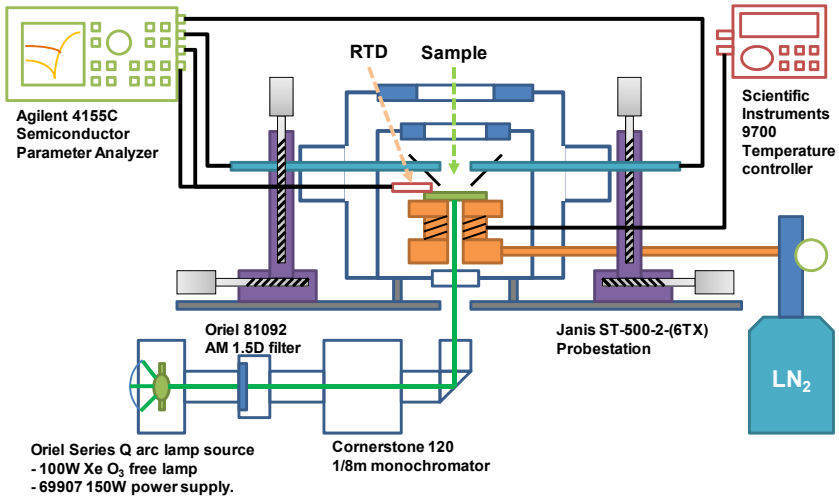


Figure 2.4. Schematic diagram of solar cell performance, external quantum efficiency and temperature dependence I-V measurement setup.

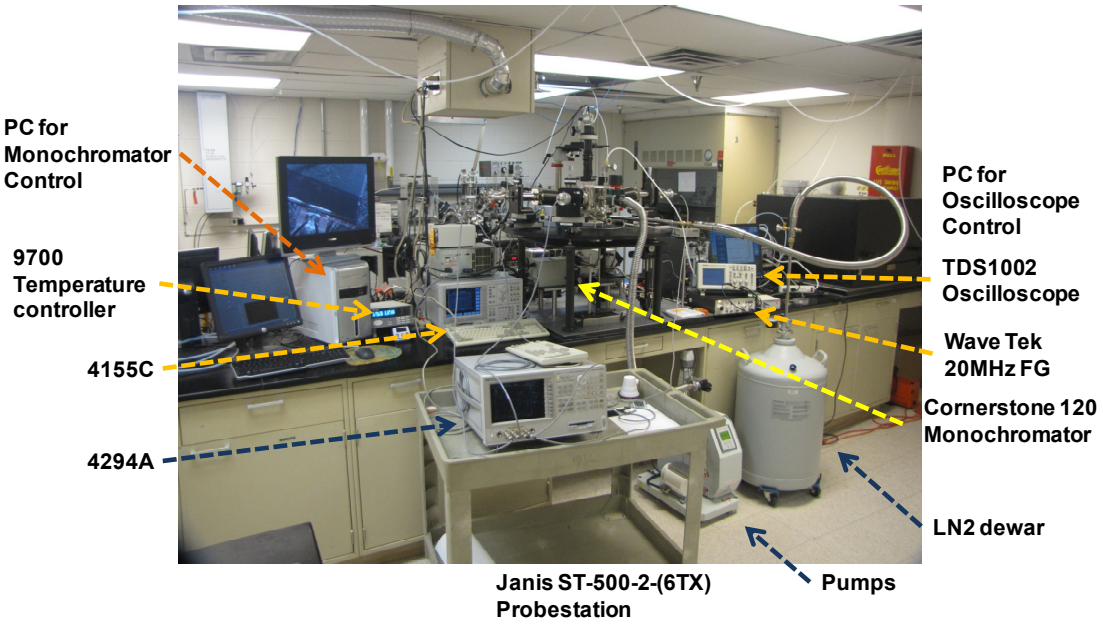


Figure 2.5. The image of measurement equipment and setup.

## 2.4. Results and discussions.

### 2.4.1. I-V characteristics.

Figure 2.6 show current density-voltage (J-V) characteristics of CIGS solar cells. Solar cell performance and parasitic elements are summarized in Table 2.2. Figure 2.6 (a) shows the dark (dotted lines) and illuminated (solid lines) I-V characteristics under AM 1.5. The efficiency of 36-1, 36-2, 41-4, and 41-12 were 6.60%, 4.44%, 3.45% and 4.38%, respectively. Comparing 41-4 and 41-12 to 36-1 and 36-2, $V_{OC}$s were higher and $J_{SC}$s were lower. The low shunt resistance, 16.89 $\Omega/cm^2$, degrades the fill factor and efficiency of 41-4 significantly. The efficiencies were correlated with shunt resistances as shown in Table 2.2. Parasitic resistances in illumination were linearly correlated to dark parasitic

resistances. Thus, it is important to understand the dark current mechanism to increase the shunt resistances under illumination. The dark current characteristics at 300 K were separated to two different current mechanisms below and above the 0.2V as shown in Figure 2.6 (b). Above 0.2 V, recombination currents were dominant because the ideality factors were higher than 1 as shown in Table 2.2. Since two mechanisms were both operative, the ideality factors were higher than 2. Current characteristics at low bias (< 0.2 V) were related with shunt resistance. The currents at low bias were symmetric in bias polarity. At 120 K, recombination currents were completely suppressed and the low bias current characteristic was dominant. The current characteristics have a very weak positive temperature dependence. Among the several current mechanisms, Fowler-Nordheim (F-N) tunneling mechanism was well matched with low temperature J-V characteristics. A general current-voltage equation of F-N tunneling is given as

$$J \propto F^2 \exp\left[-\frac{4\sqrt{m^*}(q\phi_B)^{3/2}}{3q\hbar F}\right] \propto V^2 \exp\left[-\frac{b}{V}\right] \tag{2-31}$$

[13]. Tunneling current has no temperature dependence, thus the I-V characteristics was well matched with the current characteristics at low bias. Figure 2.6 (c) show the fitting results of dark I-V characteristics with equation (2-31) at 120 K. The model was very well matched with measurement data.

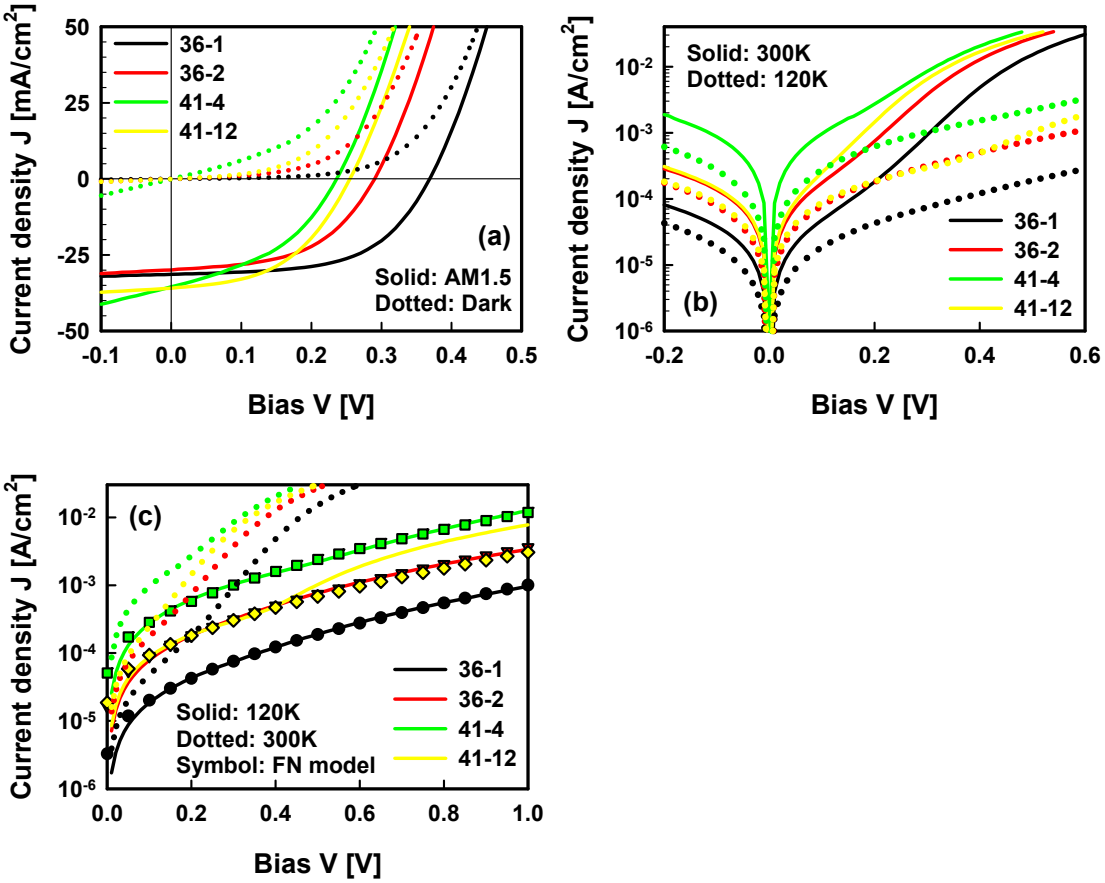


Figure 2.6. (a) dark (dotted lines) and illuminated (solid lines) I-V characteristic, (b) Semi-log scale dark I-V characteristic, and (c) fitting results of F-N tunneling current (F-N model) and measurement data at 120 K.

The band gaps ($E_g$) of the absorber layers were extracted by measuring the temperature (T) and $V_{OC}$ relationship using equation (2-6) as shown in Figure 2.7. At low temperature, F-N tunneling became the dominant current mechanism rather than diode or recombination. Thus the T-$V_{OC}$ characteristics were not linear and saturated. We estimated the band gap T-$V_{OC}$ characteristics at high temperature. The extracted band gaps of 36-1, 36-2, 41-4, and 41-12 were 1.316 eV, 0.999 eV, 1.077eV, and 0.988 eV,

respectively. The high $V_{OC}$ of 36-1 was due to the high band gap of the absorber however the extracted band gaps did not match the $V_{OC}$ in other samples.

Table 2.2. Solar cell performance and parasitic element characteristics.

| | | 36-1 | 36-2 | 41-4 | 41-12 |
|---|---|---|---|---|---|
| Illumination | $V_{OC}$ [V] | 0.369 | 0.290 | 0.236 | 0.255 |
| | $J_{SC}$ [mA/cm$^2$] | 31.39 | 29.86 | 35.49 | 35.91 |
| | FF [%] | 57.04 | 51.28 | 41.16 | 47.86 |
| | Efficiency [%] | 6.60 | 4.44 | 3.45 | 4.38 |
| | Shunt R [Ωcm$^2$] | 151.75 | 66.42 | 16.89 | 54.06 |
| | Series R [Ωcm$^2$] | 0.763 | 0.766 | 0.584 | 0.825 |
| | $E_g$ [eV] | 1.316 | 0.999 | 1.077 | 0.988 |
| Dark | $J_0$ [μA/cm$^2$] | 4.64 | 26.3 | 257 | 21.7 |
| | Ideality factor A | 2.23 | 2.39 | 3.35 | 2.27 |
| | Shunt R [Ωcm$^2$] | 2571 | 716 | 116 | 635 |
| | Series R [Ωcm$^2$] | 3.00 | 3.27 | 1.94 | 4.30 |

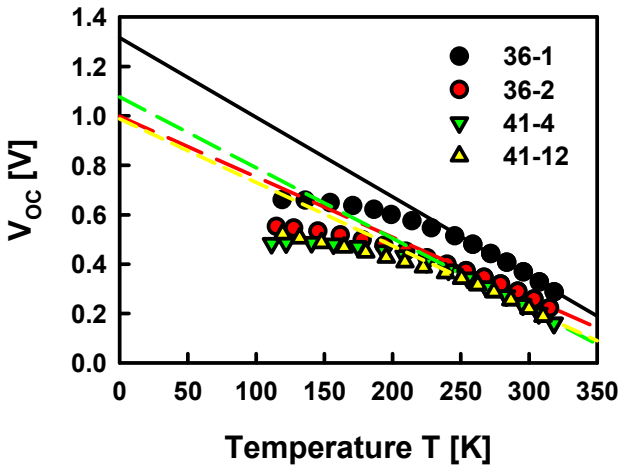


Figure 2.7. Temperature (T) – $V_{OC}$ characteristics.

### 2.4.2. External quantum efficiency (EQE).

Figure 2.8 show the external quantum efficiency results of 36-1 and 41-12. The maximum quantum efficiencies of 36-1 and 41-12 were 81.9% and 83.5% at 625 nm, respectively. The quantum efficiencies of 41-12 were 5~10% higher than 36-1 below 500 nm and above 850 nm. The quantum efficiency loss below 500 nm is mostly due to the photon absorption in CdS buffer layer [19]. Thin CdS layer increases the quantum efficiency in this region however it can cause leakage current because of insufficient surface passivation [19]. Thus, the thickness of CdS layer of 41-12 may be thinner than 36-1 since leakage current of 36-1 was lower than 41-12. The band gap of 36-1 and 41-12 were 1.05 and 1.01 eV respectively. The lower band gap of 41-12 increased $J_{SC}$ and the quantum efficiencies above 850 nm but $V_{OC}$ was lower than 36-1.

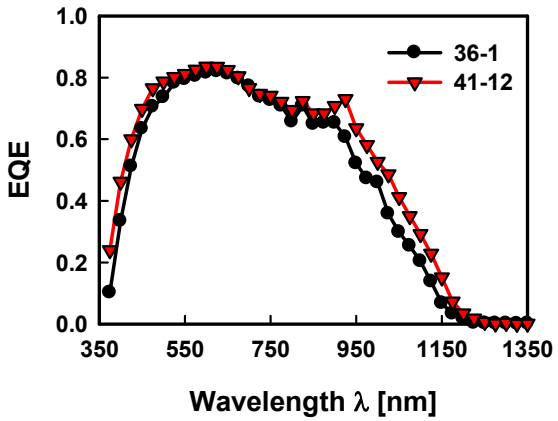


Figure 2.8. External quantum efficiency of 36-1 and 41-12.

### 2.4.3. Thermal admittance spectroscopy (T-AS).

Figure 2.9 show the junction capacitance characteristics due to temperature and frequency. Two traps levels are observed in all samples, generally called N1 in the low capacitance level and N2 in the high capacitance level. The low capacitance values of all samples were 10~15 nF/cm$^2$. Capacitance changes due to N1 were lower than N2 and were 7~20 nF/cm$^2$. Since the ratio of capacitance changes to low capacitance values were higher 0.7, from our analytical model, all defects are majority traps.

Figure 2.10 show the Arrhenius plot of $\omega_0/T^2$ vs q/kT of N1 traps and trap profiles of all samples. Since the capacitance characteristics due to N2 traps were linear with frequency over the measurement range, we could not extract the escape frequencies. The activation energies of traps for 36-1, 36-2, 41-4, and 41-12 were 0.22 eV, 0.126 eV, 0.098 eV, and 0.128 eV respectively. The activation energies of 0.22 eV and 0.12 eV may be the Cu anti-site on In and the In vacancy respectively. The total trap densities were 3.25x10$^{15}$ cm$^{-3}$, 4.78x10$^{15}$ cm$^{-3}$, 6.29x10$^{15}$ cm$^{-3}$, and 1.11x10$^{16}$ cm$^{-3}$, respectively as

shown in Table 2.3. The escape frequencies below 170 K saturated in 41-4 and 41-12. The process of filling and emptying traps is by not only generation–recombination but also tunneling [20].

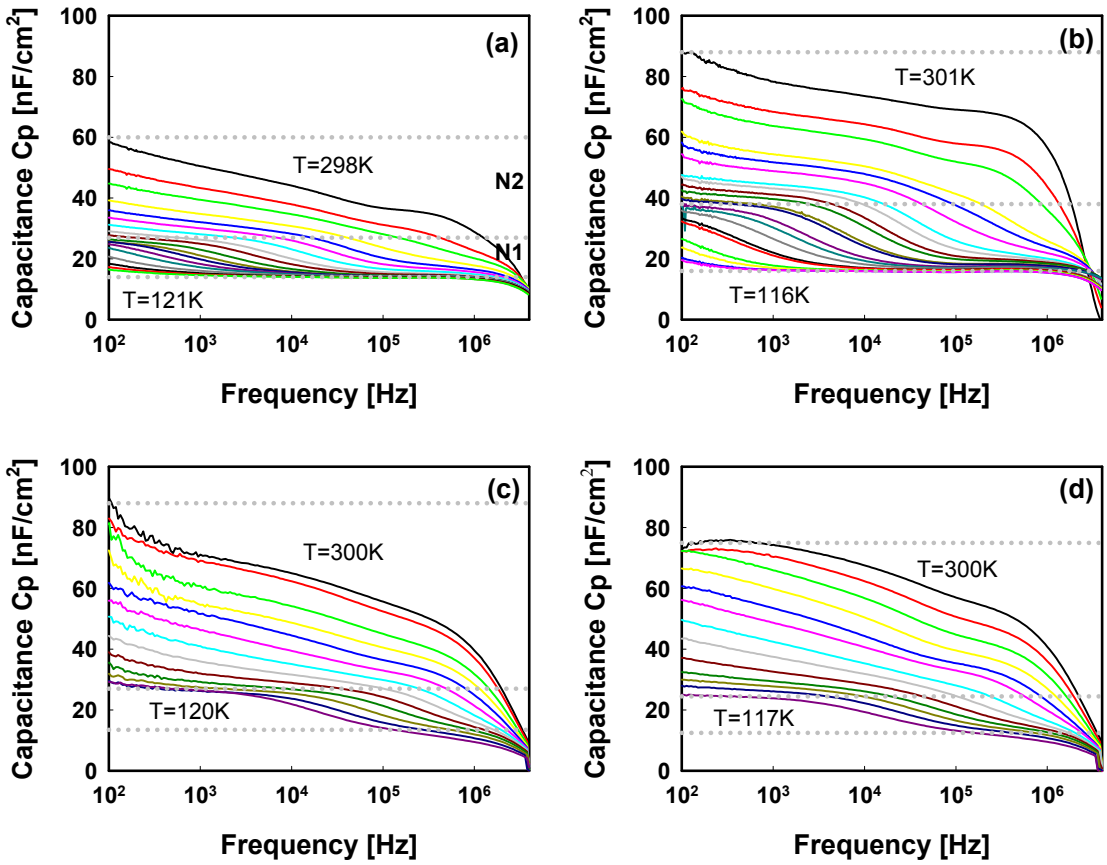


Figure 2.9. Capacitance – frequency characteristics by temperature of (a) 36-1, (b) 36-2, (c) 41-4, and (d) 41-12 from 116 K to 301 K.

Since tunneling process is independent on temperature and the generation–recombination process is logarithmic dependent on the temperature, the emission rates are saturated at low temperature by tunneling process. Thus, 41-4 and 41-12 are exhibiting high emission

rates comparing 36-1 and 36-2. These results are well matched with high F-N tunneling currents and high quantum efficiencies above 500 nm of 41-4 and 41-12. The highest efficiency cell (36-1) has the deepest activation energy and the lowest defect density compared to the other solar cells.

Table 2.3. Trap characteristics of CIGS solar cells.

| | | 36-1 | 36-2 | 41-4 | 41-12 |
|---|---|---|---|---|---|
| Energy [eV] | | 0.220 | 0.126 | 0.098 | 0.128 |
| $\chi_0$ [$s^{-1}k^{-2}$] | | $1.02x10^5$ | $1.91x10^3$ | $1.83x10^4$ | $7.32x10^4$ |
| Capture Cross Section @300k [$x10^{-19}cm^{-2}$] | | 3.14 | 2.25 | 64.94 | 78.68 |
| Trap profile | $N_{T0}$ [$cm^{-3}$] | $4.63x10^{16}$ | $6.81x10^{16}$ | $1.09x10^{17}$ | $7.53x10^{16}$ |
| | σ [eV] | 0.028 | 0.028 | 0.023 | 0.059 |
| | Concentration [$cm^{-3}$] | $3.25x10^{15}$ | $4.78x10^{15}$ | $6.29x10^{15}$ | $1.16x10^{16}$ |

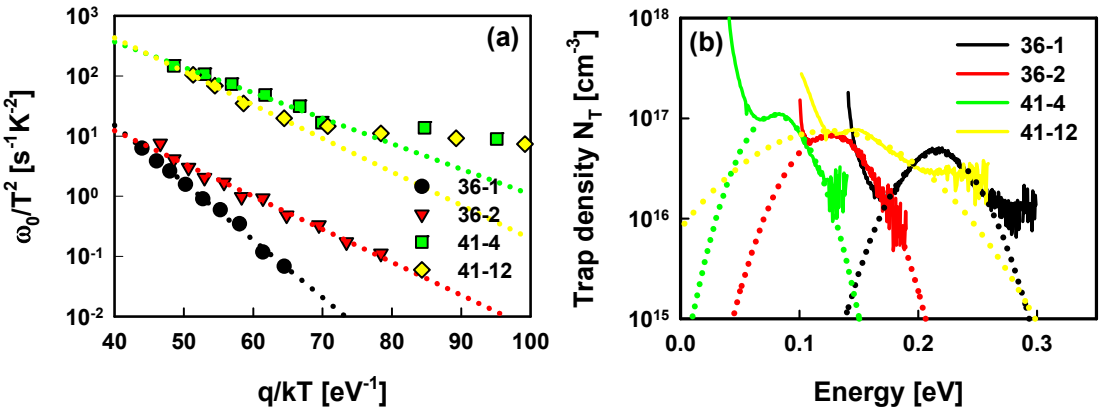


Figure 2.10 (a) Arrhenius plot of $\omega_0/T^2$ vs q/kT and (b) trap profiles of solar cells.

Figure 2.11 shows the correlation between trap characteristics and solar cells parameters in dark. The activation energies of traps were linearly correlated with the efficiencies of solar cells than trap densities. The dark shunt resistances were related to the efficiencies of solar cells as shown in Figure 2.11 (b). The trap energy level can affect the F-N tunneling current in two ways – energy barrier height and electric field from equation (2-19). The activation energies of traps are directly related with the energy barrier in F-N tunneling thus the high activation energies decrease F-N tunneling current. The activation energies of traps also affect the activation ratio of traps. The energy difference between Fermi level and the energy level of traps determine the activation ratio of traps in Fermi-Dirac distribution. The high activation energy is the low activation traps densities and free carrier densities are low. Low free carrier densities reduced the electric field in depletion region. Cu deficiency at the grain boundaries of CIGS creates a large energy barrier in the valence band between grains [21,22]. Energy band bending at the grain interface depletes the free carriers near the grain boundaries. Thus if carriers injected from trap states over the barrier at grain boundaries high trap energy levels have low injection currents low electric field [23,24].

The reverse saturation current increases logarithmically with decreasing activation energy as shown in Figure 2.11 (c). Recombination by traps is maximized when the Fermi level is equal to the trap level in the SRH recombination model [25]. In deep trap activation energy level, the Fermi level crosses the trap levels inside the depletion region. Traps are all empty or filled outside this region and so most recombination happens in depletion region. However, when the trap energy level is low and the trap concentration

is higher than the dopant concentration, recombination occurs not only in depletion region but also in charge neutral region. Thus, shunt resistance and reverse saturation current are increased with decreasing trap activation energies.

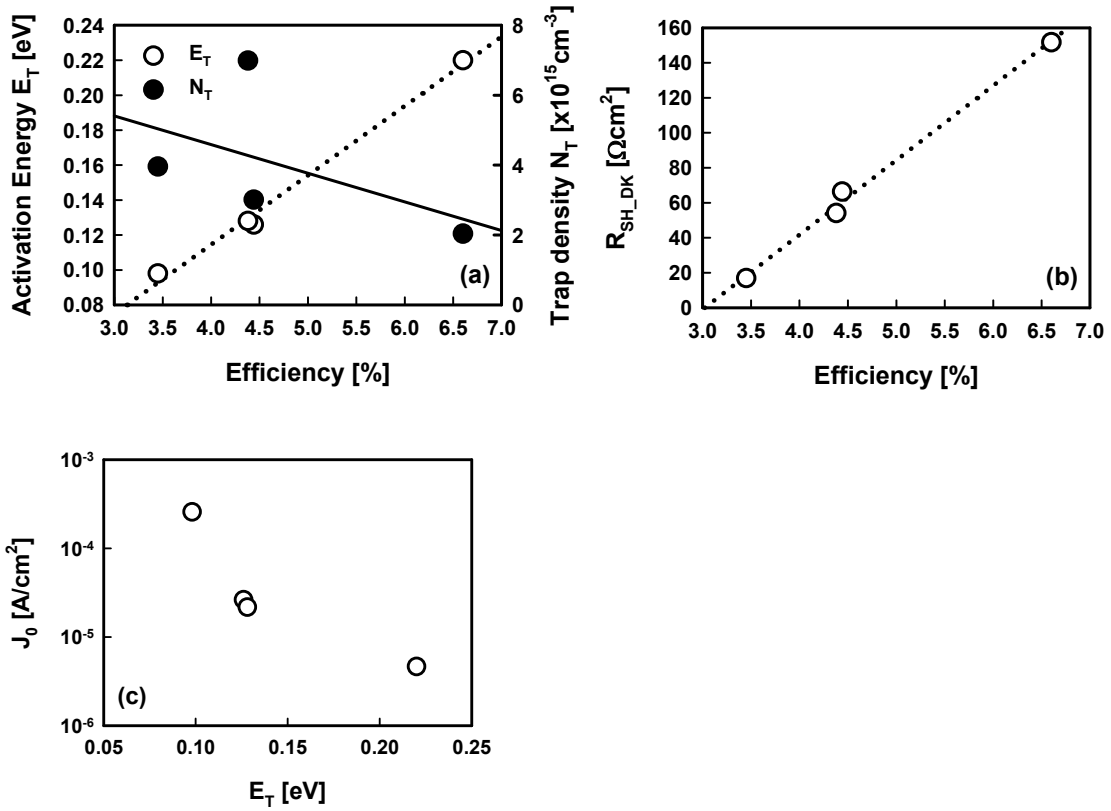


Figure 2.11. The correlation between (a) efficiency and activation energy and density of traps (b) shunt resistance and efficiency, and (c) reverse saturation current ($J_0$) and activation energy.

## 2.5. Conclusions.

We performed analytical modeling for thermal admittance spectroscopy. Capacitance difference by defects in the frequency domain is related to the polarity of the defects. The maximum available capacitance difference by minority traps is about 12% of high frequency capacitance while it is unlimited in majority traps. Thus the type of traps can be distinguished when capacitance differences are higher than 12% of high frequency capacitance. Analytical model results were well matched with numerical simulation results.

We analyzed the trap characteristics and degradation mechanisms of CIGS solar cell on stainless steel foils. All traps were majority traps and activation energies were 0.10 eV to 0.22 eV. Low shunt resistances is the dominant degradation factor in the CIGS solar cells that were provided. A low activation energy of traps in CIGS was correlated linearly with a low shunt resistance and a low efficiency. The current mechanism at low bias was Fowler-Nordheim (F-N) tunneling. The low activation energy reduces the F-N tunnel barrier, and increases electric field at the grain boundaries, thus the F-N tunneling currents increase in low bias. Low defect energies also increase recombination in the charge neutral region, thus reverse saturation current is also increased.

**References**


[1] W. Shockley, H. J. Queisser, J. Appl. Phys., 32 (1961), 510-519.

[2] M. A. Green, K. Emery, Y. Hishikawa, W. Warta, E. D. Dunlop, Prog. Photovolt.: Res. Appl., 21(2013) 1–11

[3] National Renewable Energy Laboratory, Best research cell efficiency record chart, 2013.

[4] IPCC, Renewable Energy Sources and Climate Change Mitigation Special Report of the Intergovernmental Panel on Climate Change, Cambridge university press, New York,2012

[5] K. L. Chopra, P. D. Paulson, V. Dutta, Prog. Photovolt.: Res. Appl. 12 (2004) 69–92.

[6] First Solar First Quarter Financial Report, Phoenix, 2013.

[7] P. Jackson, D. Hariskos, E. Lotter, S. Paetel, R. Wuerz, R. Menner, W. Wischmann, M. Powalla, Prog. Photovolt.: Res. Appl. 19 (2011) 894–897.

[8] D. V. Lang, J. Appl. Phys., 45 (1974) 3023-3032.

[9] D. L. Losee, J. Appl. Phys., 46 (1975) 2204-2214.

[10] L.R. Weisberg, H. Schade, J. Appl. Phys. 39 (1968) 5149–5151.

[11] D.K. Schroder, Semiconductor material and device characterization, John Wiley & Sons, Hoboken, Wiley, 2006.

[12] T. Walter, R. Herberholz, C. Müller, H. W. Schock, J. Appl. Phys. 80 (1968) 4411–4420.

[13] S. M. Sze, Physics of semiconductor devices, John Wiley & Sons, Hoboken, 2007.

[14] V. Nadenau, U. Rau, A. Jasenek, H.W. Schock, J. Appl. Phys. 87 (2000) 584-593.

[15] S. S. Hegedus, W. N. Shafarman, Prog. Photovolt.: Res. Appl. 12 (2004) 155–176.

[16] J. Santamaria, G. Gonzalez Diaz, E Iborra, I. Martil, F. Sanchez-Quesada, J. Appl. Phys. 65 (1989) 3236-3241.

[17] R. Herberholz, M. Igalson, H. W. Schock, J. Appl. Phys. 83 (1998) 318-325.

[18] R. Stangl, M. Kriegel, M. Schmidt, Conference Record, 4th World Conference on Photovoltaic Energy Conversion, Waikoloa, May 2006, 1350-1353.

[19] M. A. Contreras, M. J. Romero, B. To, F. Hasoon, R. Noufi, S. Ward, K. Ramanathan, Thin Solid Films 403–404 (2002) 204–211.

[20] P. Zabierowski, M. Edoff, Thin Solid Films 480–481 (2005) 301– 306.

[21] C. Persson, A. Zunger, Phys. Rev. Lett. 91 (2003) 196602.

[22] M. Hafemeister, S. Siebentritt, J. Albert, M. Ch. Lux-Steiner, S. Sadewasser, Phys. Rev. Lett. 104 (2010) 196602.

[23] U. Rau, K. Taretto, S. Siebentritt, Appl. Phys. A 96 (2009) 221–234.

[24] S. Siebentritt, M. Igalson, C. Persson, S. Lany, Prog. Photovolt.: Res. Appl. 18 (2010) 390–410

[25] C.-T. Sah, R. N. Noyce, W. Shockley, Proc. the IRE, 45 (1957) 1228 – 1243.

# Chapter 3

## Study on Copper Indium Gallium Diselenide Solar Cell Degradation by Air Anneal

### 3.1. Introduction

Reliable, high efficiency solar cells are required to obtain low-cost renewable electric generation. The average energy generation cost is the total investment cost divided by total electricity generated. The total electric generation cost is the grid electricity cost and the efficiencies of solar cells integrated over the lifetime of the cells [1,2]. The lifetime of solar cells is determined by the initial efficiency and the degradation rates. Solar cell degradation is not only due to electrical and photochemical reactions in the solar cell materials themselves but also depends on their environmental conditions such as humidity and temperature [3-7]. To protect solar cells from the environment and so improve their reliability, solar cells are often sealed in a glass and polymer layer. This sealed device is called a module [2,8,9]. Solar cells are installed and used by primarily by the module. The module price is mostly determined by the cost of the solar cells, the module material costs and the module process costs. Since recent efforts to reduce the cost of solar cell module are mainly focused on the cost reduction of the solar cells by increasing efficiency and manufacturing throughput, the fraction of the total cost related to module materials and processing has risen to about 40% [10,11].

Thus, high reliability solar cells that require less sealing, would significantly reduce solar cells module costs, especially in thin film solar cells.

The test and qualification conditions for a solar cell module are published in the IEC 61215/612646 standards [12-14]. The environmental test items are thermal cycling, humidity-freeze and a damp heat test. Thermal cycling is intended to test the effects of thermal stress in both the solar cells and the module. The humidity-freeze test measures the effect of thermal stress in the presence of high humidity. The damp heat test is the test for resistance of long term (1000 hours) exposure to high temperature (85 $^{o}$C) and high humidity (85% relative humidity) [12]. The failure rate of the combination of thermal cycles and damp heat can be as much as 70% [12]. Additionally, a light soaking test is required for thin film solar cell [14]. Light soaking is an examination of the stability of prolonged exposure to irradiance. The solar cell efficiency should not be change more than 2% after two consecutive 43 kWh/m$^2$ irradiance. Thus, understanding the degradation mechanisms as a function of environmental conditions is important to improve the reliability of solar cells.

In this chapter, we examined the degradation mechanisms of CIGS solar cell which were fabricated on the stainless steel substrates. The CIGS solar cells were exposed in the air for 1000 hours under moderate temperature, 85 $^{o}$C, 125 $^{o}$C and 150 $^{o}$C. The solar cells performance and trap characteristics were compared before and after air annealing. The metastability of the solar cells also examined.

### 3.2. Measurement and characterization.

CIGS solar cells were fabricated by a standard roll to roll process on stainless steel substrates and supplied by Dow chemical. Four solar cell samples with same area (0.416 $cm^2$) were obtained by cutting a single large substrate. The performance of all four cells was similar before air annealing. To measure the effect of anneal temperature, samples were annealed in the air for 1000 hours at 85 $^oC$, 125 $^oC$ and 150 $^oC$, respectively.

The current–voltage (I-V) characteristics were measured using an Agilent 4155 semiconductor parameter analyzer. Solar cell performance was measured using a Newport 96000 full spectrum solar simulated with AM 1.5 filter under 1sun illumination intensity. Thermal admittance spectroscopy was performed in a Janis ST-500 cryogenic micro probestation with liquid nitrogen cooling to characterize the traps. We measured the admittance of solar cells with an Agilent 4294A precision impedance analyzer in the range of 100Hz to 4MHz.

### 3.3. Results and discussion.

#### 3.3.1 Solar cell performance and DC characteristics.

Figure 3.1 show the post-anneal current-voltage (I-V) characteristics under dark and 1 sun illumination. The solar cell performance was extracted from this data. The values of the parasitic elements are shown in Table 3.1. With increasing air anneal temperature, the efficiency degrades from 7.74% to 7.14% (-7.76%), 6.24% (-19.4%) and

5.18%(-33.1%) at 85 $^{o}$C, 125 $^{o}$C and 150 $^{o}$C, respectively. The fill factor, open circuit voltage, and shunt resistance were significantly decreased by 12.28% (-19.2%), 60 mV (-10.5%), and 773 $\Omega/cm^2$ (-85%), respectively, after 150 $^{o}$C annealing as shown in Table 3.1.

From the dark I-V characteristics, the current at low bias (<0.4V) increased significantly with increasing temperature (Figure 3.1 (b)). The shunt resistances also decreased from 2376 $\Omega/cm^2$ to 206 $\Omega/cm^2$ for the 150 $^{o}$C annealed sample. The I-V characteristics at low bias were matched well with Fowler-Nordheim (F-N) tunneling characteristics. The increase of F-N tunneling degraded the shunt resistance under illumination because the shunt resistances in the dark and in illumination were found to be linearly correlated. With increasing F-N tunneling current, the ideality factor increased from 2.39 to 4.35 after a 150 $^{o}$C annealing. Because of the superposition of two current mechanisms - Shockley-Reed-Hall recombination and F-N tunneling, the ideality factor of the diodes increased to more than 2. The increase of reverse saturation current was due to the increase of the ideality factor. The series resistances of all annealed samples more than doubles after the anneal. The series resistances are inversely correlated with the carrier concentration as extracted by capacitance-voltage (C-V) measurements. Low carrier concentrations in the CIGS layers of the annealed samples increased the series resistance. We will discuss the carrier concentration and profile in the next section. The degradation of the fill factor by annealing was due to both the increase of series resistance by reduced carrier concentration and the decrease of shunt resistance by F-N tunneling.

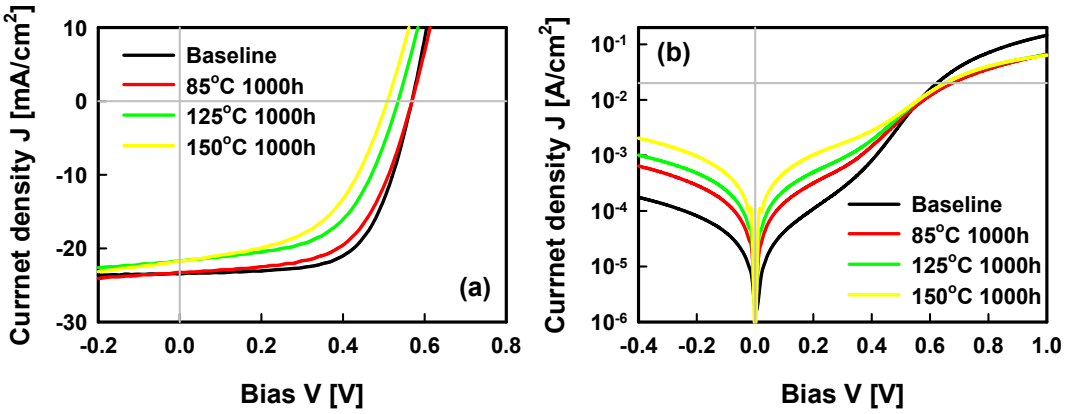


Figure 3.1. Current-voltage characteristics of CIGS solar cells under (a) AM 1.5 1 sun illumination and (b) dark.

Table 3.1. Solar cell performance and parasitic elements characteristics.

| | | Baseline | 85°C | 125°C | 150°C |
|---|---|---|---|---|---|
| Illumination | $V_{OC}$ [V] | 0.569 | 0.569 | 0.542 | 0.509 |
| | $J_{SC}$ [mA/cm$^2$] | 21.33 | 21.13 | 19.76 | 19.79 |
| | FF [%] | 63.77 | 59.2 | 58.24 | 51.49 |
| | Efficiency [%] | 7.74 | 7.12 | 6.24 | 5.18 |
| | Shunt R [Ωcm$^2$] | 863 | 287 | 189 | 130 |
| Dark | $J_0$ [μA/cm$^2$] | 1.16 | 12.52 | 22.31 | 69.33 |
| | Ideality factor A | 2.39 | 3.27 | 3.52 | 4.35 |
| | Shunt R [Ωcm$^2$] | 2376 | 716 | 427 | 206 |
| | Series R [Ωcm$^2$] | 1.89 | 4.17 | 4.24 | 3.69 |

### 3.3.2. Carrier profile.

Figure 3.2 show the carrier profiles of solar cells at 296 K and 128 K. Carrier profiles were extracted from 1 MHz capacitance-voltage (C-V) characteristics and calculated by

$$p = \frac{1}{q\varepsilon}\frac{1}{\frac{d}{dV}\left(\frac{1}{C^2}\right)}, \quad [\mathrm{cm}^{-3}] \tag{3-1}$$

where, $p$, $q$, $\varepsilon$, and $C$ are carrier concentration, electric charge, relative dielectric constant and junction capacitance, respectively. The carrier concentrations of samples at 298 K were $6.44\text{x}10^{15}$ $\mathrm{cm}^{-3}$, $1.04\text{x}10^{15}$ $\mathrm{cm}^{-3}$, $7.53\text{x}10^{14}$ $\mathrm{cm}^{-3}$, and $2.67\text{x}10^{15}$ $\mathrm{cm}^{-3}$ of before anneal (baseline), 85 $^{o}$C, 125 $^{o}$C and 150 $^{o}$C annealed samples at the depletion edge of 0 V applied. Carrier concentrations were increased with increasing depth. The depletion widths were inversely proportional to the carrier concentrations. The depletion widths were 0.51 μm, 0.82 μm, 1.06 μm and 0.59 μm for the baseline, 85 $^{o}$C, 125 $^{o}$C and 150 $^{o}$C annealed samples, respectively. The temperature dependences of the depletion width between before and after annealing were different. The depletion width of the unannealed sample increased 27% when cooling from room temperature to 128 K however the depletion widths of the annealed samples increased an average of 120% for the same temperature difference. When the thermal activation energy of carriers or traps is low (< tens meV), the increase of the depletion width at low temperature is due to the built-in potential increase because the traps are fully activated. However, when the activation energy of carriers is high, the depletion width depends on the ratio of low activation energy traps to high activation energy traps as explained in the previous chapter. Thus,

the dominant carriers in the unannealed sample have a low activation energy such as that due to Cu vacancies ($V_{Cu}$), while the activation energies of dominant carriers in the annealed samples are high activation energy. That is to say, deep traps.

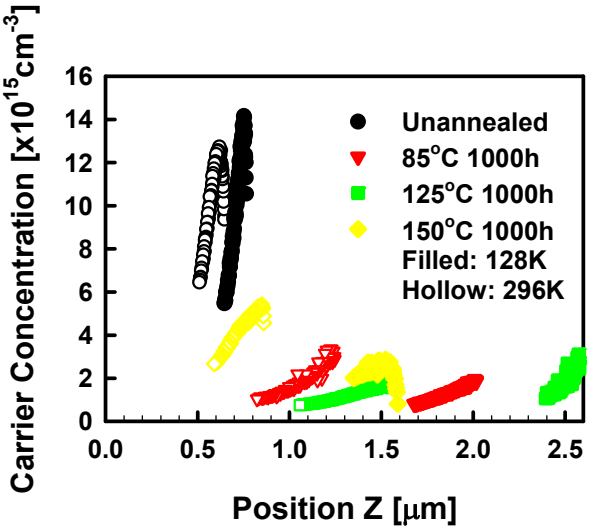


Figure 3.2. Carrier profiles of unannealed, 85 °C, 125 °C and 150 °C annealed samples

In the early stage of CIGS research, the air anneal process was found to increase the PV efficiencies significantly by increasing the carrier concentration [15,16]. The oxygen atoms passivated the Se vacancy ($V_{Se}$) at the surface or along grain boundaries [17]. The presence of Na at the grain boundary assists oxygen passivation reactions through catalysis [18]. Thus, carrier concentrations were increased by removing n-type traps and efficiencies were improved [18]. However, as the process technologies of CIGS improved, such as three stage process, oxidation (or oxygenation) effects on the efficiency of solar cells were found to not be significant [19].

However, in these results, the oxidation process reduced the majority carrier concentration significantly signaling low activation energy traps. There are two possibilities for the majority carrier concentration reduction. One is that oxygen atoms passivate the $V_{Cu}$ , which is believed to be the primary acceptor in CIGS. The other is that minority carrier traps are generated. In the latter case, two kinds of defects can be considered: the Cu interstitial ($Cu_i$) and the In anti-site on Cu ($In_{Cu}$) since Se vacancy ($V_{Se}$) might be passivated by oxygen atoms [18]. Since $Cu_i$ is a mobile defect in CIGS, we can distinguish between these defects with a metastability test [20,21].

### 3.3.3. Trap characteristics.

Figure 3.3 show the junction capacitance characteristics of four samples as a function of measurement temperature and frequency. Two kinds of traps are seen. The first exhibits a broad transition in high capacitance regime. These are generally called N2 traps. The second show a steep transition in the low capacitance regime. These are generally called N1 traps. The solar cell shows only N2 trap characteristics before annealing (Baseline cell) as shown in Figure 3.3 (a). N1 traps were developed in the annealed samples. The capacitance transitions by traps increased with increasing anneal temperature. N1 and N2 were majority traps since the ratio of the capacitance change to the high frequency capacitance was higher than 0.12. The minimum $\Delta C/C$ ratio was 0.71 by N1 traps in the 85 $^{o}$C annealed sample.

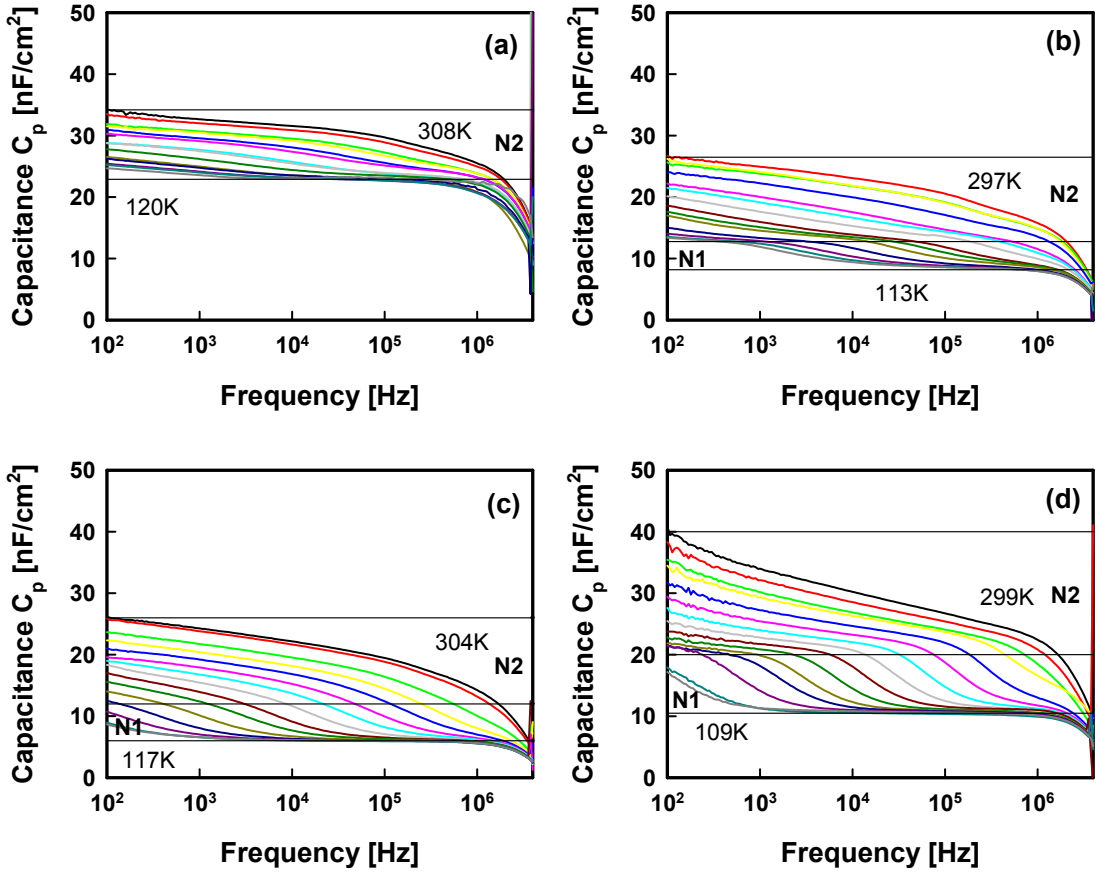


Figure 3.3. Thermal capacitance characteristics of (a) unannealed (baseline), (b) 85 $^{o}$C, (c) 125 $^{o}$C, and (d) 150 $^{o}$C annealed samples.

The activation energies and capture rate of each solar cells were extracted from Arrhenius plots of $\omega_0/T^2$ vs q/kT as shown in Figure 3.4. The trap characteristics are summarized in Table 3.2. In 125 $^{o}$C and 150 $^{o}$C annealed samples, we could not extract inflection points in capacitance-frequency characteristics due to N2 traps. The activation energy of the N2 traps in the baseline solar cell was 0.288eV. According to the research of Zhang et al, the activation energy of these traps is close to the activation energy of the Cu anti-site on In ($Cu_{In}$) defect which are well known p-type deep traps in CIGS films

[22]. The activation energy of the $Cu_{In}$ defect is 0.3 eV. The traps had a Gaussian energy profile with a total trap concentration of $6.66\times10^{15}$ $cm^{-3}$. At 85 $^{o}$C, the activation energy of the N2 trap was 0.563 eV, almost at midgap. The activation energy of the newly generated N1 trap was 0.124 eV. The total trap concentrations of the N1 and N2 traps were $5.11\times10^{15}$ $cm^{-3}$ and $9.92\times10^{15}$ $cm^{-3}$, respectively. The activation energies of the N1 and N2 traps in the 85 $^{o}$C annealed solar cell were close to the activation energy of the In vacancy ($V_{In}$) and the double charged Cu anti-site on In ($Cu_{In}$(-/2-)). The activation energies of the N1 traps for the 125 $^{o}$C and 150 $^{o}$C annealed samples were 0.271 eV and 0.251 eV respectively. Their energies were close to the N2 traps in the baseline solar cell. Majority (acceptor like) traps with the activation energy near 0.25 ~ 0.27 eV is believed to be Cu anti-sites on In ($Cu_{In}$). The total trap concentrations of 125 $^{o}$C and 150 $^{o}$C annealed samples were $5.73\times10^{15}$ $cm^{-3}$ and $1.11\times10^{16}$ $cm^{-3}$, respectively.

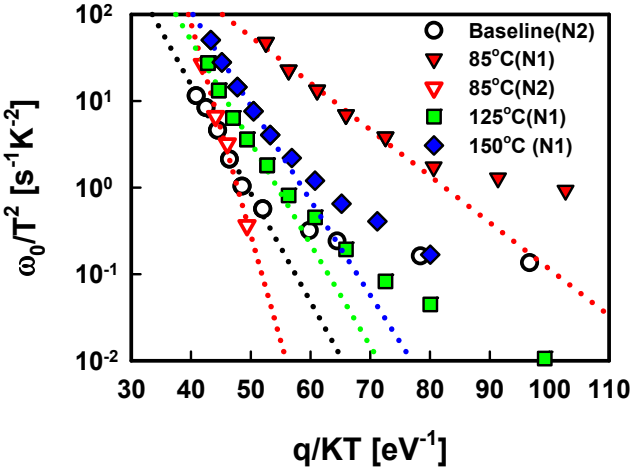


Figure 3.4. Arrhenius plot of $\omega_0/T^2$ vs q/kT of unannealed, 85 $^{o}$C 125 $^{o}$C, and 150 $^{o}$C annealed samples.

Figure 3.5 show the trap profiles of all of the traps. The activation energies of N2 in the baseline cell and N1 in the 85 $^{o}$C and 125$^{o}$C annealed solar cells were similar (0.251 eV ~ 0.288 eV), however, standard deviations of trap distributions were reduced with increasing annealing temperature and the profiles became more sharp.

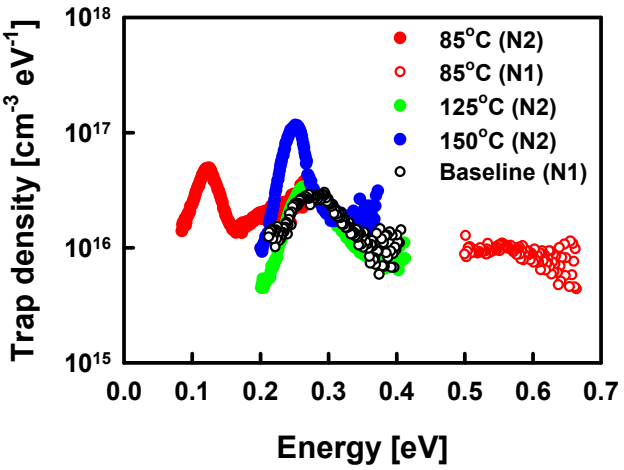


Figure 3.5. Trap distribution of baseline, 85 $^{o}$C 125 $^{o}$C, and 150 $^{o}$C annealed samples.

Comparing carrier and trap concentrations, the carrier concentrations are comprised of shallow traps ($V_{Cu}$) and deep traps ($Cu_{In}$). Since the activation energy of the deep traps is high about 0.251 ~ 0.288 eV, they are only partially activated. Thus, only part of total deep trap concentration contributes to carrier concentration. If we know the deep trap characteristics then the concentration of the shallow traps can be calculated.

In the baseline solar cell, the carrier concentration was $6.44\times10^{15}$ cm$^{-3}$. This concentration was the sum of the fully activated shallow traps ($V_{Cu}$) and part of the deep

traps concentration ($Cu_{In}$). When the activation energy and density are 0.288 eV and $6.66\times10^{15}$ $cm^{-3}$, by numerical calculation the carrier concentration by the deep trap is $1.06\times10^{15}$ $cm^{-3}$ and the concentration of shallow traps is $6.25\times10^{15}$ $cm^{-3}$. Since the shallow trap concentration is comparable to the deep trap concentration, the depletion width does not change much with temperature.

The trap concentration and activation energy of the 125 $^{o}$C annealed solar cell was similar to the baseline sample, however the carrier concentration was $7.53\times10^{14}$ $cm^{-3}$. This means that about $5.8\times10^{15}$ $cm^{-3}$ shallow traps were eliminated after annealing. In the same manner, the reduced shallow traps concentration of the 150 $^{o}$C annealed solar cell was about $6.25\times10^{15}$ $cm^{-3}$. The air anneal reduced the carrier concentration significantly.

Table 3.2. Trap characteristics of baseline, 85 $^{o}$C 125 $^{o}$C, and 150 $^{o}$C annealed samples.

| | Admittance spectroscopy | | | | | |
|---|---|---|---|---|---|---|
| | Type | Energy [eV] | Trap Conc. [$cm^{-3}$] | Standard Deviation [eV] | Defect Index | Carrier Concentration [$cm^{-3}$] |
| Baseline | N2 | 0.288 | $6.66\times10^{15}$ | 0.052 | $Cu_{In}$(-/0) | $6.44\times10^{15}$ |
| 85$^{o}$C, | N2 | 0.563 | $9.92\times10^{15}$ | 0.149 | $Cu_{In}$(2-/-) | $1.04\times10^{15}$ |
| | N1 | 0.124 | $5.11\times10^{15}$ | 0.020 | $V_{In}$ | |
| 125$^{o}$C, | N1 | 0.271 | $5.73\times10^{15}$ | 0.034 | $Cu_{In}$(-/0) | $7.53\times10^{14}$ |
| 150$^{o}$C, | N1 | 0.251 | $1.11\times10^{16}$ | 0.018 | $Cu_{In}$(-/0) | $2.67\times10^{15}$ |

### 3.4. Metastability.

To analyze the reason for the carrier concentration reduction by air annealing, we examined the carrier profile change by bias stress. If carrier concentration decrease is due to mobile charges such as $Cu_i$, carrier profile will change under an applied bias while fixed traps such as $In_{Cu}$, or the $V_{Cu}$ passivation by oxygen atoms cannot the change carrier distribution by an applied bias. At thermal equilibrium, a built-in field is formed near the junction. As a result, mobile ions are depleted by drift. However, when a bias or light is applied to the solar cells, the electric field distribution is changed. Mobile charges move with the electric field and carrier profiles are changed.

The measurement performed in a vacuum chamber to prevent additional reaction with air. The measurement temperature was 80 $^{o}$C to increase the mobility of mobile charges.

First, we measured the initial carrier profiles by C-V measurement and applied a -1 V reverse bias to the junction. Keeping the field in place, we measured the carrier profile every 5 minutes until no further changes were observed. Then we applied +1 V forward bias and measured the profile every 5 minutes until once again no further changes were observed. Profiles saturated after 2 hours in reverse bias and 30 minutes in forward bias. We repeated this measurement cycle 4 times and obtained same carrier profile change. When the solar cells were left in thermal equilibrium, the carrier profiles recovered to their initial condition after 12 hours.

Figure 3.6 show the carrier profile changes of the baseline and 150 $^{o}$C annealed solar cells before and after bias stress. The carrier profiles of baseline sample were not

changed by bias stress. However, the carrier profiles of 150 °C annealed sample were significantly changed by bias stress. The carrier density decreased after the forward bias stress and increased after the reverse bias stress at positions more than 0.25 μm from the junction. The carrier densities of the initial, after forward bias stress and after reverse bias stress at 0.4 μm were $4.8\times10^{15}$ $cm^{-3}$, $2.5\times10^{15}$ $cm^{-3}$, and $1.2\times10^{16}$ $cm^{-3}$, respectively. The charge distribution characteristics due to bias were the same as previously reported for metastable CIGS [23]. The density difference between the after reverse bias stress and thermal equilibrium was $7.2\times10^{15}$ $cm^{-3}$ at 0.4 μm from the junction. This density is similar with the reduced carrier concentration after 150 °C annealing. Thus, the reduced carriers by air anneal may be related to the metastable state carriers.

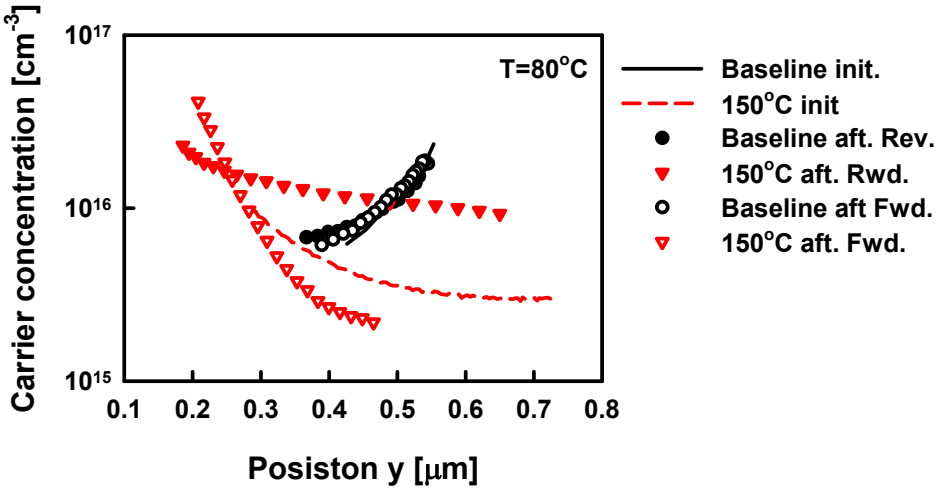


Figure 3.6. Carrier profiles of baseline and 150 °C annealed samples before and after 20 minutes forward and 2 hours reverse bias stress.

There are two models for metastabilty of CIGS solar cells [24,25]. The first is the mobile Cu ion model. The second invokes the bi-stable states of ($V_{Cu}$-$V_{Se}$) defect complexes. In the mobile Cu ion model, positively charged interstitial Cu ($Cu_i$) defects move in response to an electric field, changing the charge distribution. When forward bias is applied, $Cu_i$ defects move toward the junction interface so the net hole concentrations decrease near the junction interface. Under reverse bias, $Cu_i$ defects move toward the back contact, thus the net hole density is increased. In the bi-stable states of ($V_{Cu}$-$V_{Se}$) defect complexes model ($V_{Cu}$-$V_{Se}$) defect complexes can be two stable states: shallow donor and acceptor states. According to the research of Kazmerski et al., the oxidation process in $CuInSe_2$ (CIS) forms $In_2O_3$ and $SeO_2$. No Cu oxides were observed. $CuSe_x$ forms near the oxide-CIS interfaces [26,27]. Cu ions may be generated and redistributed by oxidation [24]. In the oxidation process, oxygen atoms mostly passivate the $V_{Se}$ defects. This increases the acceptor carrier concentrations since the $V_{Se}$ defect acts as a donor. Thus it is difficult to generate $V_{Se}$ and form ($V_{Cu}$-$V_{Se}$) defect complexes by an oxidation process. Therefore the mobile interstitial Cu defects model well explains the observed metastability in our CIGS solar cells caused by oxidation.

Figure 3.7 show the metastable I-V characteristics and performance changes with time, comparing before and after 150 $^oC$ annealed solar cells. Solar cells were exposed to AM 1.5 1 sun radiation for 1 hour and the solar cell performance was measured every 5 minutes. The performance and I-V characteristics of the baseline solar cell did not change after 1 hour of illumination as shown in Figure 3.7 (a) and (b). The performance of the 150 $^oC$ annealed solar cells improved 8.9% after 1 hour of illumination. The

improvement was mostly due to a fill factor increase as shown in Figure 3.7 (b) and (d). The series resistance decreased, thus the current increased at 1 V as shown in Figure 3.7 (a). Light illumination moves the Cu ions toward the junction interface so the carrier concentration at the back contact might be increased. Thus, series resistance is decreased and the fill factor increased.

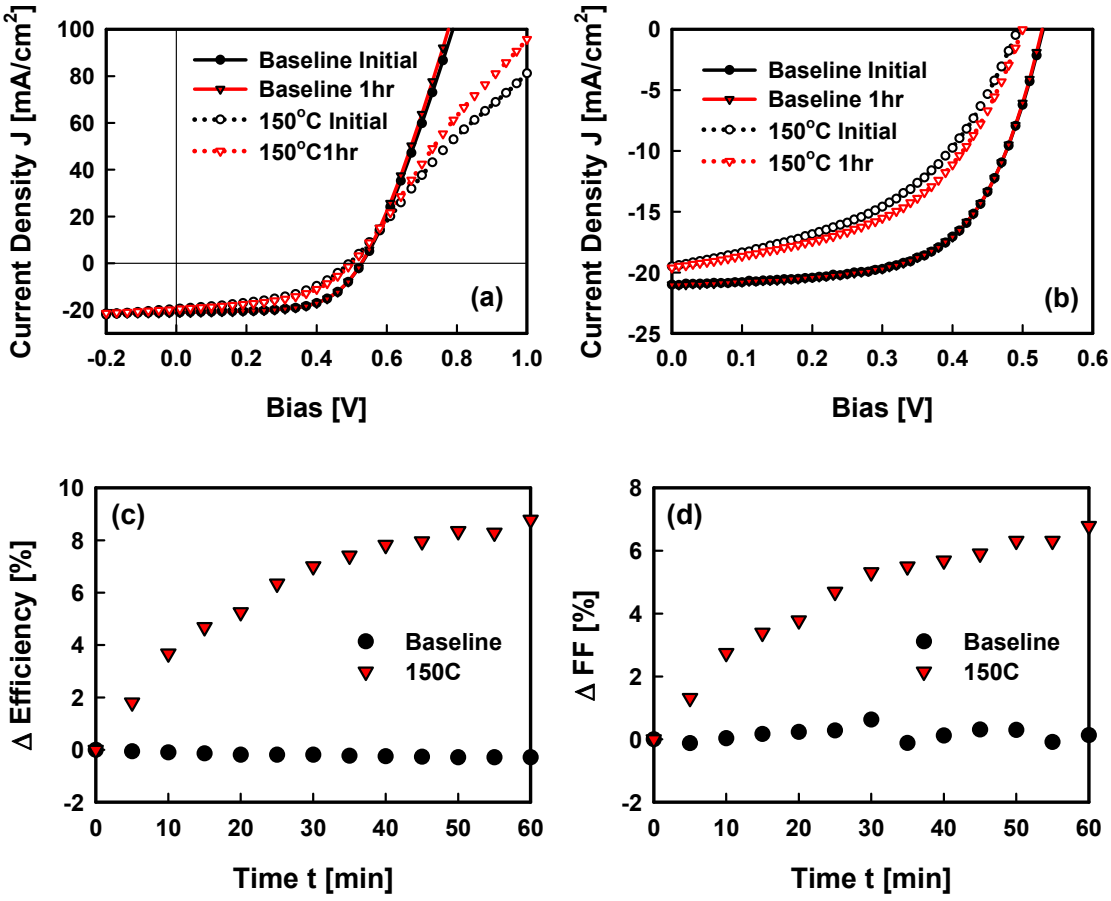


Figure 3.7. I-V characteristic of baseline and 150 °C annealed solar cells before and after 1 hour illumination (a) in large scale, (b) in small scale. And (c) efficiency and (d) fill factor change by time.

### 3.5. Conclusion.

We examined the effect of air anneals on CIGS solar cells. With increasing air anneal temperature, the efficiencies of solar cell decreased, ultimately going from 7.74% to 5.18% after a 150 $^{o}$C 1000 hour anneal. The increase of F-N tunneling current and series resistance degraded both the fill factor and the efficiency significantly. The activation energies of traps were 0.251 eV ~ 0.288 eV except for the 85$^{o}$C annealed sample. Majority traps are presumed to be Cu anti-site on In ($Cu_{In}$). The trap densities were similar density until the 125 $^{o}$C anneal. After the 150 $^{o}$C anneal, they increased almost by a factor of two from $6.44\times10^{15}$ $cm^{-3}$ to $1.11\times10^{16}$ $cm^{-3}$ comparing to before the anneal. The air anneal reduced the carrier concentrations even though the majority trap densities were similar or increased after the 150 $^{o}$C anneal. The minority traps generated by air anneal appear to have compensated the majority carriers. Metastable minority defects appear to have been generated by anneals, causing metastabilty in the CIGS solar cells after the 150 $^{o}$C anneal. Since oxidation is believed to passivate $V_{Se}$ defects and Cu ions can be generated by oxidation at the grain boundaries, it is reasonable to consider the effects on each. The interstitial Cu defect ($Cu_i$) model does a good job of explaining the observed metastability in CIGS solar cells after long oxidations. $Cu_i$ defects compensate the majority carriers reducing the carrier concentration.

**References**


[1] K. Branker, M. J. M. Pathak, J. M. Pearce, Renew. Sust. Energ. Rev. 15 (2011) 4470–4482.

[2] A. Luque, Handbook of Photovoltaic Science and Engineering, John Wiley & Sons, West Sussex, England, 2003.

[3] D. C. Jordan, S. R. Kurtz, Prog. Photovolt.: Res. Appl. 21 (2013) 12–29.

[4] T. Saitoh, H. Hashigami, S. Rein, S. Glunz, Prog. Photovolt.: Res. Appl. 8 (2000) 426-436

[5] A. Romeo, M. Terheggen, D. Abou-Ras, D. L. Bätzner1, F.-J. Haug, M. Kälin, D. Rudmann, A. N. Tiwari, Prog. Photovolt.: Res. Appl.12 (2004) 93–111.

[6] S.-i. Sato, H. Sai, T. Ohshima, M. Imaizumi, K. Shimazaki, M. Kondo, Prog. Photovolt.: Res. Appl. 21 (2012).

[7] T. J. McMahon, Prog. Photovolt.: Res. Appl. 12 (2004) 235–248.

[8] S. Hegedus, Prog. Photovolt.: Res. Appl. 14 (2006) 393–411.

[9] B. Dimmler, M. Powalla, H. W. Schock, Prog. Photovolt.: Res. Appl. 10 (2002) 149–157

[10] M. Woodhouse, A. Goodrich, R. Margolis, T. James, R. Dhere, T. Gessert, T. Barnes, R. Eggert, D. Albin, "Perspectives on the pathways for cadmium telluride photovoltaic module manufacturers to address expected increases in the price for tellurium", Sol. Energy Mater. Sol. Cells, (2012) in press.

[11] EIA. Average price of photovoltaic cells and modules, 2002-2011.

[12] Tüv, Basic understanding of IEC standard testing for photovoltaic panels, Peabody,.

[13] IEC, standard IEC 61215.

[14] IEC, standard IEC 61646.

[15] R. A. Mickelsen, W. S. Chen, Proceedings of 15th IEEE Photovolt. Spec. Conf., 1981, 800 - 804.

[16] R. Noufi, P. Souza, C. Osterwald, Solar Cells, 15 (1985) 87 - 91

[17] D. Cahen, R. Noufi, Appl. Phys. Lett., 54 (1989) 558-560.

[18] L. Kronik, D. Cahen, H. W. Schock, Adv. Mater. 10 (1998) 33-36.

[19] S. Kijima, T. Nakada, Appl. Phys. Express 1 (2008) 075002.

[20] K. Gartsman, L. Chernyak, V. Lyahovitskaya, D. Cahen, V. Didik, V. Kozlovsky, R. Malkovich, E. Skoryatina, V. Usacheva, J. Appl. Phys. 82 (1997) 4282-4285.

[21] L. Chernyak, K. Gartsman, D. Cahen, O. M. Stafsudd, J. Phys. Chem. Solids 56 (1995) 1165-I 191.

[22] S. B. Zhang, S.-H. Wei, A. Zunger, Phys. Rev. B. 57 (1998) 9642-9656.

[23] R. Herberholz, H.W. Schock, U. Rau, J.H.Werner, T. Haalboom, T. Godecke, F. Ernst, C. Bleilharz, K.W. Benz, D. Cahen, Proceedings of 26th IEEE Photovolt. Spec. Conf., 1997, Anaheim, 323-326.

[24] U. Rau, D. Braunger, R. Herberholz, H. W. Schock, J.-F. Guillemoles, L. Kronik, D. Cahen, J. Appl. Phys., 86 (1999) 497-505.

[25] S. Lany, A. Zunger, J. Appl. Phys. 100 (2006) 113725.

[26] L. L. Kazmerski, O. Jamjoum, P. J. Ireland, S. K. Deb, R. A. Mickelsen, W. Chen, J. Vac. Scl. Technol., 19 (1981) 467-471.

[27] L. L. Kazmerski, O. Jamjoum, J. F. Wager, P. J. Ireland, K. J. Bachmann, J. Vac. Sci. Technol. A, 1 (1983) 668-669.

# Chapter 4

## Heteroepitaxy and solar cell performance of Copper Indium Gallium Diselenide solar cells

### 4.1. Introduction.

$CuIn_{1-x}Ga_xSe_2$ (CIGS) solar cells are one of the most promising solar cells due to the high efficiency and the potential for very low cost thin films solar cells [1,2]. CIGS solar cells have already achieved an efficiency of 20.3% which is the highest value among lab scale thin film solar cells [3]. The ability to vary the band gap of CIGS can be used to tune the material for the theoretical maximum efficiencies of single and multi junction solar cells. The band gaps ($E_g$) of CIGS are variable from 1.01 eV to 1.68 eV through the Ga/(In+Ga) composition ratio. The band gaps of single and tandem junction solar cells for the theoretical maximum efficiency are 1.4 eV, by Shockley-Quisser model [4] and 1.64 eV for top cells [5]. Since the band gap of the highest efficiency CIGS solar cells is around 1.1 eV where the Ga composition (x) is about 0.3 ~ 0.35, the efficiency of a single junction CIGS solar cell is expected to be more improved by increasing the band gap. Much research has been performed on wide band gap CIGS solar cells however the efficiencies of these devices were always lower than those of devices with a band gap closer to 1.1 eV [6-9].

The open circuit voltage ($V_{OC}$) is the most significant problem in wide band gap CIGS solar cells [9-11]. Ideally, $V_{OC}$ is equal to the band gap less an offset voltage which is typically 0.2 to 0.3 V. In CIGS solar cells, $V_{OC}$ follows this relationship when $E_g < 1.3$ eV however it saturates at 0.7 ~ 0.8 V when $E_g > 1.4$. $V_{OC}$ saturation is often explained by a high recombination velocity at the CdS/CIGS interface. However, the detailed mechanism is not well understood [12,13]. Grain size also can be a reason for low efficiency since large grain sizes are obtained around x = 0.3. However, even when grain sizes are large at high Ga composition through the use of high process temperatures, the efficiencies of wide band gap $CuGaSe_2$ (CGS) solar cells are less than 10% [14,15].

CIGS films do not grow with a random grain orientation. The preferred orientation of CIGS films actually has more of an effect on efficiency than the grain size. (220/204) oriented films have higher efficiency compared to (112) direction films at same Ga composition [16,17]. The potential change at the grain boundaries due to the preferential orientation of the films is one of the models used to explain the effects of orientation on efficiency [18]. However, the effects of grain boundary potential on efficiency are inconsistent [19]. Recently, it was demonstrated that the preferred orientation strongly depend on the crystal orientations of sub layers [20]. The reasons for high efficiency in (220/204) films, however, are still unclear.

We examine the effects of heteroepitaxy between layers in CIGS solar cells to explain these effects. We perform bulk and interface trap densities modeling based on the dislocation generation through the stress of lattice mismatch between the layers and investigate the effects of bulk and interface trap models on the solar cell performances

using numerical device simulation. Finally, we compare these predictions to experimental results.

### 4.2. Heteroepitaxy between CIGS and $MoSe_2$.

In the conventional high efficiency processes for CIGS solar cells, 0.5 ~ 1.0 μm of Mo is deposited on various substrates by sputtering, 2.0 ~ 2.5 μm p-type CIGS films are deposited on the Mo layer by a thermal co-evaporation process, and 70 nm n-type CdS is deposited on CIGS by chemical bath deposition (CBD) to form p-n junction with CIGS. 150 nm of ZnO:Al, and 100 nm ZnO are then deposited on the CdS to act as low resistance window layers. Mo is an important layer for achieving low back contact and series resistances [21]. A $MoSe_2$ layer is formed at the interface between Mo and CIGS during CIGS deposition [22,23]. The low band gap $MoSe_2$ greatly reduces the contact resistance with CIGS compared to other metals [24,25]. The $MoSe_2$ layer not only reduces resistance, it also influences the crystal structure of the CIGS film. Contreras et al. showed that the growth of (204) oriented CIGS strongly depended on the Mo structure [26]. Shin et al. demonstrated that (220) preferred orientation CIGS films grew on (100) $MoSe_2$ while (112) oriented CIGS films grew on (002) $MoSe_2$ [20]. In a three-stage process [27], which produces the highest efficiency devices, $(In,Ga)_2Se_3$ films are deposited on Mo in first stage and CIGS films are formed after $Cu_2Se$ deposition on $(In,Ga)_2Se_3$ films. The preferred orientations of hexagonal $(In,Ga)_2Se_3$ films also depends on the crystal structure of $MoSe_2$. (006) and (300) oriented $(In,Ga)_2Se_3$ films were grown on (002) and (100) $MoSe_2$ respectively, matching the directions of the underlying crystal

orientations [20]. The epitaxial relationship between CIGS and $MoSe_2$ affects the orientations and also performances of CIGS solar cells. Thus, we investigate the lattice mismatch between CIGS and $MoSe_2$.

In polycrystalline film growth, the films are typically comprised of random orientated grains and, generally, the reaction between grains and grain boundaries are supposed to be more important than the influence of the substrate. However, in the grown films textured with sub layers, the epitaxial relationship can affect the film characteristics. Especially if the grain size is large, the epitaxial relationship is more important. The grain size of high efficiency CIGS films are about 1um suggesting that the orientations of CIGS films are affected strongly by the orientation of the substrate. Thus, heteroepitaxy between CIGS and $MoSe_2$ is important.

### 4.2.1. Lattice mismatch.

In heteroepitaxy, the lattice mismatch between the two layers is extremely important because it affects both layer adhesion and dislocations at the hetro material interface. Threading dislocations due to interface dislocations directly affect the bulk trap density.

The crystal structure of 2H-$MoSe_2$ is hexagoanal with a space group of $P6_3/mmc$. The lattice constants of 2H-$MoSe_2$ used in this work are

$$a = 3.2910 + 2.382\times10^{-5}\times T + 1.18\times10^{-9}\times T^2 \quad [\text{Å}] \quad (4\text{-}1)$$

$$c = 12.9288 + 1.672\times10^{-4}\times T - 4.987\times10^{-8}\times T^2 \quad [\text{Å}] \quad (4\text{-}2)$$

where T is temperature in Celsius. At 293 K a and c are 3.292 Å and 12.936 Å respectively [28].

The lattice constants for chalcopyrite CIGS depend on the Ga/(In+Ga) ratio [29]. In this work, we used following lattice constants of $Cu_{1-y}(In_{1-x}Ga_x)_{1+y/3}Se_2$ [30].

$$a = 5.765 - 0.164x - 6.6910^{-2}\,y \quad [\text{Å}] \tag{4-3}$$

$$c = 11.557 - 0.555x - 0.134y \quad [\text{Å}] \tag{4-4}.$$

CIGS films are generally Cu deficient to prevent metallic $CuSe_2$ phase formation. This deficiency shrinks the lattice constants of CIGS. The Cu deficiency lattice shrink parameters are found in Ref 31 [31]. In this work, we assumed Cu composition y = 0.9.

The lattice misfit (*f*) is defined as

$$f = \frac{d_{CIGS} - d_{MoSe_2}}{d_{MoSe_2}} \ [\%] \tag{4-5}$$

where, $d_{CIGS}$ and $d_{MoSe_2}$ are lattice constant of CIGS and $MoSe_2$ respectively.

Since the crystal structure of CIGS and $MoSe_2$ are different, respectively, chalcopyrite and hexagonal structures, the possible combinations of lattice matched structures of CIGS and $MoSe_2$ are (112) CIGS and c-plane (001) $MoSe_2$ and (n l m) CIGS where n×l×m=0 and m- (100), a- (110), or r- (102) plane $MoSe_2$. Thus, the lattice of (110) CIGS can be matched with m-, a-, or r-plane $MoSe_2$. We found a well matched combination for (110) CIGS with lattice constants of 35.08$^o$ rotated (110) CIGS and the m-plane (100) and r-plane (102) $MoSe_2$ as shown in Figure 4.1. The rotation angle was calculated by CrystalMaker. The definition of the short ($d_a$) and long lattice spacings ($d_c$) of CIGS are shown in Figure 4.1 (c).

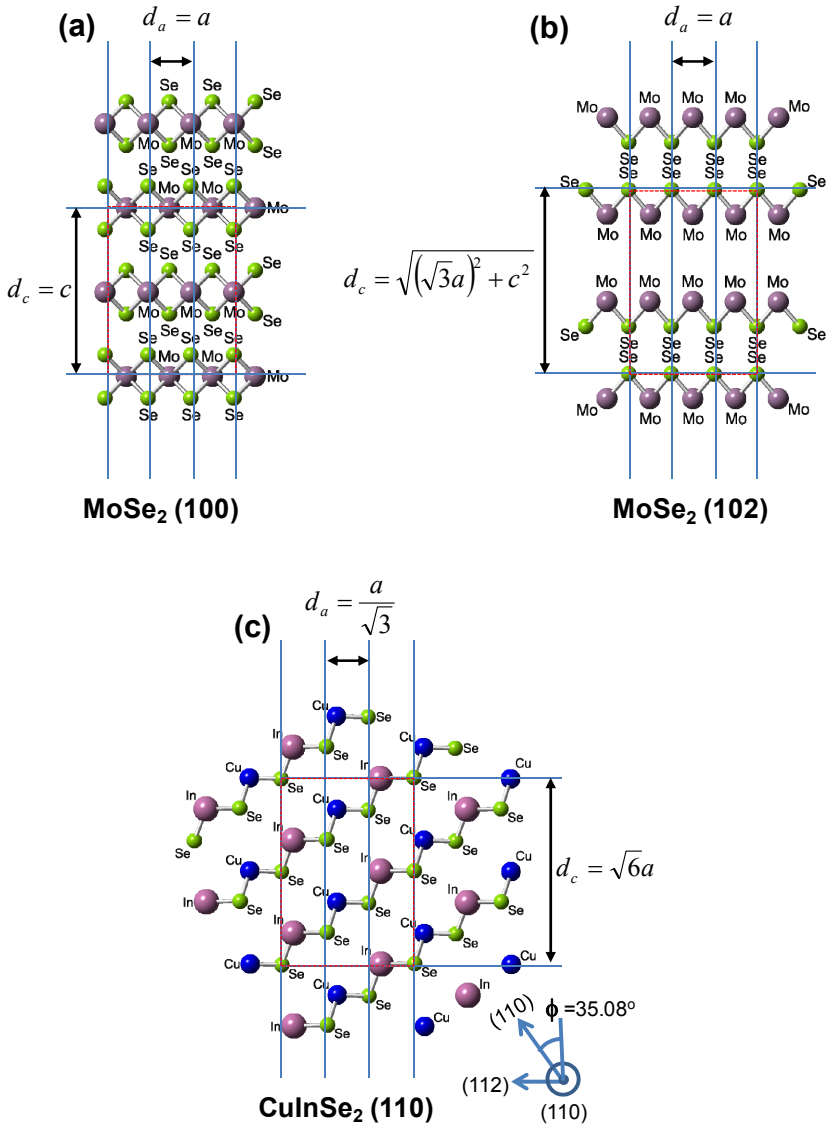


Figure 4.1. Plane views of crystal structures of (a) (100) $MoSe_2$, (b) (102) $MoSe_2$ and (c) 35.08° rotated (110) $CuInSe_2$.

Since CIGS films are deposited at 500~600 °C, thermal stress of CIGS films should be considered. The general layer stack of substrate before CIGS formation are

$(In,Ga)_2Se_3$, $MoSe_2$ and Mo films on soda-lime glass. The linear thermal expansion coefficients of each layer materials and CIS/CGS are shown in Table 4.1. The linear thermal coefficients of all materials are generally matched except Mo. Especially, the linear thermal coefficients of CIS/CGS, $(In,Ga)_2Se_3$ and $MoSe_2$ are very well matched thus we ignored thermal stress in CIGS films and considered only lattice mismatch between layers.

Table 4.1. Linear thermal expansion coefficients of materials in CIGS solar cell.

| Materials | Linear thermal expansion coefficients [$\times 10^{-6}\,K^{-1}$] | Materials | Linear thermal expansion coefficients [$\times 10^{-6}\,K^{-1}$] |
|---|---|---|---|
| $CuInSe_2$ | 10.5 [32] | Soda lime glass | 9~ [33] |
| $CuGaSe_2$ | 10.6 [32] | Mo | 5.2~5.7 [34] |
| $(In,Ga)_2Se_3$ | 10.8 [35] | $MoSe_2$ | 10.08 [28] |

Figure 4.2 shows the lattice misfits between 35.08$^o$ rotated (110) CIGS to m- and r-plane $MoSe_2$ as functions of the Ga composition of CIGS. In the short lattice spacing direction ($d_a$), the lattice constants of both m- and r- plane $MoSe_2$ were same, 3.292 Å, and the lattice constants of CIGS were 3.230 to 3.325 Å due to Ga composition. Lattice misfits in short spacing were from +0.99% at $CuInSe_2$ (CIS) to -1.89% at $CuGaSe_2$ (CGS). Positive misfit means the lattice constants of CIGS are larger than the lattice constants of $MoSe_2$. The lattice is matched at about x=0.35. In the long spacing direction ($d_c$), lattice mismatch between CIGS and m-plane (100) and r-plane (102) $MoSe_2$ are

different. The long lattice distances ($d_c$) of 35.08° rotated (110) CIGS were 13.539 ~ 14.125 Å while the m- and r-plane $MoSe_2$ were 12.936 Å and 14.137 Å respectively. Misfit in m-plane is larger than in r-plane. Lattice misfits of CIGS to m-plane and r-plane $MoSe_2$ were 4.66% to 9.19% and -0.08% to -4.23% respectively. (110) CIGS films on r-plane $MoSe_2$ had a smaller lattice misfit.

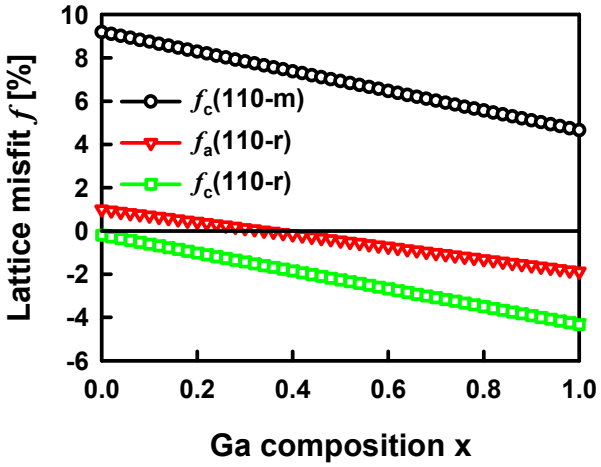


Figure 4.2. Lattice misfits between 35.08° rotated (110) CIGS and m-plane (100) and r-plane (102) $MoSe_2$ by Ga composition. $f_a$ is misfit in short spacing and $f_c$ is misfit in long spacing.

Comparing the lattice misfit of (110) and (112) CIGS, lattice misfits of (112) CIGS to c-plane (001) $MoSe_2$ were 20.16% to 23.69%. If template growth is indeed operative, the large lattice misfit of (112) CIGS films can result in a more defective poor quality film compared to the (110) CIGS film. Due to the resultant energy penalty, this growth orientation would not be preferred.

Regarding the preferred orientation of $MoSe_2$ with (110) CIGS, it is observed that (110) oriented CIGS films grew from m-plane $MoSe_2$ than r-plane $MoSe_2$ using X-ray diffraction [20]. In X-ray diffraction, the normalized intensity ($I/I_{max}$) of the (102) $MoSe_2$ pattern is 7.4% in powder diffraction so that it is difficult to observe in polycrystalline films. Since a large misfit strain stores high stress energy in deposited films, (110) CIGS films on r-plane $MoSe_2$ are stable because of low lattice misfits. Moreover, the lattice misfit characteristics of (110) CIGS grown on the m-plane does not match the dependence of trap densities and performance characteristics of CIGS solar cells with Ga composition. Generally, CIGS films with high Ga compositions are found to have large trap densities and low performance. However, the misfit of (110) CIGS on m-plane $MoSe_2$ in long lattice spacing direction decreases with increasing Ga composition while misfit of (110) CIGS on r-plane $MoSe_2$ increases. From the efficiency difference between (110) and (112) preferred CIGS films, a low lattice misfit is a high efficiency. In same manner, the misfits of (110) CIGS on r-plane $MoSe_2$ are preferred for high efficiency solar cells. Thus, we examined the trap properties of (110) CIGS films on r-plane $MoSe_2$.

### 4.2.2. Critical thickness ($h_c$), dislocation spacing ($p$) and trap densities.

The film thickness and lattice mismatch between CIGS and $MoSe_2$ are important parameters for generating misfit dislocations. A lattice mismatch creates a strain field in the deposited films. The elastic strain energy is accumulated by the strain field which is proportional to film thickness and the lattice mismatch. If the total energy - the summation of the elastic strain energy and the dislocation energy - is minimum

dislocations are generated. According to the Frank and van der Merwe energy criteria, dislocations begin to be generated when the film thickness reaches the value which makes the sum of the elastic strained energy due to lattice mismatch and the dislocation energy a minimum [36]. The thickness which starts to generate dislocation called critical thickness ($h_c$). Matthew suggested that the critical thickness is the value which makes the elastic energy and the dislocation energy simply equal [37]. If the thickness of the deposited film exceeds the critical thickness, the residual stress energy generates additional dislocations with a spacing ($p$). The dislocation density is simply $p^{-2}$. Thus, this location density is calculated by film thickness and lattice misfits.

The energy ($U_d$) stored in an edge dislocation is

$$U_d = \int \frac{1}{2} \sum \sigma_{ij} \varepsilon_{ij} dV = \int \frac{1}{2} \sum b_i \sigma_{ij} n_j dl \approx \frac{Gb^2}{4\pi(1-\nu)} \ln\left(\frac{h}{r_0}\right) \tag{4-6}$$

where, $\sigma_{ij}$ and $\varepsilon_{ij}$ are the shear stress and shear strain respectively, $b$ is Burgers vector, $n_j$ is displacement vector, $\nu$ is Poisson's ratio, $G$ is the shear modulus, $h$ is the distance from free space, and $r_0$ is core radius of dislocation origin.

The strain energy ($U_h$) created by elastic strain field is

$$U_h = -b\sigma h = -2G\frac{1+\nu}{1-\nu} bhf \cos\lambda \tag{4-7}$$

where, $\lambda$ is angle between the force and slip direction.

The total energy of lattice mismatch then is

$$U_d + U_h = \frac{Gb^2}{4\pi(1-\nu)} \ln\left(\frac{h}{r_0}\right) - 2G\frac{1+\nu}{1-\nu} bhf \cos\lambda \tag{4-8}.$$

The critical thickness ($h_c$) is defined as the value for the minimum total energy condition. This criteria is simplified to Matthew's condition, $U_d = U_h$, then,

$$h_c = \frac{|b|}{8\pi f(1+\nu)\cos\lambda}\left\{\ln\left(\frac{h_c}{r_0}\right)+1\right\} \tag{4-9}$$

[38]. This form is similar to Matthew and Blakeslee's work when threading dislocations are generated at the interface by misfit [39]. The critical thickness is inversely proportional to the lattice misfit when, as is typically the case for small values of misfit, $h_c >> r_0$.

When the film thickness is thicker than critical thickness a residual stress remains and generates additional dislocations. If additional parallel dislocations are generated with a spacing ($p$),

$$\frac{|b|}{8\pi h(1+\nu)\cos\lambda}\left\{\ln\left(\frac{h}{r_0}\right)+1\right\} = f_m - \frac{b}{p} \tag{4-10}$$

where, the maximum strain ($f_m$) is

$$\frac{|b|}{8\pi h_c(1+\nu)\cos\lambda}\left\{\ln\left(\frac{h_c}{r_0}\right)+1\right\} = f_m \tag{4-11}$$

[40].

To calculate the critical thickness and dislocation spacing of (110) CIGS on (102) $MoSe_2$, we assume that the dislocations occur on the CIGS side of the interface. The Burgers vector (b) of CIGS is $\frac{1}{2}\langle 110\rangle$ since the crystal structure of CIGS is similar to the zincblende structure [41]. The core radius of a dislocation ($r_0$) is generally taken to be

$0.5\times|b|$ and Poisson's ratio of CIGS is 0.28 [42].With the parameters listed above, the theoretical dislocation spacing results of CIGS were not matched with experimental results of CIGS on GaAs films [43]. This is a common observation for a variety of materials. An empirical parameter is commonly used to improve the accuracy of the model [44]. In the case of CIGS, if we increase the Burgers vector (b) by a factor of 1.66, the theoretical dislocation spacing matches well with experiment results as shown in Figure 4.3. The lattice parameters of CIGS in this work were also well matched to experimental results.

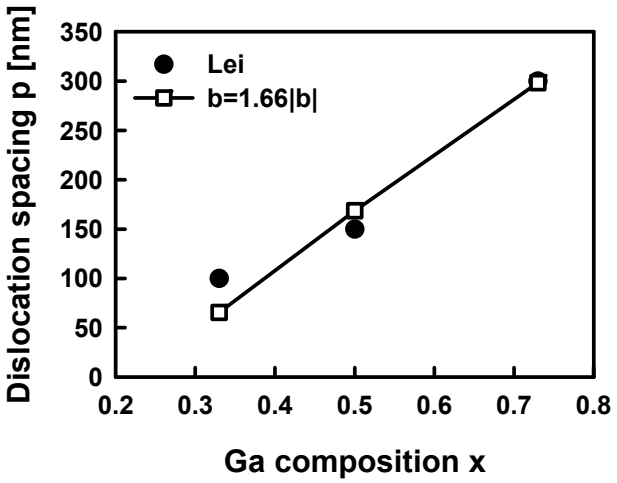


Figure 4.3. Empirical results and model of dislocation spacing of CIGS on GaAs [43].

Figure 4.4 shows the dislocation spacing of a 2.0 μm thick (110) CIGS film grown on (102) $MoSe_2$. To simplify the calculation, we assumed that dislocation spacing was affected by only one direction of lattice mismatch. The dislocation spacing of each

direction directly reflected the lattice misfits of each direction independently. In the direction of short spacing (a-direction), the dislocation spacing ($p_a$) were large near x=0.35 because of the low lattice mismatch. They decreased logarithmically outside of x=0.35. In the long spacing or c-direction, the dislocation spacing ($p_c$) decreased monotonically with increasing Ga composition.

The two dimensional (2D) dislocation densities are

$$N_{DIF} = \begin{cases} \dfrac{1}{p_a \times p_c} & (p_a \times p_c \neq 0) \\ \dfrac{1}{p_a + p_c} & (p_a \times p_c = 0) \end{cases} \quad [\text{cm}^{-2}] \qquad \begin{matrix} (4-12) \\ (4-13) \end{matrix}$$

[45].

The predicted 2D dislocation densities are shown in Figure 4.4. 2D dislocation densities had negative parabolic characteristics for x<0.35 because of the low lattice misfit in c- and a-directions near x=0 and x=0.35 respectively. The lowest density was $2.21\times10^{5}$ $\text{cm}^{-2}$ at x=0.35. Overall densities were lower than $9\times10^{9}$ $\text{cm}^{-2}$. However, 2D dislocation densities increased monotonically as increasing Ga composition for x>0.35 due to monotonic increases of misfit in both directions. The dislocation density rose to $1.83\times10^{11}$ $\text{cm}^{-2}$ at CGS.

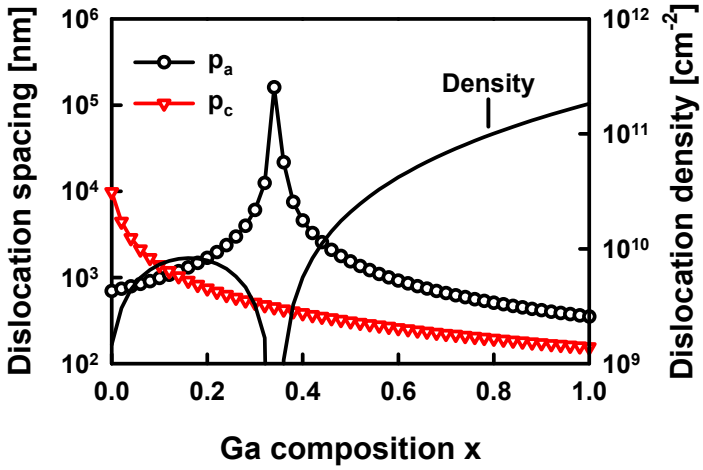


Figure 4.4. Dislocation spacing of each direction and two dimensional dislocation densities of (110) CIGS on (102) $MoSe_2$.

2D dislocation densities represent the dislocation densities at the CIGS/$MoSe_2$ interface. Theoretically, these densities directly affect the back contact performance but may not the bulk characteristics. However, about 44% of interface dislocations are typically found to be threading dislocations. Thus 2D dislocation densities can affect the bulk properties of CIGS [43].

Further investigating defect characteristics in misfit dislocations, dislocations along the [110] direction of the chalcopyrite structure are polar i.e. the dislocations are located in cation atomic planes (metals) or anion atomic planes (chalcogens). Dislocations in cation planes are preferred energetically over anion planes, thus vacancies and anti-sites of metal ions can be the preferred defects, specifically $V_{Cu}$, $V_{In}$, $In_{Cu}$, and $Cu_{In}$ [46,47]. $V_{Cu}$ are the major acceptor with a low activation energy ($E_a$) in CIGS. $In_{Cu}$ forms a defect cluster with $V_{Cu}$ in Cu deficient films, called an ordered defect cluster

(ODC: $2V_{Cu}^{-} + In_{Cu}^{2+}$,) by spontaneous reaction. Thus, $V_{In}$ and $Cu_{In}$ may be major deep traps in misfit dislocations. The activation energies of $V_{In}$ and $Cu_{In}$ are 0.17 eV and 0.29 eV above the valence band edge respectively [46].

Hanna et al. characterized the deep traps in CIGS films which were grown by single-stage and three-stage process as a function of Ga composition using thermal admittance spectroscopy [48]. The activation energies of dominant deep traps were near 0.3 eV above valence band edge through all compositions. Based on the activation energy, these traps are expected to be $Cu_{In}$. Trap densities were a minimum ($1.2\times10^{15}$ $cm^{-3}$) at x=0.26 in single stage process films while the minimum trap density of three-stage process films was $5.0\times10^{14}$ $cm^{-3}$, near half of single stage process results.

Figure 4.5 show the bulk trap densities due to misfit dislocation model. We assumed all interface dislocations are threading dislocations and the line defect densities along threading dislocation are uniform. The misfit dislocation models of the single stage process films closely matched the experimental results except near x=0. The defect densities along threading dislocations were $1\times10^{5}$ $cm^{-1}$ and $4\times10^{4}$ $cm^{-1}$ per threading line for single and three-stage process respectively. The difference between single and three stage process were only the defect densities per threading line. Since misfit dislocation models do not include grains and grain boundary effects, the model was very well matched experiments in large grain size region, i.e. near x=0.3 while the trap densities estimated by the misfit model were lower than the experimental results near x=0.0 and 1.0. It is also true that factors other than misfit may be leading to defects in these regimes.

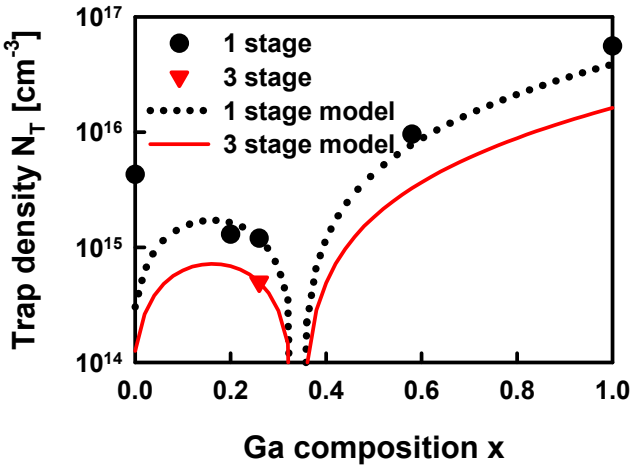


Figure 4.5. Experiment data and model of defect densities due Ga composition for two different CIGS deposition processes.

### 4.3. Heteroepitaxy between CdS and CIGS.

#### 4.3.1. Lattice mismatches.

A layer of n-type CdS is typically deposited on CIGS by chemical bath deposition (CBD) to form the pn-junction. Generally the crystal structures of CdS are hexagonal and cubic. While hexagonal CdS is the more stable crystal structure, both structures are observed at the CIGS interface. The crystal structure of CdS depends on the process conditions and the dominant orientation of CIGS [49]. The space groups and lattice constants of hexagonal and cubic CdS are $P6_3\,mc$, a=4.1348, c=6.7490 [50] and, $F\bar{4}3m$, a=5.811 [51], respectively. The orientations of hexagonal and cubic CdS that have a good lattice match to CIGS are hexagonal (001) CdS to (112) CIGS and cubic (100) CdS to (100) CIGS like CIGS and $MoSe_2$. The lattice misfits of hexagonal and cubic CdS structures to CIGS are shown in Figure 4.6. In both structures, the lattice misfit increased

linearly with increasing Ga composition from 1.04% and 1.55% with CIS to 4.00% and 4.53% with CGS. Hexagonal CdS is more stable than cubic CdS however cubic CdS is better matched with CIGS than hexagonal.

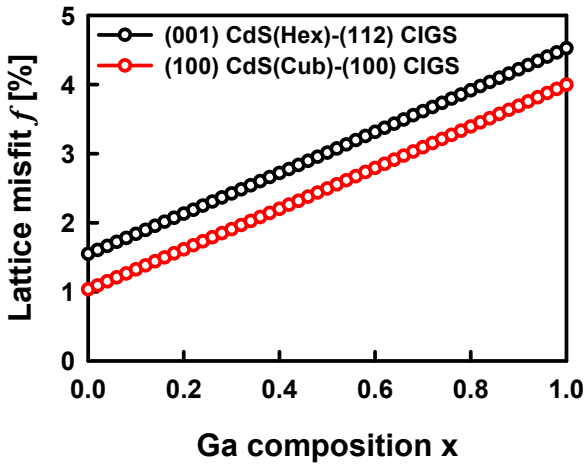


Figure 4.6. Misfits of hexagonal and cubic CdS to CIGS.

### 4.3.2. Dislocation spacing (*p*) and dislocation density.

Since cubic CdS had a lower misfit density, we examined it for high efficiency solar cells. Dislocation spacing and trap densities of 70 nm cubic CdS films on (100) CIGS are shown in Figure 4.7. The dislocation densities were $2.2\times10^{11}$ to $5.28\times10^{12}$ $cm^{-2}$ where the Poisson's ratio of CdS was taken as 0.39 [52] and the Burgers vector of cubic CdS is b = $\frac{1}{6}\langle 11\bar{2}\rangle$ [53]. Dislocation densities were simply calculated as $1/p^2$ because of symmetric misfits. Dislocations are located at the interface between CdS and CIGS.

Thus, 2D dislocation densities can be directly related to trap densities at the CdS/CIGS interface.

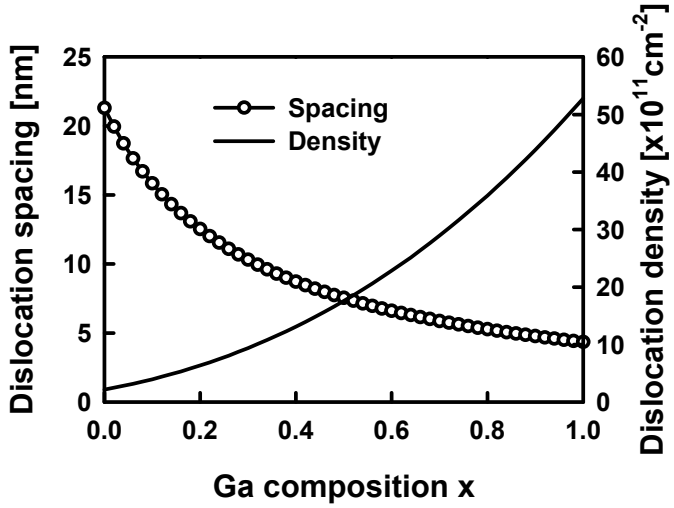


Figure 4.7. Dislocation spacing and dislocation densities of (100) cubic CdS–(100) CIGS.

CdS is an n-type material with a low carrier concentration. S vacancies ($V_S$) and Cd interstitial atoms ($I_{Cd}$) are the dominant donor-like defects. The characteristics of each trap is not well known but the activation energy of donor-like traps are 0.20 to 0.25 eV, 0.34 eV and 0.48 eV below conduction band edge [54,55]. Low activation energy traps ($E_a$) are assumed to be due to $V_S$ and $V_S$, which are the dominant defects in CdS [56].

**4.4. Device simulation.**

We investigated the effects of bulk and interface misfit traps models on CIGS solar cells performance using DESSIS, commercial multi physics numerical device

simulation tools. Device simulation is performed by self-consistently solving the current continuity equation and the Poisson equation. Shockley-Reed-Hall recombination model and Hurkx's trap assisted tunneling model were considered in recombination [57].

Additionally, a thermionic emission current model was used for interface recombination. In the thermionic emission mechanism, carriers which have statistically higher energy than the energy barrier can transport over the barrier. This mechanism can explain the hole injection from valence band of CIGS into the interface defect states.

Thermionic emission current should satisfy the current continuity through device so that currents in region 1 and 2 are same

$$J_2 = J_1 . \tag{4-14}$$

The current density ($J_2$) and energy flux density ($S_2$) in the high band energy region are

$$J_2 = q\left[ v_2 n_2 - \frac{m_2}{m_1} v_1 n_1 \exp\left( -\frac{\Delta E}{kT} \right) \right] \tag{4-15}$$

and,

$$S_2 = S_1 + \frac{J_2}{q}\Delta E = -\left[ v_2 n_2 kT_2 - \frac{m_2}{m_1} v_1 n_1 kT_1 \exp\left( -\frac{\Delta E}{kT} \right) \right] \tag{4-17}$$

respectively, where,

$$v_i = \sqrt{\frac{kT_i}{2\pi m_i}} , \tag{4-18}$$

$k$ and $T$ are Boltzmann constant and temperature respectively. $m_i$, $v_i$, $S_i$ and $J_i$ are effective mass, thermionic emission velocities, energy flux density and current density in each region respectively. $\Delta E$ is positive energy band difference between two regions.

Optical absorption and reflections in the multiple stacked layers are calculated by transfer matrix methods. When the waves in forward and backwards directions are *A* and *B* respectively, waves in each layer are

$$\begin{bmatrix} A_i \\ B_i \end{bmatrix} = \frac{1}{2n_1}\begin{bmatrix} n_1 + n_2 & n_1 - n_2 \\ n_1 - n_2 & n_1 + n_2 \end{bmatrix}\begin{bmatrix} A_{i+1} \\ B_{i+1} \end{bmatrix} \tag{4-19}$$

and light absorption (*G*) is

$$G(\lambda, z) = \phi_0(\lambda, z_0)\alpha(\lambda)\exp[-\alpha(\lambda)(z - z_0)] \tag{4-20}.$$

Model parameters and device structures are shown in Table 4.2. Electron affinities ($\chi$) and energy band gaps ($E_g$) of CIGS due to Ga composition (x) are

$$\chi = 3.97 + 0.6x \tag{4-21}$$

$$E_g = 1.01 + 0.53x + 0.13x^2 \tag{4-22}$$

[29].

We used the n-k values from Paulson's work [58] for the optical parameters of CIGS. The n-k values between compositions and wave lengths are extracted by interpolation with second order polynomial functions. Figure 4.8 (a) and (b) show the fitting and experimental results of n-k values of CIGS and (c) and (d) show surface plots of n-k values used in this work.

Table 4.2. Physical parameters and device structure for simulation.

| | | ZnO:Al | ZnO | CdS | CIGS | |
|---|---|---|---|---|---|---|
| | | | | | CIS | CGS |
| Parameters | Dielectric Constant | 7.8 | | 2.48 | 13.60 | 10.07 |
| | Band gap [eV] | 3.441 | | 2.48 | 1.01 | 1.68 |
| | Electron Affinity [eV] | 4.50 | | 4.24 | 4.57 | 3.97 |
| | Mobility [$cm^2/Vs$] | N: 45, P: 15 | | N: 45<br>P: 15 | N:100, P: 45 | |
| Structure | Dopant type & Concentration [$cm^{-3}$] | n-$1x10^{19}$ | n-$1x10^{17}$ | n-$1x10^{15}$ | p-$1x10^{16}$ | |
| | Thickness [μm] | 0.15 | 0.10 | 0.07 | 2.00 | |
| Traps | $E_T$ [eV] | | | $E_C$-0.21 | $E_V$+0.30 | |
| | σ [$cm^{-2}$] | | | $1\times10^{-14}$ | $1\times10^{-14}$ | |

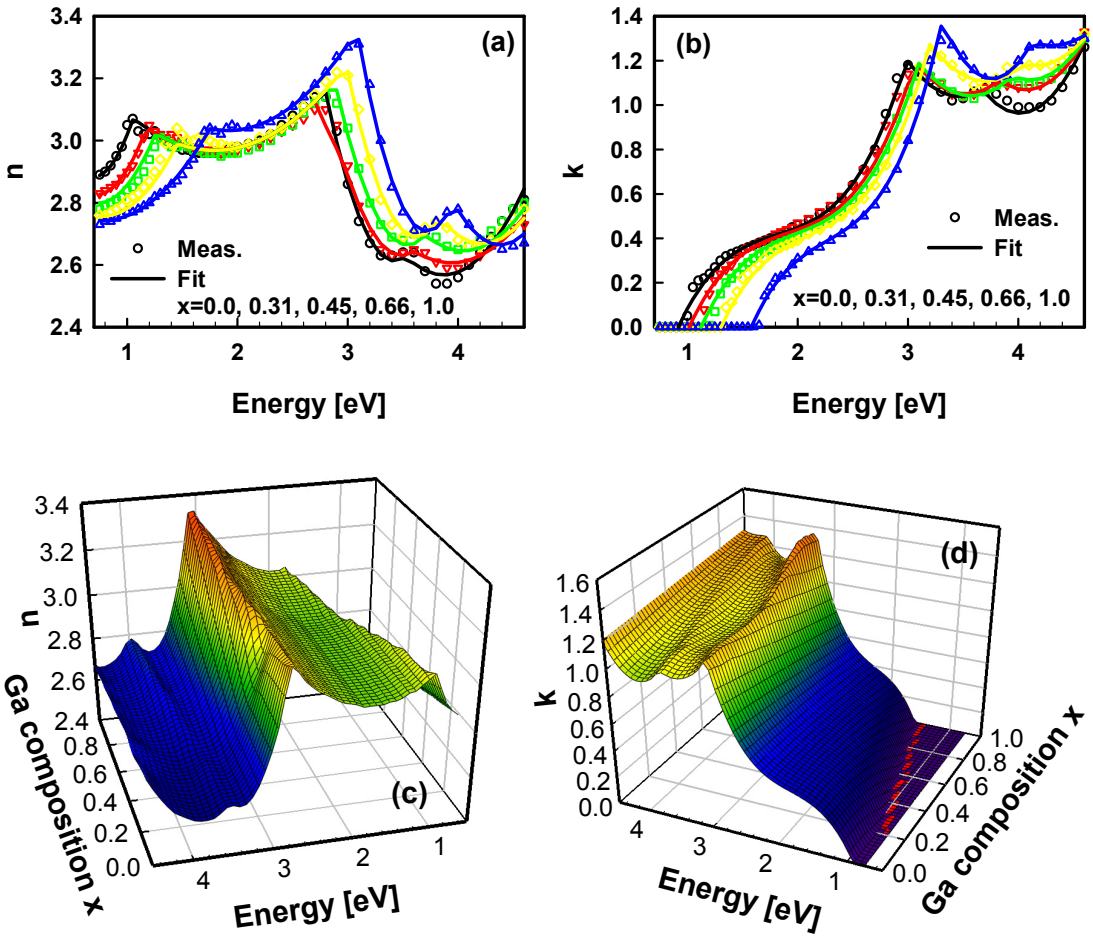


Figure 4.8. Fitting and experimental results of n (a) and k (b) values of CIGS and surface plots of n (c) and k (d) model of CIGS.

## 4.5. Result and discussion.

### 4.5.1. The bulk trap model of misfit of CIGS and $MoSe_2$

Figure 4.9 show the experimental and simulation results of a CIGS solar device. We compared our modeling results with the experimental work of Shafarman et al. [11], Eisenbarth et al, [8] and Contreras et al. [9] and also compared with 19.9% [59] and

20.3% [3] efficient CIGS solar cells. Shafarman et al. fabricated the CIGS solar cells with different Ga compositions 0.27 ~ 0.81 using a single stage co-evaporation process. Eisenbarth et al. deposited CIGS films by the three-stage co-evaporation process and also characterized traps in the CIGS films. Recently, Contreras et al. represented up-to-date results of wide band gap CIGS solar cells by high temperature three-stage process on EtaMax glass substrates.

In ideal CIGS solar cells with homogeneous composition, the maximum efficiency was 20.5 % at $E_g$=1.28 eV. The efficiencies of 1.20 to 1.45 eV band gaps devices were above 20% under AM 1.5 illumination. The efficiencies of CIS and CGS solar cells were 15.06% and 17.84% respectively. Open circuit voltages ($V_{OC}$) were linearally proportional to the energy band gap and Ga composition. The differences between band gap and $V_{OC}$ are 0.514 to 0.537 V through Ga composition.

In the single stage bulk misfit trap model, the maximum efficiency was 19.47% at the lowest trap densities composition of x=0.35 ($E_g$=1.21 eV). The efficiency decreased sharply away from x=0.35 and the efficiencies of CIS and CGS were 13.17% and 11.0% respectively. The short circuit current ($J_{SC}$) and fill factor (FF) decreased significantly from 18.42 mA/cm$^2$ and 84.8% to 14.18 mA/cm$^2$ and 73.1% in CGS. Comparing the single stage process results of Sharfarman et al., $J_{SC}$ and $V_{OC}$ are well matched and the errors were within 5%. However, the efficiencies were higher than experimental results because of fill factors. The differences in FF were especially large at CIS and CGS. These differences were due to high parasitic shunt resistance in the simulation which might be current flow at the grain boundaries. The misfit trap model does not include the

current mechanism at the grain boundaries, thus the FF was generally larger than experimental results.

The three-stage bulk trap model has half of the deep trap density compared to the single stage film. Thus, comparing the single stage process model, the efficiencies increased 1.25% on average except near x=0.35 and the efficiency of CGS increased to 12.65%. The reduced trap density increased $J_{SC}$ by 11.08%. The $J_{SC}$ of CGS was 15.75 $mA/cm^2$ in the three stage bulk trap model. Comparing the model results to the work of Eisenbarth et al., $J_{SC}$ results were well matched and $V_{OC}$ were well matched below 1.36 eV. However, $V_{OC}$ was proportional to the band gaps above 1.36 eV and was 1.08 V at CGS, while $V_{OC}$ saturated between 0.71 and 0.73 V in experimental results. The difference in FF reduced compared to the single stage growth because grain sizes in three-stage process were larger. Thus grain boundary effects might be reduced.

In the three-stage process, the Ga composition is non uniform through CIGS layer because of the difference in the diffusivity of In and Ga [60]. Compositional back grading improves the performance by increasing the collection of electrons and holes in the neutral region [61, 62]. The effect of Ga grading with misfit trap densities were investigated using our previous methods [63]. The absorber layer was divided into twenty five 80 nm thick layers for optical absorption calculation to take into account the gradient in the Ga composition. The trap density in each layer was determined by average Ga composition in that layer. We considered linear backward grading for Ga compositions below 0.7. The composition at the bottom was fixed at x=0.7. With Ga backward grading similar to that observed in the three-stage process, the maximum efficiency increased to

21.24% at x=0.35 since $V_{OC}$ increased significantly from 0.69 V to 0.734 V due to the increase of band gap near the end of the depletion region. $J_{SC}$ also increased from 34.8 mA/cm$^2$ to 35.83 mA/cm$^2$ due to the improvement in the charge collection efficiency in the neutral region. When the Ga composition is 0.3, the efficiency was increased the most, from 18.47% to 21.02%. It was due to multiple effects including more light absorption with low band gap at the top, $V_{OC}$ increase due to the wide band gap at the edge of the depletion region, and low loss because of low trap density composition. These results were very well matched with the experimental results of 20.3% cells. The errors are less than 3% on average. $J_{SC}$ was slightly higher than experimental results of 20.3% cells. In the work of Jackson et al. cells with an efficiency above 20% were obtained in the rage of x=0.30 ~ 0.35. Simulation results shows that the efficiencies are higher that 21% in x=0.30 ~ 0.35 and decreased for compositions outside of that range due to high trap densities.

Simulation results of the bulk misfit trap model reproduced efficiency trend on Ga composition were very well and showed a good match with experimental results. The maximum efficiency was always achieved at compositions with a low misfit density. Efficiencies decreased sharply for compositions significantly different than x=0.35. Comparing CIS and CGS, the misfit of CGS is much higher. Thus efficiency is lower than CIS. The reason for the existence of a maximum in efficiency as a function of Ga composition, and low efficiency at wide band gap may be due to the low misfit between CIGS and $MoSe_2$. Thus, the effects of bulk traps due to misfit between CIGS and $MoSe_2$ along with band gap grading models provide a good explanation for the observed CIGS

solar cells performance dependence on Ga composition. However, misfit model did not explain the open circuit voltage saturation at Ga-rich films as shown in Figure 4.9.

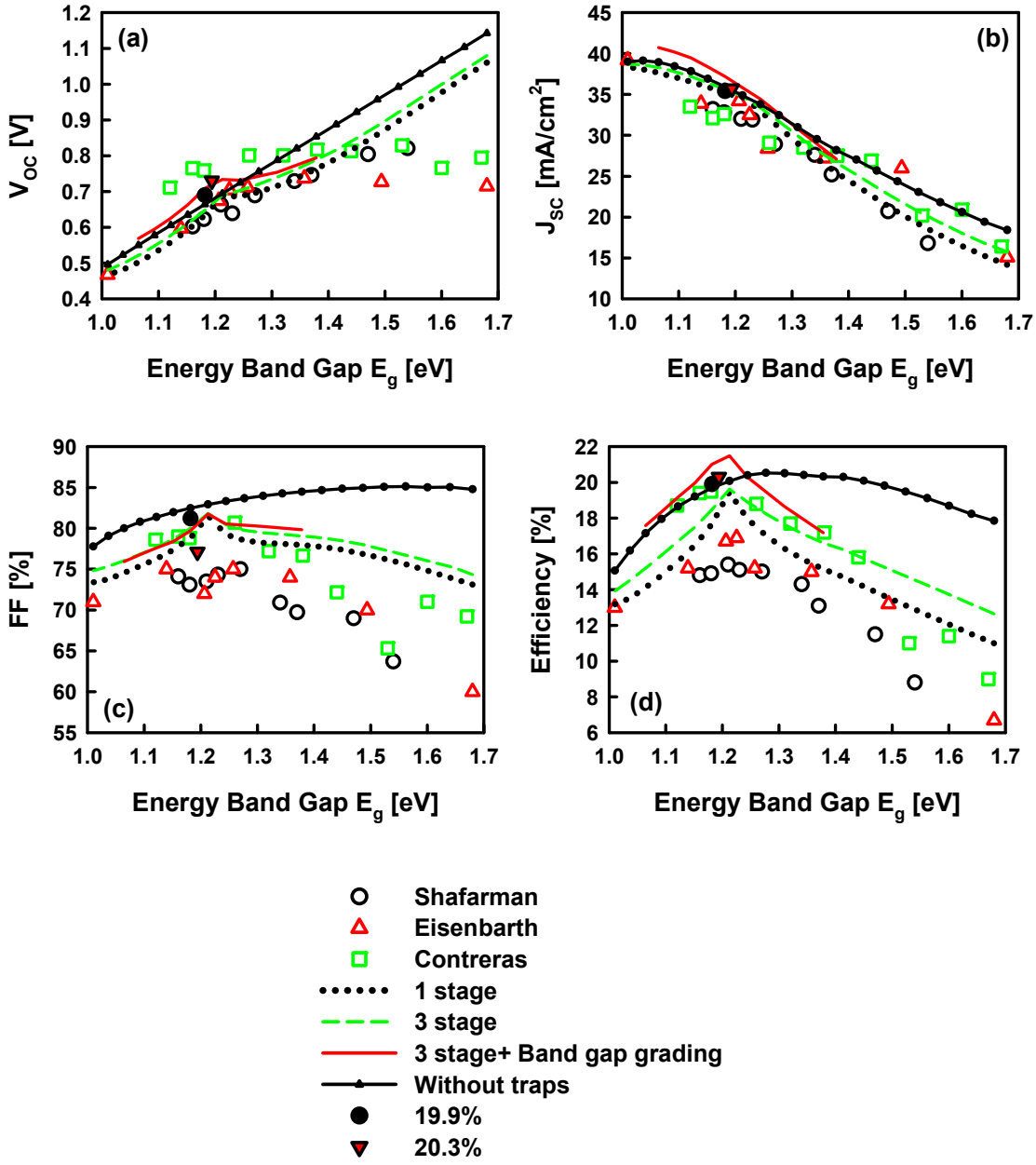

Figure 4.9. Comparison of experimental and simulation results of single stage, three-stage and three-stage with linear Ga compositional grading bulk trap density models by misfits. (a) open circuit voltage $V_{OC}$, (b) short circuit current ($J_{SC}$), fill factor (FF) and, (d) efficiency.

### 4.5.2 Thermionic emission and interface trap model by the misfit between CdS and CIGS.

The band alignment between traps at the CdS/CIGS interface is important because it determines the activation of interface traps in thermionic emission mechanism. The electron affinity of CdS is 4.24 eV. The activation energy of the S vacancy ($V_S$) which is a commonly observed interface dislocation trap is 0.21 eV below the conduction band edge of CdS. For comparison, the dependence of the electron affinity of CIGS on Ga concentration is given by equation (4-21).

Figure 4.10 shows the band gaps and the energy differences between interface traps and the valence band edge of CIGS as a function of Ga composition. Below x=0.2 ($E_g$=1.12 eV), the interface traps are above the conduction band edge of CIGS. Thus the interface states are almost empty and cannot affect the carrier transport. Above x=0.2, the energy of the interface trap is located in the band gap of CIGS. Thus interface traps can affect the solar cell performance. The energy difference between the energy level of interface traps and the valence band edge of CIGS are constant value around 1.15 eV. Contreras et al. extracted the activation energies of dark currents as a function of Ga composition by measuring the temperature (T) – $V_{OC}$ relationship [9]. If the dark current

mechanism is drift-diffusion, the activation energy should be the band gap of the absorber material. However, the activation energies were found to be constant at 1.16 to 1.2 eV for x > 0.3 (Eg=1.18) as shown in Figure 4.10. This means that the dark current mechanism is not drift-diffusion but instead has a logarithmic dependency on temperature and the activation energy. When one compares the energy difference between the interface traps and valence band edge of CIGS, however, the extracted activation energies are well matched.

Regarding interface traps, many previous researches considered that minority traps in the CIGS layer contributed the interface traps [64,65]. However, activation energies of deep traps in CIGS have a similar energy difference from each band edge though the whole Ga composition [66,67]. Thus, minority (donor likes) traps are deactivated in wide band gap CIGS solar cells because conduction band edge of CIGS is higher than CdS in high Ga composition. However, minority carrier traps were detected in wide band gap CIGS solar cells with 50 ~ 260 meV activation energy [68]. This cannot be explained by minority carrier traps in CIGS. However, interface traps in the CdS layer explain this effect very well.

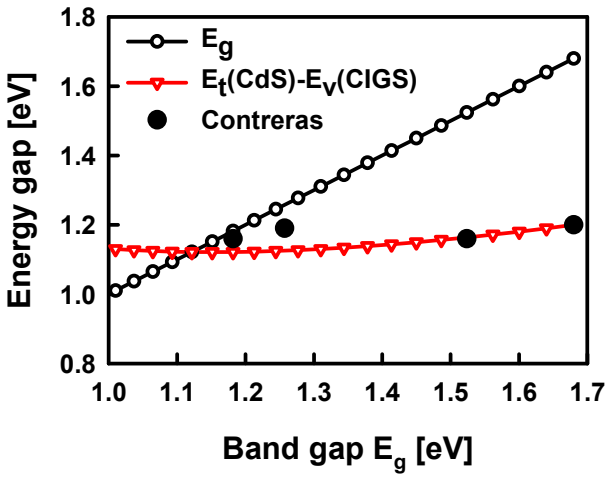


Figure 4.10. The behavior of band gap, energy difference between interface trap energy of CdS and valence band edges of CIGS by Ga composition.

In such a structure the dark current is related to the carrier transport to interface traps and the hole transport from the valence band of CIGS into interface trap states. There are several possible mechanisms for this transport. However, since the depletion region is wide, the built in electric field is low, as a result, direct or trap assisted tunneling currents are very unlikely. Thermionic emission is one of the possible dark current mechanisms. In the thermionic emission mechanism, energy difference between the interface traps and valence band edge of CIGS becomes an energy barrier like Schottky barrier. This energy barrier is determined by the Fermi energy level and the energy difference between the interface traps and the valence band edge at the interface. The total dark current then is the sum of the drift-diffusion and thermionic emission currents. The dark currents of CIGS solar cells above x=0.2 are limited by thermionic emission current at the junction interface because of the low activation energy.

Hole injection current is determined by the energy barrier at the interface and the states of interface traps. For example, if the interface states are all empty, it is impossible that holes inject into interface states. The interface trap density affects the band bending and status of interface traps at the junction interface.

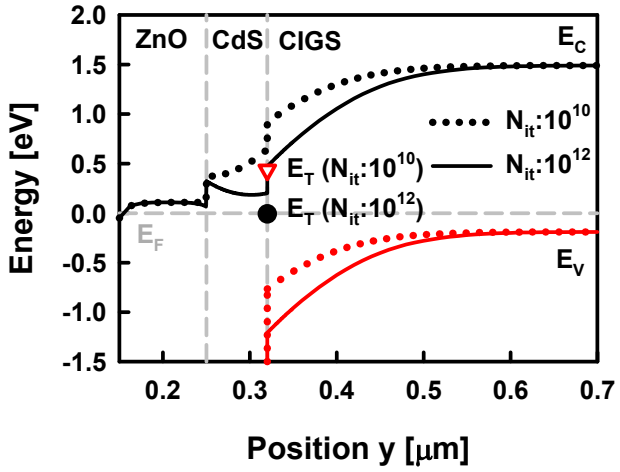


Figure 4.11. Band diagrams of CGS near the between CdS and CIGS when the interface traps densities are $10^{10}$ and $10^{12}$ $cm^{-2}$ respectively.

Figure 4.11 show the band diagrams of CGS solar cells for two interface trap densities near junction interface. When the interface trap densities are $10^{10}$ $cm^{-2}$ and $10^{12}$ $cm^{-2}$, the energy levels of interface traps are 0.435 eV and 8 meV above Fermi level respectively. At a density of $10^{10}$ $cm^{-2}$, the interface traps are almost totally empty. And, at a density of $10^{12}$ $cm^{-2}$, however, half of the interface traps are filled. Thus thermionic emission is unlikely to occur for low trap concentrations. For high trap concentration, the Fermi level is pinned at the energy level of interface traps at the junction interface. Since

the carrier concentrations of CdS and CIGS are generally in the range of $10^{15}$ to $10^{16}$ $cm^{-3}$, energy band bending at the interface is easily affected, even by low interface trap densities.

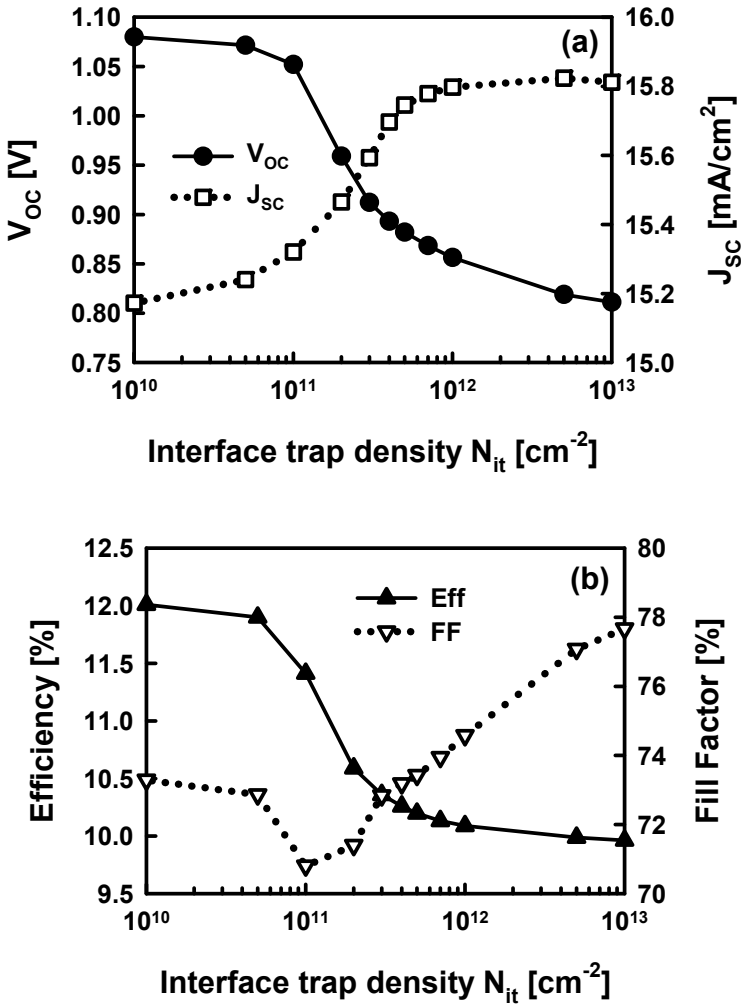


Figure 4.12. Performance degradations of $CuGaSe_2$ solar cell due to interface trap densities. (a) open circuit voltage ($V_{OC}$) and short circuit current ($J_{SC}$) and, (b) efficiency and fill factor.

Figure 4.12 show the effects of interface trap densities on CGS solar cell performance, now applying the thermionic emission mechanism. When the interface trap densities are higher than $10^{11}$ $cm^{-2}$, $V_{OC}$ decreased sharply and saturated at 0.8 V due to the thermionic emission current while $J_{SC}$ was increased by band bending. Interface traps work as the donor like traps in CdS. Thus high trap concentrations increase band bending and depletion width in CIGS layer. The efficiency of CGS decreases from 12% to 9.96%. The dominant current mechanism was changed from Shockley Read Hall recombination to thermionic emission. This increases the fill factor for defect densities above $10^{11}$ $cm^{-2}$. Considering the energy difference between interface traps and the valence band edge of CIGS, thermionic emission transport can happen above x=0.2 (Eg=1.12 eV). Since interface trap densities in the misfit model are in the range of $2.2\times10^{11}$ to $5.3\times10^{12}$ $cm^{-2}$, the Fermi level at the interface is pinned for Ga concentrations above 0.3 (Eg =1.19 eV), because of interface trap densities above $1\times10^{12}$ $cm^{-2}$. Applying both the bulk and interface misfit trap models, the simulation and experimental results of CIGS solar cells are shown in Figure 4.13. $V_{OC}$ was linearly proportional to the band gap below x=0.35 (Eg=1.22 eV) however, correlation slope was changed from 1.0 to 0.29 above x=0.35. $V_{OC}$ saturated at 0.85 V. Thermionic emission currents were dominant over drift-diffusion and recombination currents above x=0.55 ($E_g$=1.34 eV). Thus $V_{OC}$ is determined by energy barrier at the junction interface. The $V_{OC}$ result was very well matches with the works of Shafarman et al. and Eisenbarth et al. through all compositions.

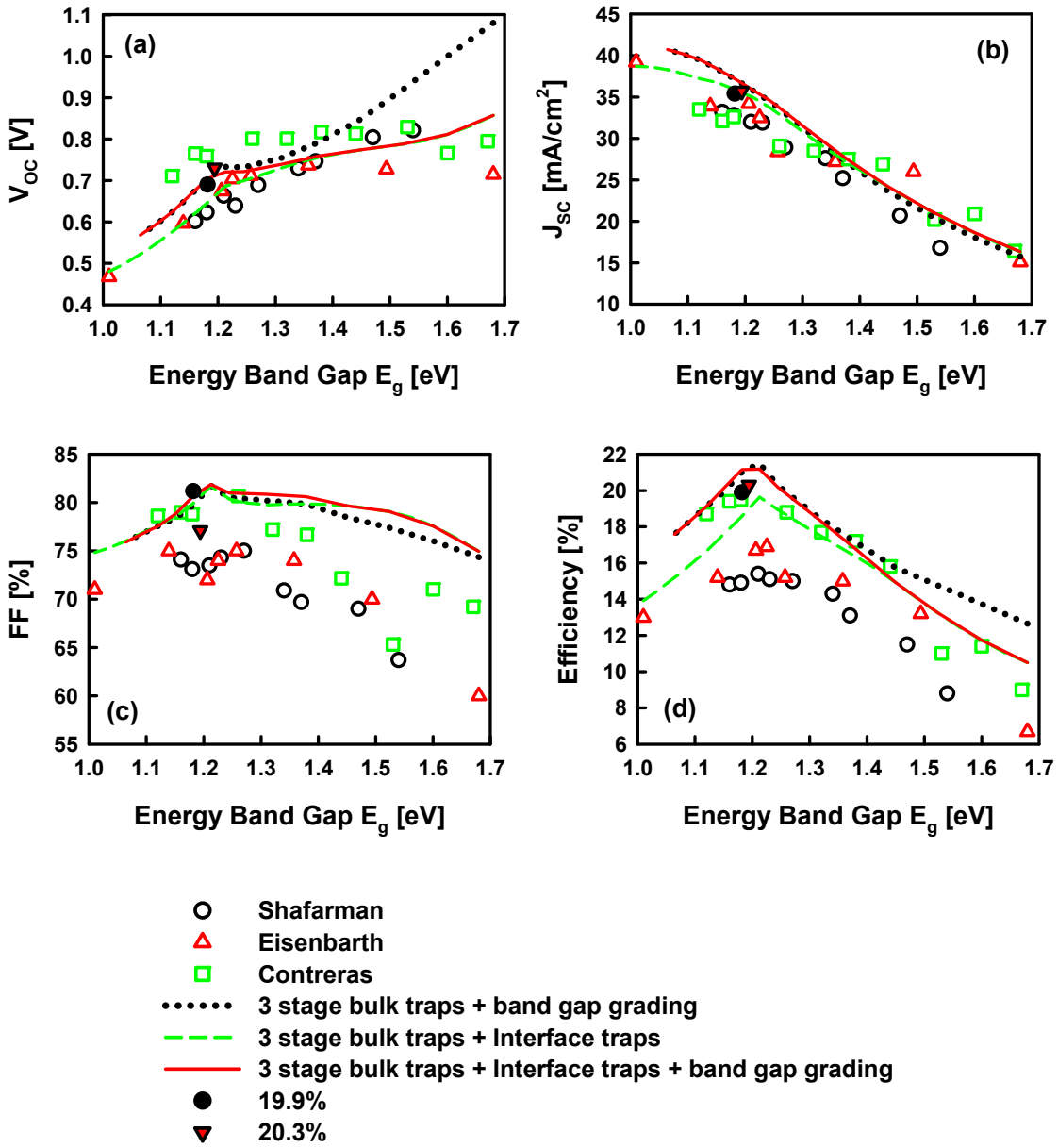


Figure 4.13. Comparison of experimental and simulation results of three-stage, linear Ga compositional grading and interface trap models by misfit (a) open circuit voltage $V_{OC}$, (b) short circuit current ($J_{SC}$),fill factor (FF) and, (d) efficiency.

Comparing to the work of Contreras et al., the trends of $V_{OC}$ are matched even though simulation results were lower by 50 to 100 mV. This difference may be due to large forward compositional grading [62]. Forward grading increases $V_{OC}$ by increasing the band gap at the CdS/CIGS interface however $J_{SC}$ can be lost [63]. Thus $J_{SC}$ was lower than other works below x=0.55 (Eg=1.34 eV). Fill factors were close and efficiencies were well matched with experimental results of Contreras et al. The interface misfit trap and thermionic emission model accurately explain the $V_{OC}$ saturation effects.

**4.6. Conclusions.**

A misfit model between the layers in a CIGS solar cell can explain the general dependence of the behavior of these devices with Ga composition. Low misfit films can be grown with a low dislocation density. High efficiency (220/204) CIGS are well lattice matched with r-plane (102) $MoSe_2$. Lattice misfit between CIGS and $MoSe_2$ generates threading dislocations correlated with lattice misfit in CIGS.These threading dislocations contribute to bulk traps densities. The best performance cells were obtained near a Ga concentration of x=0.35. This correlates perfectly with the minimum in misfit, and therefore misfit dislocations. Wide band gap devices had low efficiencies due to a high density of dislocations caused by a large misfit. By controlling the trap density due to threading dislocations, performance can be improved.

Misfit between CIGS and CdS generates interface trap states in CdS layer. Since both layers have a low carrier concentration, the Fermi level is easily pinned at the energy level of interface traps at the junction interface, even for moderately low interface trap

densities. It is pinned above x=0.55 in our model. Fermi level pinning activates the interface traps and enables thermionic emission transport of holes from the valence band of CIGS to the interface traps. Fermi level pinning and the thermionic emission mechanism leads to a saturation of the open circuit voltage in wide band gap CIGS solar cells.

We present new misfit trap models. These models well explain general characteristic of CIGS solar cells. It is important to consider heteroepitaxy between layers for high performance and high efficiency in heterojunction solar cells. Low misfit is preferred to achieve high efficiency solar cells.

**References**


[1] K. L. Chopra, P. D. Paulson, V. Dutta, Prog. Photovolt.: Res. Appl. 12 (2004) 69–92.

[2] U. Rau, H.W. Schock, Appl. Phys. A 69 (1999) 131–147.

[3] P. Jackson, D. Hariskos, E. Lotter, S. Paetel, R. Wuerz, R. Menner, W. Wischmann, M. Powalla, Prog. Photovolt.: Res. Appl. 19 (2011) 894–897.

[4] W. Shockley, H. J, Queisser, J. Appl. Phys. 32 (1961) 510-519.

[5] A. Martí, G. L. Araújo, Sol. Energy Mater. Sol. Cells 43 (1996) 203-222.

[6] W.N. Shafarman, R. Klenk, B.E. McCandless, 25th IEEE Photovolt. Spec. Conf., May, 1996; Washington, D.C. 783.

[7] M. A. Contreras, K. Ramanathan, J. AbuShama, F. Hasoon, D. L. Young, B. Egaas, R. Noufi, Prog. Photovolt.: Res. Appl. 13 (2005) 209–216.

[8] T. Eisenbarth, T. Unold, R. Caballero, C.A. Kaufmann, D. Abou-Ras, H.-W. Schock, Thin Solid Films 517 (2009) 2244–2247.

[9] M. A. Contreras, L. M. Mansfield, B. Egaas, J. Li, M. Romero, R. Noufi, E. Rudiger-Voigt, W. Mannstadt, Prog. Photovolt.: Res. Appl. 20 (2012) 843–850.

[10] R. Herberholz, V. Nadenau, U. Rühle, C. Köble, H.W. Schock, B. Dimmler, Sol. Energy Mater. Sol. Cells 49 (1997) 227-237.

[11] W. N. Shafarman, R. Klenk, B. E. McCandless, J. Appl. Phys. 79 (1996) 7324-7328.

[12] M. Gloeckler, J. R. Sites, Thin Solid Films 480–481 (2005) 241– 245.

[13] V. Nadenau, U. Rau, A. Jasenek, H. W. Schock, J. Appl. Phys. 87 (2000) 584-593.

[14] R. Caballero, S. Siebentritt, K. Sakurai, C. A. Kaufmann, H. W. Schock, M. Ch. Lux-Steiner, Thin Solid Films, 515 (2007) 5862–5866.

[15] M. A. Contreras, M. Romero, D. Young, Conference Record, 3rd World Conference on Photovoltaic Energy Conversion, Osaka, May 2003, 2864.

[16] S. Chaisitsak, A. Yamada, M. Konagai, Jpn. J. Appl. Phys. 41 (2002) 507.

[17] S. Marsillac, S. Don, R. Rocheleau, E. Miller, Sol. Energy Mater. Sol. Cells 82 (2004) 45.

[18] U. Rau, K. Taretto, S. Siebentritt, Appl. Phys. A 96 (2009) 221–234.

[19] C.-S. Jiang, M. A. Contreras, I. Repins, H. R. Moutinho, Y. Yan, M. J. Romero, L. M. Mansfield, R. Noufi, M. M. Al-Jassim, Appl. Phys. Lett. 101 (2012) 033903.

[20] D. H. Shin, Y. M. Shin, J. H. Kim, B. T. Ahn, K. H. Yoon, J. Electrochem. Soc., 159 (2012) B1-B5.

[21] P. E. Russell, O. Jamjoum, R. K. Ahrenkiel, L. L. Kazmerski, R. A. Mickelsen, W. S. Chen, Appl. Phys. Lett., 40 (1982) 995-997.

[22] T. Wada, N. Kohara, T. Negami, M. Nishitani, Jpn. J. Appl. Phys. 35 (1996) L1253.

[23] S. Nishiwaki, N. Kohara, T. Negami, T. Wada, Jpn. J. Appl. Phys. 37 (1998) L71.

[24] R. J. Matson, O. Jamjoum, A.D. Buonaquisti, P. E. Russell, L. L. Kazmerski, P. Sheldon, R. K. Ahrenkiel, Solar Cells, 11 (1984) 301-305.

[25] K. Orgassa, H.W. Schock, J.H. Werner, Thin Solid Films 431-432 (2003) 387–391.

[26] M. A. Contreras, B. Egaas, D. King, A. Swartzlander, T. Dullweber, Thin Solid Films 361-362 (2000) 167-171.

[27] A. M. Gabor, J. R. Tuttle, D. S. Albin, M. A. Contreras, R. Noufi, A. M. Hermann, Appl. Phys. Lett. 65 (1994), 198-200.

[28] S. H. El-Mahalawy, B. L. Evans, J. Appl. Cryst., 9 (1976), 403-406.

[29] S. R. Kodigala, Thin films and nanostructures $Cu(In_{1-x}Ga_x)Se_2$ based thin film solar cells Vol. 35, (2010).

[30] R. Chakrabarti, B. Maiti, S. Chaudhuri, A.K. Pal, Sol. Energy Mater. Sol. Cells, 43 (1996), 237-247.

[31] M. Souilah, A. Lafond, C. Guillot-Deudon, S. Harel, M. Evain, J. Solid State Chem., 183 (2010) 2274–2280.

[32] H.-G. Brühl, H. Neumann, G. Kühn, Solid State Commun. 34 (1980) 225-227.

[33] A. Luque. Handbook of Photovoltaic Science and Engineering, John Wiley & Sons, West Sussex, 2003.

[34] K. Wang, R. R. Reeber, Mat. Sci. Eng. R23 (1998) 101-137.

[35] A. Tonejc, S. Popovic, B. Grzeta-Plenkovic, J. Appl. Crystallogr. 13 (1980) 24.

[36] J. H. Van Der Merwe, J. Appl. Phys. 34 (1963) 117-122.

[37] J. W. Matthews, J. Vac. Sci. Technol., 12 (1975) 126-133.

[38] L. B. Freund, Mater. Res. Soc. Bull. 17 (1992) 52.

[39] J. W. Matthews, A. E. Blakeslee, J. Cryst. Growth, 27 (1974) 118-125.

[40] L. B. Freund, S. Suresh, Thin Film Materials Stress, Defect Formation and Surface Evolution, Cambridge University Press, New York, 2003.

[41] J. Dietrich, D. Abou-Ras, T. Rissom, T. Unold, H.-W. Schock, C. Boit, IEEE J. Photovolt., 2 (2012) 364-370.

[42] B. Fernandez, S. M. Wasim, Phys. Stat. Sol. (a), 122 (1990) 235–242.

[43] C. H. Lei, A. A. Rockett, I. M. Robertson, N. Papathanasiou, S. Siebentritt, J. Appl. Phys., 100 (2006) 114915.

[44] R. People, J. C. Bean, Appl. Phys. Lett. 49 (1986), 229.

[45] M. A. Meyers, H. Jarmakani, E. M. Bringa, B. A. Remington. Dislocations in Solids, vol. 15, (2009) chap. 89.

[46] S. B. Zhang, S.-H. Wei, A. Zunger, Phys. Rev. B, 57 (1998) 9642-9656.

[47] S. Lany, A. Zunger, J. Appl. Phys. 100 (2006) 113725.

[48] G. Hanna, A. Jasenek, U. Rau, H.W. Schock, Thin Solid Films, 387 (2001) 71-73.

[49] D. Abou-Ras, G. Kostorz, A. Romeo, D. Rudmann, A.N. Tiwari, Thin Solid Films 480–481 (2005) 118– 123.

[50] O. Madelung, Semiconductors: Data handbook 3rd ed., Springer, Berlin, 2004.

[51] R. W. G. Wyckoff, Crystal Structures, John Wiley and Sons, New York, 1963.

[52] R. M. White, IEEE Trans. Electron Devices, 14 (1967) 181-189.

[53] V. Nadenau, D. Hariskos, H.-W. Schock, M. Krejci, F.-J. Haug, A. N. Tiwari, H. Zogg, G. Kostorz, J. Appl. Phys., 85 (1999) 534-542.

[54] C. Grill, G. Bastide, G. Sagnes, M. Rouzeyre, J. Appl. Phys., 50 (1979) 1375-1380.

[55] M. Hussein, G. Lleti, G. Sagnes, G. Bastide, M. Rouzeyre, J. Appl. Phys., 52 (1981) 261-268.

[56] J. Oualid, J. L. Granier, D. Sarti, J. Phys. C: Solid State Phys. 12 (1979) 5323-5331.

[57] G. A. M. Hurkx, D. B. M. Klaassen, M. P. G. Knuvers, IEEE Trans. Electron Devices, 39 (1992) 331-338.

[58] P. D. Paulson, R. W. Birkmire, W. N. Shafarmana J. Appl. Phys., 94 (2003) 879-888.

[59] I. Repins, M. A. Contreras, B. Egaas, C. DeHart, J. Scharf, C. L. Perkins, B. To, R. Noufi, Prog. Photovolt: Res. Appl.16 (2008) 235–23.

[60] S. M. Schleussner, T. Törndahl, M. Linnarsson, U. Zimmermann, T. Wätjen, M. Edoff, Prog. Photovolt: Res. Appl. 20 (2012) 284–293.

[61] T. Dullweber, O. Lundberg, J. Malmström, M. Bodegård, L. Stolt, U. Rau, H.W. Schock, J. H. Werner, Thin Solid Films 387 (2001) 11-13.

[62] M. A. Contreras, L. M. Mansfield, B. Egaas, J. Li, M. Romero, R. Noufi, E. Rudiger-Voigt, W. Mannstadt, Conference Record, 37th IEEE Photovolt. Spec. Conf., Seattle, June 2011; 000026 – 000031.

[63] S. H. Song, K. Nagaich, E. S. Aydil, R. Feist, R. Haley, S. A. Campbell, Conference Record, 35th IEEE Photovol. Spec. Conf., Honolulu, June 2010; 002488 - 002492.

[64] R. Herberholz, M. Igalson, H. W. Schock, J. Appl. Phys., 83 (1998) 318-325.

[65] M. Igalson, A. Urbaniak, M. Edoff, Thin Solid Films 517 (2009) 2153–2157.

[66] M. Turcu, I. M. Kötschau, U. Rau, J. Appl. Phys., 91 (2002) 1391-1399.

[67] A. Zunger, S. B. Zhang, S.-H. Wei, Conference Record, 26th IEEE Photovolt. Spec. Conf., Anaheim, June 1997; 313-318.

[68] V. Mertens, J, Parisi, J. Appl. Phys., 101 (2007) 104507.

# Chapter 5

## Broken Band Gap Heterojunction for Tandem Copper Indium Gallium Diselenide Solar Cells

### 5.1. Introduction.

The efficiencies of single-junction solar cell are constrained by the Shockley-Queisser limit [1]. Further improvements require the use of multi-junction photovoltaic (PV) device architectures [2]. Crystalline multi-junction solar cells hold the world record efficiency [3], however, they are expensive to produce due to the need for epitaxial growth in ultra high vacuum [4]. It would be desirable to make multi-junction solar cells based on low-cost thin polycrystalline films such as CdTe and $CuIn_{1-x}Ga_xSe_2$ (CIGS).

In multi-junction PV devices two or more solar cells are stacked vertically and share the solar spectrum. Part of the solar spectrum is absorbed in top cell and the other part is absorbed in bottom cell and they connect electrically to each other. Thus, contacts between cells should be transparent below band gap of top solar cell. When two solar cells are stacked monolithically, it is inevitable to form a reverse biased p-n junction at the interface between them. This drops a large part of the voltage produced in the junctions and limits current flow. Typically, tunnel junction (TJ) diodes are used between the solar cells to solve this problem.

Tunnel junction formation is one of the obstacles in making multi-junction solar cells based on polycrystalline films. A conventional TJ requires a very heavily doped p-n junction with steep dopant profiles at the interface for good tunneling efficiency [5]. There are several difficulties in making tunnel junction with polycrystalline films. First, unlike in epitaxially grown single crystal films, the steep dopant profile is much more difficult to achieve in polycrystalline films owing to fast grain boundary diffusion [6,7]. Furthermore, some of the top cell layers require a high temperature deposition process to produce large grains good quality films with low trap densities. Thus, significant dopant diffusion in the bottom solar cell and inter-diffusion near the tunnel junction can occur. Second, doping in most polycrystalline PV materials such as CIGS occurs via vacancies or anti-site defects, which makes precise dopant control very difficult and compensation common. Third, it is impossible to form heavily doped layers of both types in single materials due to compensation effects [8,9]. To avoid these difficulties, multi terminal methods have been demonstrated [10,11]. In CIGS solar cells, $MoSe_2$ on ZnO:Al (AZO), SnO:F (FTO) and $In_2O_3$:Sn (ITO) make good ohmic contacts to a CIGS absorber, however low transmittance is a problem [12-14]. More fundamentally, however, it is difficult to imagine a scenario where creating a tandem device by stacking single-junction structures will yield a lower cost per watt of delivered power since one loses the advantages of monolithic integration.

In this chapter, we examine the possibility of using metal-oxide broken-gap heterojunctions as the tunnel junction in multi-junction CIGS solar cells. We investigated the I-V characteristics of p-$Cu_2O$/n-$In_2O_3$ junction which is expected to have a broken-

gap band alignment. We studied the effects of doping concentration and band alignment using numerical device simulation. We also investigated monolithic CIGS-based tandem PV device with p-$Cu_2O$/n-$In_2O_3$ junction where the top and bottom cell absorbers were $CuGaSe_2$ (CGS) and $CuInSe_2$ (CIS) respectively, including the band alignment of broken-gap heterojunctions with top and bottom solar cells.

## 5.2. Broken-gap heterojunction and metal oxide.

### 5.2.1 Broken gap heterojunction and its I-V characteristics.

A broken-gap heterojunction is a junction between two dissimilar materials where the conduction band edge of the n-type material is equal to or lower in energy than the valence band edge of the p-type material as shown in Figure 5.1 (a). Electrons can easily move across the junction interface with this band alignment by a nonlocal interband transition. As a result, the junction can has linear current-voltage (I-V) characteristics [15] even without heavy doping on both sides.

The electrical characteristics of the broken-gap heterojunction have been studied extensively in GaSb-InAs systems [15-22]. The valence band edge of GaSb is 0.48 to 0.53 eV higher than that of InAs and the band overlap ($\Delta\chi$ as shown in Figure 5.1 (a)) is 0.12 to 0.17 eV since the band gaps of InAs and of GaSb are 0.36 eV and 0.71 eV, respectively [16].

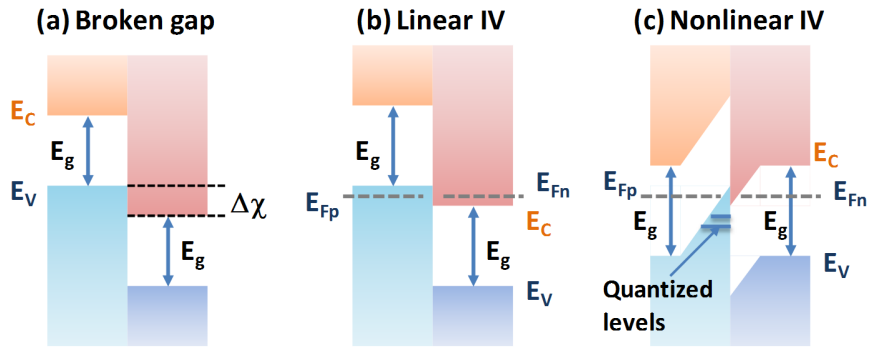


Figure 5.1. (a) Band alignment of broken-gap heterojunctions, (b) band diagram of linear I-V broken-gap heterojunction and (c) band diagram for nonlinear I-V broken-gap heterojunction.

The I-V characteristics of a broken gap junction are impacted by energy band bending at the junction interface [17,18]. Since the difference of electron affinities of two materials are higher than the band gap of high electron affinity materials, the Fermi level is located inside the bands; specifically, the conduction band of the low electron affinity material region and the valence band of the high electron affinity material region. This occurs near the junction interface to maintain the difference of the electron affinities of the two materials. Thus, carriers are accumulated near the junction interface, electrons in the low electron affinity material and holes in the high electron affinity material.

Linear I-V characteristics are observed when a p-n junction is formed from an n-type low electron affinity material and a p-type high electron affinity material as shown in Figure 5.1 (b) such as p-GaInAsSb/n-InAs and p-GaSb/n-GaInAsSb. This type of junction has little or no band bending near the junction. Thus, accumulated carriers can

move easily across the junction under an applied bias even if the dopant concentration is low. The p-$Cu_2O$/n-$In_2O_3$ junction has the same device structure. Thus its measured I-V characteristics are also linear [16,19,28].

When the junction is formed with same carrier type materials such as an n-n or p-p heterointerface, a large electron affinity difference induces large energy band bending at the interface. This type of band bending can form a quantum well. Electron or hole energy levels are quantized due to this steep energy gradient at the interface. These quantized energy levels prohibit the direct transport of electrons across the junction if energy levels are not matched with occupied emitting and empty accepting states. This steep band bending induces a Schottky-like junction so that I-V characteristics are rectifying. Finally, a p-n junction with a low electron affinity p-type material and a high electron affinity n-type material such as n-GaInAsSb/p-InAs and n-GaSb/p-GaInAsSb junction also induce larger energy barriers on both sides of the interface. Thus I-V characteristics are rectifying.

One of the unusual properties of broken band gap junctions is the potential to observe negative differential resistance (NDR) in the I-V characteristic. NDR is seen when the dopant concentrations of n-type InAs and p-type GaSb are $2x10^{17}$ and $5x10^{18}$ $cm^{-3}$ respectively [20].Recently, NDR is also observed in n-InAs/p-GaSb nanowire [21].The reasons of NDR are not well known yet.

For tunnel junctions in multi-junction solar cells, the broken-gap heterojunction resistance should be low since it adds to the series resistance. A resistance as low as $10^{-7}$ $\Omega$-$cm^2$, which is far lower than that needed for PV applications, can be achieved [22].

### 5.2.2. Metal oxide transparent conduction oxides and broken-gap heterojunctions.

High conductivity transparent conducting oxides (TCOs) [23,24] are often used as window layers in solar cells [25]. The use of these materials for the tunnel junction would make process integration easier since moderately and heavily TCOs are not particularly sensitive to environmental exposure. Yet, they are difficult to heavily dope both n- and p-type, making it hard to form tunnel junctions from these materials [26,27]. The formation energy of compensating defects is related to the Fermi level. Above a certain concentration of one type of dopant, a similar amount of compensating defects is generated. The net carrier concentration saturates in an effect called dopant concentration pinning [26]. Thus, one cannot form a heavily doped p-type film from materials such as ZnO, $SnO_2$, $In_2O_3$, $Ga_2O_3$, and CdO. Similarly, one cannot form a heavily doped n-type film from $Cu_2O$, NiO and $CuMO_2$ (M=Al, In, Cr and Ga).

While a tunnel homojunction is not possible, it is possible to use a heterojunction of an n-type and a p-type metal oxide for a tunnel junction. This brings up the question of what the optimal band alignment is in such a structure. A broken-gap metal-oxide heterojunction is one possible approach. When designing a broken-gap tunnel junction the electron affinities of the materials are the most important properties. Low and high electron affinities are desired for the n- and p-type materials, respectively. This is challenging in metal oxides because p-type TCOs are rare. $Cu_2O$ and $CuAlO_2$ are two of the most attractive materials for broken-gap tunnel junctions since they have the lowest electron affinities among the p-type TCOs. Next, considering n-type TCOs, $SnO_2$, $GaInO_3$

and $ZnSnO_3$ are the most likely to form broken-gap band alignment with $Cu_2O$ and $CuAlO_2$ [24].

Studies on broken-gap heterojunction with metal oxide films are very rare. Tanaka et al. studied the heterojunctions formed between $Cu_2O$ and several different n-type TCOs including ZnO, ITO and $In_2O_3$ [28]. Unlike junctions with other n-type TCOs, the p-$Cu_2O$/n-$In_2O_3$ junction showed linear I-V characteristics while the p-$Cu_2O$/n-ITO junction showed nonlinear I-V characteristics with a low energy Schottky barrier [28]. The band alignment of these ohmic p-$Cu_2O$/n-$In_2O_3$ junctions was not studied however it can be estimated from the I-V results, the band alignment of the $Cu_2O$/ITO junction, and the electron affinity difference between ITO and n-$In_2O_3$. Recently, Deuermeier et al. analyzed the band alignment of p-$Cu_2O$/n-ITO by X-ray photoemission spectroscopy (XPS). They found that the conduction band edge of n-ITO is 0.2 to 0.7 eV higher than the valence band edge of p-$Cu_2O$ depending on the ITO deposition conditions [29]. According to research results from multiple groups [24,30], the work function of $In_2O_3$ is 0.2 to 0.8 eV lower than that of ITO. From these results, it can be estimated that p-$Cu_2O$/n-$In_2O_3$ junctions may have a broken-gap band alignment. The linear I-V characteristics support this inference.

**5.3. Device simulation.**

Numerical simulation for the tunnel junction in a complete monolithic tandem solar cell requires simultaneous solution of current continuity and the Poisson equation, as well as a self-consistent treatment of quantum mechanical transport in the tunnel

junction. We use DESSIS – a commercially available multi physics device simulation tool for numerical simulation. Quantum transport at the broken-gap junction is solved by the Wentzel–Kramers–Brillouin (WKB) approximation. Device simulation is performed by self-consistently solving the current continuity equation, the Poisson equation and WKB approximation near the broken-gap junction interface. Optical absorption in the stacked multiple layers is calculated by transfer matrix methods [31].

Both the top and bottom cells are modeled as having uniform composition and dopant concentration. We assumed an ideal CGS top solar cell. CGS has a suitable band gap for the top solar cell in tandem devices. However, the reported maximum efficiency of CGS solar cells is only about 10% due to a large trap density and the band discontinuity between the CGS and buffer layer [32,33]. For an accurate simulation of a CIGS tandem PV cell, trap effects must be considered [34]. As technology advances, however, the efficiencies of CGS solar cells are rising [35,36], and alternative wide bandgap CIGS-based materials are being explored. Therefore, we have chosen to focus on the effects of the broken-gap heterojunction under the maximum performance condition (i.e. trap-free absorbers) in this chapter.

## 5.4. Transport models and simulation results of p-$Cu_2O$/n-$In_2O_3$ heterojunction.

### 5.4.1 Nonlocal interband transition model vs. ballistic transport model.

First, we look at the electrostatics of the heterojunctions. Figure 5.2 (a) shows the band diagrams near the band overlap region of the p-$Cu_2O$/n-$In_2O_3$ heterojunction for several band overlaps at thermal equilibrium. As previously shown for the $Cu_2O$/ITO

heterojunction [29], the band alignment can vary with film deposition conditions. We varied the band overlap from 0.0 eV to 0.2 eV to study the effect. For these calculations, the doping concentrations on both sides of the junction were taken to be $1.5\times10^{19}$ $cm^{-3}$ and the thickness of each layer was set to 200 nm. According to the Anderson model [37], the Fermi level should be constant throughout the device. Also, the energy band discontinuity should be maintained at the interface. The energy bands bend at the interface to satisfy both of these requirements [37]. As shown in Figure 5.2 (b), this band bending induces majority carrier accumulation on both sides of the junction near the interface. The wider the band overlap ($\Delta\chi$), the denser the accumulation layers concentrations at the interface.

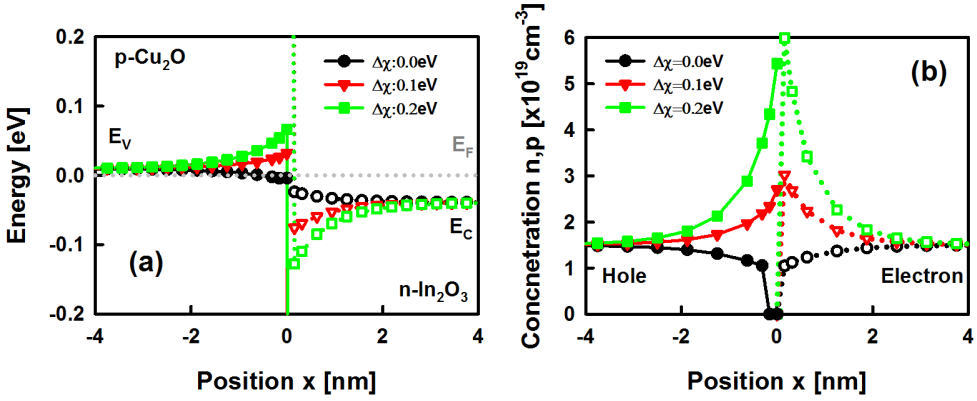


Figure 5.2. (a) The band diagram and (b) carrier concentrations for a $Cu_2O/In_2O_3$ broken-gap heterojunction near the band overlap region for different values of the band overlap ($\chi$) between 0.0 eV and 0.2 eV. In (a) the solid and dotted lines represent the valence and the conduction bands, respectively. In (b) the solid and dotted lines represent the hole and electron concentrations, respectively.

Next we studied transport. An accurate solution for carrier transport in a broken-gap heterojunction can be obtained by solving Schrodinger's and Poisson's equations self-consistently [38,39]. Quantum transport near the junction interface can also be treated by the WKB approximation.

Specifically, carrier transport in a broken-gap heterojunction occurs through two mechanisms in series, drift-diffusion from the charge neutral region to the interface and a nonlocal interband transition across the junction interface. After carriers move across the interface they recombine quickly and contribute current as shown in Figure 5.3.

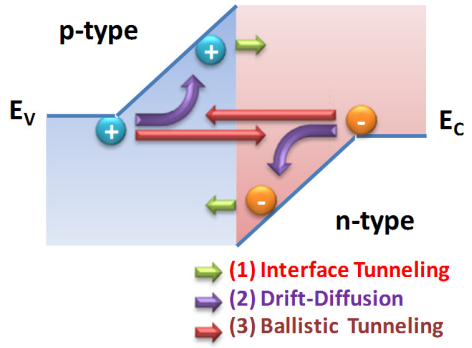


Figure 5.3. Possible current transport mechanisms in broken-gap heterojunctions: (1) interband transition at the interface (2) drift-diffusion and (3) ballistic transport.

Carrier transport is modeled by solving both the interband transition and the drift-diffusion transport in the quasi-neutral region simultaneously. At the heterojunction, the band alignment affects not only the band bending but also both the electric field and the carrier concentration at the interface as described above [40]. For the interface transition,

band bending at the interface is very important since the shape of the potential strongly affects the transmission coefficient. Similarly, the electric field and carrier concentration profiles near the junction interface are also important for the drift-diffusion model.

In addition to interband transition at the interface, ballistic transport between the edge of the charge neutral region and the junction interface, is also possible ((3) in Figure 5.3) when the accumulation width is very narrow and a strong built-in field is formed. Ballistic transport occurs when carriers move between bands with high kinetic energy before losing energy by scattering events [41]. When the electrons move into the accumulation region, they are accelerated by a strong built-in electric field and reach velocities substantially higher than the saturated or terminal velocity. This is the so called velocity overshoot effect. The electrons eventually scatter and lose the kinetic energy acquired from the field if the accumulation region is wide enough [41]. Since the scattering rate increases with kinetic energy, ballistic transport happens within a very short time and within a narrow region, generally no more than about ten nanometers. Thus, electrons can move ballistically across the accumulation region only if the accumulation width is narrower than the distance they travel without scattering (~10 nm) [41]. In this work, we simulate ballistic transport using direct transport from the edge of charge neutral region to the junction interface using the WKB approximation. This is appropriate because ballistic transport conserves the sum of the kinetic and potential energies.

In the WKB approximation, the transmission probability can be calculated for arbitrary potential shapes and the carrier energy can be larger or smaller than the potential

barrier. Interband tunneling current from the valence band to the conduction band ($J_{cv}$) is given by

$$J_{CV} = -q\int_{0^+}^{\infty}[R_{CV}(x) - G_{CV}(x)]dx, \tag{5-1}$$

where the difference between the recombination ($R_{cv}$) and generation rates ($G_{cv}$) is given as

$$R_{CV}(x) - G_{CV}(x) = \frac{A_{CV}^{*}}{qk}\left(\frac{dE_V(x)}{dx}\right)\Gamma_{CV}(\varepsilon, x)\times$$

$$\left[T_p(x)\log\left\{1 + Exp\left(\frac{E_{Fp}(x) - \varepsilon}{kT(x)}\right)\right\} - T_n(0^-)\log\left\{1 + Exp\left(\frac{E_{Fn}(0^-) - \varepsilon}{kT(0^-)}\right)\right\}\right]. \tag{5-2}$$

In equation (5-2), $A_{cv}^{*}$ is the Richardson constant, $E_{Fp,n}$ is Fermi level of hole and electron, $\varepsilon$ is the carrier energy, $E_v$ is the valence band edge energy, $q$ is charge, $k$ is the Boltzmann constant, $T$ is temperature and $T_n$ and $T_p$ are the transmission coefficients at the interface which is due to velocity mismatch for electrons and holes, respectively [31]. $x=0^-$ refers to the position where tunneling begins. We assume that the transmission coefficients are unity since the carriers that move across the junction recombine quickly with the majority carriers. The tunneling probability ($\Gamma_{cv}$) is given by

$$\Gamma_{CV}(\varepsilon, x) = \exp\left[-2\int_0^r \kappa(x', \varepsilon)dx'\right], \tag{5-3}$$

where, $\kappa$, $\varepsilon$ and $x$ are the wave vector, the energy of carriers and position respectively. The wave vector, $\kappa$, is

$$\kappa = \frac{\kappa_C \kappa_V}{\sqrt{\kappa_C^2 + \kappa_V^2}}, \tag{5-4}$$

where,

$$\kappa_{C,V} = \frac{\sqrt{2m_0 m_{e,h}^* \pm \left(E_{C,V}(x) - \varepsilon\right)}}{\hbar}, \tag{5-5}$$

$\hbar, m_{e,}, m_h$, $E_C$ and $E_V$ are the reduced Planck constant, the effective tunneling masses of the electron and the hole and the conduction band edge energy of n-type material and the valence band edge energy of the p-type material, respectively [31]. Parameters used in the simulations are listed in Table 5.1. Parameters for the CIGS solar cell simulations were taken from previous chapter.

Table 5.1. Physical parameters for simulation.

| Material | Dielectric Constant | Band gap [eV] | Electron Affinity [eV] | Mobility [$cm^2$/Vs] | Effective Tunneling mass |
|---|---|---|---|---|---|
| $MoSe_2$ | 18.0 | 1.2 | 4.4 | N:45, P: 15 | |
| NiO | 11.9 | 3.6 | 1.6 | N:45, P: 2 | |
| $Cu_2O$ | 7.11 | 2.1 | 3.0 | N:45, P: 15 | $m_h$: 0.84 [42] |
| $In_2O_3$ | 3.95 | 3.5 | 5.1 | N:45, P: 15 | $m_e$: 0.35 [43] |
| ZnO | 7.8 | 3.441 | 4.5 | N:45, P: 15 | |
| IZO | 3.95-7.8 | 3.5 | 5.0 – 4.5 | N:45, P: 15 | |

We studied the I-V characteristics of p-$Cu_2O$/n-$In_2O_3$ broken-gap heterojunctions and compared the two tunneling models described above. Even though a band overlap

exists, the I-V characteristic of the broken-gap junction is linear as proven in the n-InAs/p-GaSb junction.

Figure 5.4 compares the I-V characteristics of the p-$Cu_2O$/n-$In_2O_3$ junction calculated using the interface interband transition model (Figure 5.4 (a)) and the ballistic transport model (Figure 5.4 (b)).

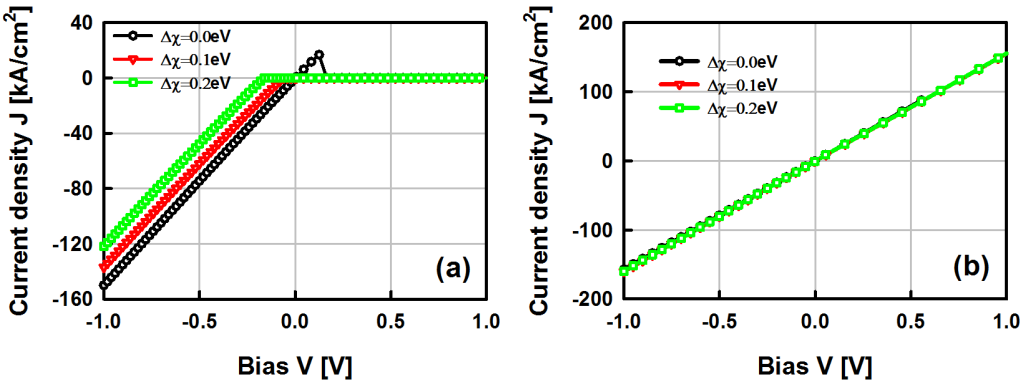


Figure 5.4. Calculated I-V characteristics for (a) the interface-interband transition model and (b) the ballistic transport model for different values of the band overlap (χ) between 0.0 eV and 0.2 eV.

Under near flat-band conditions where the band overlap is zero, both tunneling models predict linear I-V characteristics in the reverse bias region. However significant differences exist between the two model predictions when there is band overlap. Specifically, a cutoff voltage ($V_C$) appears for the interface interband transition model in reverse bias (negative voltage) when the band overlap is more than 0.1 eV. Current stops flowing above this cutoff value. There is no cutoff voltage predicted with the ballistic

transport model. Instead the junction is ohmic over the calculated range, with current flowing both in forward and reverse bias. We note the importance of this difference by pointing out that in this application the junction must be operated in reverse bias and only very small voltage drops can be allowed.

At thermal equilibrium, no current should flow. However, band bending creates an electric field which induces a drift current toward the junction. The carrier concentration profile must cause the induced diffusion current to cancel the drift current for both carriers as in the Einstein relation. According the simulation results shown in Figure 5.4 (a), even if a small bias is applied, when carriers are accumulated at the interface the diffusion current by accumulated carriers cancels the drift current and thus no significant current flows. From current cancelation by accumulated carriers at the interface, we can estimate the cutoff voltage analytically by calculating a flat band voltage at which carriers are not accumulated at the interface. As shown in Figure 5.2 (a), the energy difference from the valence band edge of p-type to the conduction band edge of n-type in charge neutral region is 49 meV. Therefore, when the band overlaps are 0.1 and 0.2 eV the estimated cutoff voltage is -51 mV and -0.151 V respectively. The corresponding cutoff voltages calculated by simulation are -61 mV and -0.16 V, respectively. The approximate calculation provides a good match to the simulation results. A wider band overlap increases the band bending as shown in Figure 5.2 (a), thus a larger reverse bias is required to remove the accumulated carriers at the interface. The cutoff voltage shifts to a larger value due to the wider band overlap as shown in Figure 5.4 (a).

In forward bias, the carrier accumulation is increased due to the increase of band bending at the interface. The diffusion current by accumulated carriers also increases and cancels out the drift current. An applied reverse bias reduces the band bending and the accumulated carrier concentration. The current does not flow until the accumulated carriers are removed. After the band becomes flat, majority carriers begin to be injected to the interface by drift, thus current flows through the device. When the band overlap is zero no carriers accumulate at thermal equilibrium. Carrier accumulation begins at 0.124 V in forward bias. Thus current flow below 0.124 V and a peak voltage ($V_P$) is observed in I-V characteristics. However, the experimentally measured I-V characteristics of broken-gap heterojunctions with band overlap do not show a cutoff voltage. For example, the band overlap in InAs/GaSb heterojunction is between 0.12 and 0.17 eV, yet the I-V characteristics of this junction are linear without a cutoff voltage. Thus, the interface transition model fails to explain the observed I-V characteristics of broken-gap heterojunctions studied to date [15-22].

In contrast, the I-V characteristics of a broken-gap heterojunction predicted using a ballistic transport model is linear and exhibits current flow both in forward and reverse bias as shown in Figure 5.4 (b). Since ballistic transport occurs directly between the charge neutral region and the interface, the transmission coefficient depends only on the barrier shape and not on the profiles of accumulated carriers near the interface. For carriers to move ballistically, the charge accumulation width should be narrower than the ballistic mean free path and the electric field should be high. In the p-$Cu_2O$/n-$In_2O_3$ junction studied here, the charge accumulation widths on both sides of the junction are

less than 4 nm as shown in Figure 5.2 and the maximum electric field is 1 MV/cm. These narrow depletion widths and high electric fields lead to carrier conduction by ballistic transport across this junction. Increasing the energy band overlap produces a higher electric field at the interface making ballistic tunneling more likely. The resistance due to ballistic transport is determined by the transmission coefficient. When the transmission coefficient is unity, the resistance of ballistic transport at the interface is lower than the series resistance of the charge neutral region. As a result, the series resistance of junction does not determine the I-V characteristics. Thus, for this situation the I-V characteristics do not depend on the width of the band overlap ($\Delta\chi$) since the transmission coefficient is nearly unity due to the narrow accumulation width as shown in Figure 5.4 (b). This is the reason that a broken band-gap junction can achieve a junction resistance as low as $10^{-7}$ $\Omega$-cm$^2$ in InAs/GaSb junctions. We note that in a tandem device operating under unconcentrated sunlight will generate about 20 mA/cm$^2$. For a 1 mV potential drop at the tunnel junction, the maximum allowable resistance could be as high as $5\times10^{-2}$ $\Omega$-cm$^2$, suggesting that a broken-gap tunnel junction could easily achieve this goal.

### 5.4.2 The effect of doping concentration.

One of difficulties in fabricating a tunnel junction is controlling the carrier concentration profiles in the heavily doped n- and p-type layers. Specifically, maintaining steep doping profiles near the junction between two polycrystalline films is extremely difficult. Fundamentally, the energy band alignment of the broken-gap heterojunction is such that the Fermi level is located in the conduction and valence bands of the n- and p-

type layers, respectively and tunneling can occur even when these layers are only lightly doped.

Although many n-type TCOs can be doped higher than $1\times10^{20}$ $cm^{-3}$, heavily doped p-type TCOs are much more difficult to achieve. We therefore investigate the limits on the doping concentration in $Cu_2O$ when the doping concentration in n-type $In_2O_3$ is fixed at $5\times10^{19}$ $cm^{-3}$. The thicknesses of n and p-type layers were fixed at 200 nm.

When the doping concentration is low, a peak voltage ($V_P$) or cutoff voltage ($V_C$) is observed in I-V characteristics. The peak voltage ($V_P$) is the voltage at which current is drops abruptly in forward bias as in a tunnel diode. The cutoff voltage ($V_C$) is the voltage at which the current begins to flow under reverse bias as shown in Figure 5.5 (c).

Figure 5.5 (a) shows the typical I-V characteristics and energy band diagrams in each different carrier transport region of the p-$Cu_2O$/n-$In_2O_3$ junction with a low dopant concentration on one side, when the doping concentration of $In_2O_3$ and $Cu_2O$ are $5\times10^{19}$ $cm^{-3}$ and $10^{17}$ $cm^{-3}$ respectively. At thermal equilibrium (point A), the $Cu_2O$ band is pulled down near the interface due to the heavy dopant concentration in the $In_2O_3$. Thus the valence band edge of $Cu_2O$ in the charge neutral region is higher than the conduction band of $In_2O_3$. In reverse bias (point B), band bending increases the electron concentrations in p-$Cu_2O$ at the interface. Electrons are injected into the n-$In_2O_3$ across the junction by interband transition. Thus, current flows. In forward bias, electrons move from n-$In_2O_3$ to p-$Cu_2O$ by not only diffusion but also interband transition at the interface until the valence band edge of $Cu_2O$ at quasi neutral region is equal to the conduction

band edge of $In_2O_3$ (point C). When the valence band edge of $Cu_2O$ at in quasi neutral region is lower than the conduction band edge of $In_2O_3$ holes are accumulated at the junction interface. And, the compensation of drift and diffusion currents due to accumulated holes in opposite directions blocks the interband transition at the interface and only the small diffusion current remains. Thus the current changes abruptly and a peak voltage is observed at point C. This abrupt current change produces the NDR often associated with tunnel junctions. NDR was observed in a broken-gap n-InAs/p-GaSb heterojunction at a moderate doping concentration [20]. Since the diffusion current increases exponentially with voltage in this regime, at sufficiently high voltage (point D), one finds a measurable current once again. The peak voltage is the voltage which makes the energy band flat. It is determined by the difference between the valence band edge of $Cu_2O$ in charge neutral region and the conduction band edge of $In_2O_3$ in charge neutral region at thermal equilibrium. When valence band edge of $Cu_2O$ is higher than the conduction band edge of $In_2O_3$ the peak voltage becomes positive. In the reverse bias case, the peak voltage changes to a cutoff voltage since carriers cannot transport across the junction until the energy band becomes flat. Thus at sufficiently low carrier concentrations the peak voltage becomes the cutoff voltage.

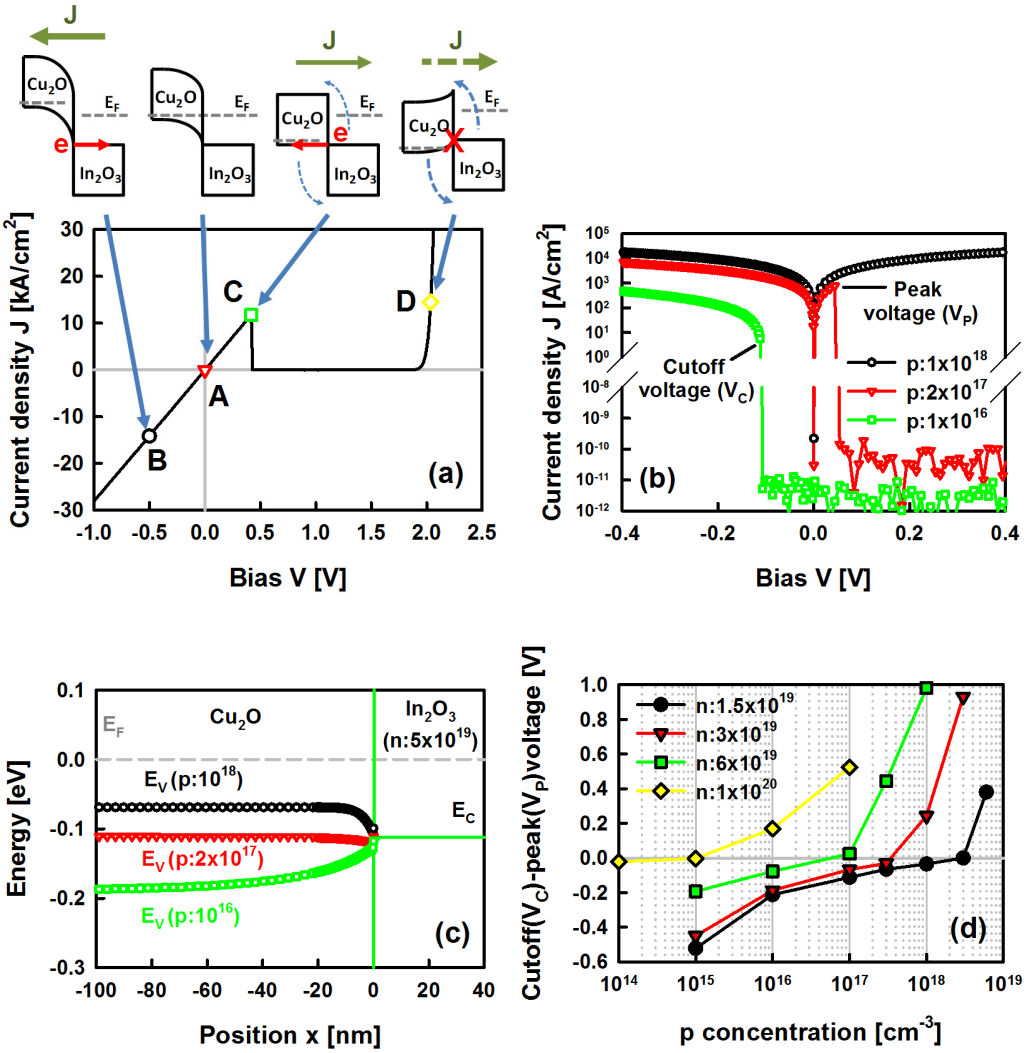


Figure 5.5. (a) I-V characteristics of $10^{17}$ $cm^{-3}$ p-$Cu_2O$ and $5\times10^{19}$ $cm^{-3}$ n-$In_2O_3$ broken-gap heterojunction and pictorial band diagrams for each transport region, (b) semi-log scale I-V characteristics, (c) band diagrams of $5\times10^{19}$ $cm^{-3}$ $Cu_2O$ with $10^{16}$, $2\times10^{17}$ and $10^{18}$ $cm^{-3}$ $In_2O_3$ at thermal equilibrium and (d) cutoff ($V_C$) and peak voltages ($V_P$) due to the dopant concentration of $Cu_2O$ and $In_2O_3$.

Figure 5.5 (b) and 5.5 (c) show the I-V characteristics and band diagrams of p-$Cu_2O$/n-$In_2O_3$ with $Cu_2O$ dopant concentrations of $1\times10^{16}$, $2\times10^{17}$ and $1\times10^{18}$ $cm^{-3}$, with the carrier concentration in $In_2O_3$ fixed at $5\times10^{19}$ $cm^{-3}$. With $1\times10^{18}$ $cm^{-3}$ in $Cu_2O$, current flows within ±0.4 V without discontinuity. However, when the dopant concentration of $Cu_2O$ is $2\times10^{17}$ $cm^{-3}$ the peak voltage is 44 mV since the valence band edge of $Cu_2O$ is only slightly higher (6 meV) than the conduction band edge of $In_2O_3$ at that voltage as shown in Figure 5.5 (c). When the dopant concentration of $Cu_2O$ becomes $1\times10^{16}$ $cm^{-3}$ the valence band edge of $Cu_2O$ is lower than the conduction band edge of $In_2O_3$ as shown in Figure 5.5 (c) and cutoff voltage is -0.11 V. No peak voltage is observed. Figure 5.5 (d) shows the peak and cutoff voltage due to the dopant concentration in p-$Cu_2O$ and n-$In_2O_3$. Decreasing the dopant concentration in p-$Cu_2O$ causes the peak voltage to move to the cutoff voltage. For tunnel junctions in multi-junction solar cells, the voltage drop in the tunnel junction should be minimized and so a cutoff voltage should be avoided. The lowest possible dopant concentration of p-$Cu_2O$ is determined when the cutoff and peak voltages are zero. With $1.5\times10^{19}$ $cm^{-3}$ in n-$In_2O_3$, the dopant concentration of $Cu_2O$ can be to $2\times10^{17}$ $cm^{-3}$ without an additional voltage drop. When the dopant concentration in n-$In_2O_3$ increases to $1\times10^{20}$ $cm^{-3}$ linear the dopant concentration of $Cu_2O$ can be as low as $2\times10^{15}$ $cm^{-3}$ with an addition of only $3.6\times10^{-3}$ Ω-$cm^2$ to the resistance per unit area of the p-$Cu_2O$/n-$In_2O_3$ broken-gap junction device. These results show that broken-gap junctions can provide low resistance ohmic junctions, even with a relatively low dopant concentration on one side of the junction.

### 5.4.3 Broken-gap heterojunction vs. barrier tunnel junction.

Figure 5.6 shows the I-V characteristics of a GaAs tunnel diode and a p-$Cu_2O$/n-$In_2O_3$ broken-gap heterojunction. The model parameters for GaAs tunnel diode was adopted from Hermle et al. [44]. The thicknesses of both the n-type and p-type layers were taken to be 200 nm. For tunneling to occur in a GaAs tunnel junction, the Fermi level should be placed above and below the energy band edge of the n- and p-type material respectively. Therefore the dopant concentrations should be higher than the density of states in the conduction band and the valence band - generally higher than $10^{19}$ $cm^{-3}$. The dopant concentrations of the GaAs tunnel diode are $3\times10^{19}$ and $5\times10^{19}$ $cm^{-3}$ in both n- and p-types. The dopant concentration of n-$In_2O_3$ is $5\times10^{19}$ $cm^{-3}$ the same as the most heavily doped side of the GaAs tunnel diode to compare characteristics. Since a broken-gap junction has linear I-V characteristics even with a moderate dopant concentration, the dopant concentrations of p-$Cu_2O$ are set to $2\times10^{17}$ and $1\times10^{18}$ $cm^{-3}$.

As shown in Figure 5.6, in a GaAs tunnel diode the current increases exponentially in reverse bias. In forward bias it increases to a peak current point ($I_P$) at peak voltage ($V_P$) then decrease to zero near zero bias. When decreasing the doping concentration from $5\times10^{19}$ $cm^{-3}$ to $3\times10^{19}$ $cm^{-3}$ the current density decreases drastically from 1.05 $kA/cm^2$ to 20.6 $A/cm^2$ at -50 mV. The I-V characteristics of p-$Cu_2O$/n-$In_2O_3$ junction are linear. The junction with $1\times10^{18}$ $cm^{-3}$ in $Cu_2O$ has a high slope compared to the junction with the low dopant concentration and so has a low resistance.

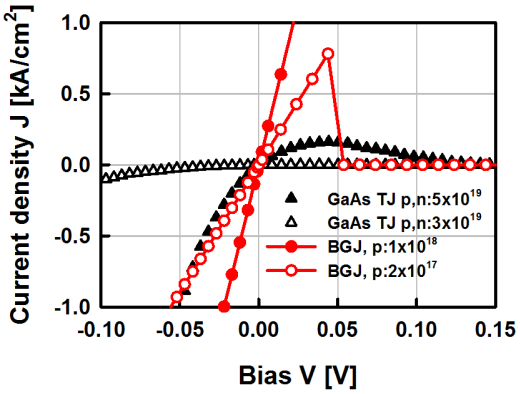


Figure 5.6. Comparison of I-V characteristics between GaAs tunnel junction (symbol) and $Cu_2O/In_2O_3$ heterojunction (line with symbol).

The tunneling current $J_t$ of GaAs tunnel junction is given by

$$J_t \propto F \exp\left(-\frac{4\sqrt{2m^*}E_g^{3/2}}{3q\hbar F}\right), \tag{5-6}$$

where, $m^*$ is effective tunneling mass, $E_g$ is the band gap [5]. The electric field, $F$, is given by

$$F = \left[\frac{q}{2\varepsilon_s}\frac{N_D N_A}{N_D + N_A}(V_{bi} - V)\right]^{1/2}, \tag{5-7}$$

where, $N_D$ and $N_A$ are the dopant concentrations in the n and p regions, respectively, $\varepsilon_s$ is the dielectric constant, and $V_{bi}$ is the built-in potential [5]. As shown in equation(5-7), the electric field in tunnel junction is proportional to the square root of the dopant concentration and the reverse bias. Thus the tunneling current in a GaAs tunnel diode increases exponentially with both reverse bias and doping concentration. As a result, the

resistance of a GaAs tunnel diode has a maximum at zero bias. However, the voltage drop in a multi-junction solar cell tunnel junction should be minimized. Therefore, even a GaAs tunnel junction with high doping concentrations in both n- and p-type materials can have a much higher resistance than a broken-gap junction. When the dopant concentration of a GaAs tunnel junction is $5\times10^{19}$ $cm^{-3}$ in both sides, the resistance is $1.1\times10^{-4}$ $\Omega$-$cm^2$. When the dopant concentration decreases to $3\times10^{19}$ $cm^{-3}$ the resistance increases to $6.3\times10^{-3}$ $\Omega$-$cm^2$. On the other hand the total resistance of $1\times10^{18}$ $cm^{-3}$ p-$Cu_2O$/n-$In_2O_3$ junction is $2.2\times10^{-5}$ $\Omega$-$cm^2$, limited only by the series resistance. When the dopant concentration of p-$Cu_2O$/n-$In_2O_3$ decreases to $2\times10^{17}$ $cm^{-3}$ the resistance increases only to $5.6\times10^{-5}$ $\Omega$-$cm^2$. Thus, even when the doping concentration of p-$Cu_2O$/n-$In_2O_3$ is lower than that of the GaAs tunnel junction, the resistance is much less.

### 5.5. Top and bottom single solar cells with $Cu_2O/In_2O_3$ heterojunction interface.

Next, the performance of top and bottom CIGS-based solar cells with a p-$Cu_2O$/n-$In_2O_3$ tunnel junction was investigated. For tandem PV devices, the optimized band gaps of the top and the bottom solar cells under AM 1.5 illumination are 0.94 eV and 1.64 eV, respectively [45]. The band gap of the CIGS material system approximately covers this range and can be varied from 1.01 eV for $CuInSe_2$ (CIS) to 1.68 eV for $CuGaSe_2$ (CGS) Thus, we chose CGS and (CIS) for the absorber layers in the top and bottom cells, respectively.

#### 5.5.1. Top CGS solar cell to $Cu_2O$ heterojunction interface.

The device structures and performance results of top solar cells with broken-gap heterojunction are shown in Figure 5.7 (a). The window layers were comprised of a 150 nm thick n-type ZnO:Al and a 100 nm thick n-type ZnO. The dopant concentrations of the 150 nm thick and 100 nm thick n-ZnO were $10^{19}$ $cm^{-3}$ and $10^{17}$ $cm^{-3}$, respectively. A 70 nm thick n-type ($5\times10^{15}$ $cm^{-3}$) CdS was used as a buffer layer between the CGS and the n-ZnO. A 1.6 μm thick p-type ($10^{16}$ $cm^{-3}$) CGS layer was used for the absorber layer. A 10 nm thick $MoSe_2$ was used for the contact layer between the top solar cell and the broken-gap heterojunction.

The valence band edge of $MoSe_2$ (at 5.6 eV below vacuum level) is close to valence band of CGS (at 5.68 eV below vacuum level). As a result, $MoSe_2$ forms an ohmic contact with CGS. $MoSe_2$ is important not only for forming ohmic contacts but also to act as a seed layer for CIGS growth as will be described in another chapter [46]. According to a previous study, $MoSe_2$ layers formed by selenization of Mo have transmission problems on TCO layers [13,14]. However, when deposited by sputtering, the optical band gap of $MoSe_2$ is about 1.2 eV with a sharp absorption edge. We assumed that this layer has the same optical (n-k) parameters as sputtered $MoSe_2$ [47]. The doping concentration of $MoSe_2$ was taken to be $10^{18}$ $cm^{-3}$. Since $Cu_2O$ is a p-type material ($10^{19}$ $cm^{-3}$) it should contact the CGS absorber of the top cell. A 100 nm thick p-type $Cu_2O$ was placed below the $MoSe_2$ to complete the top cell.

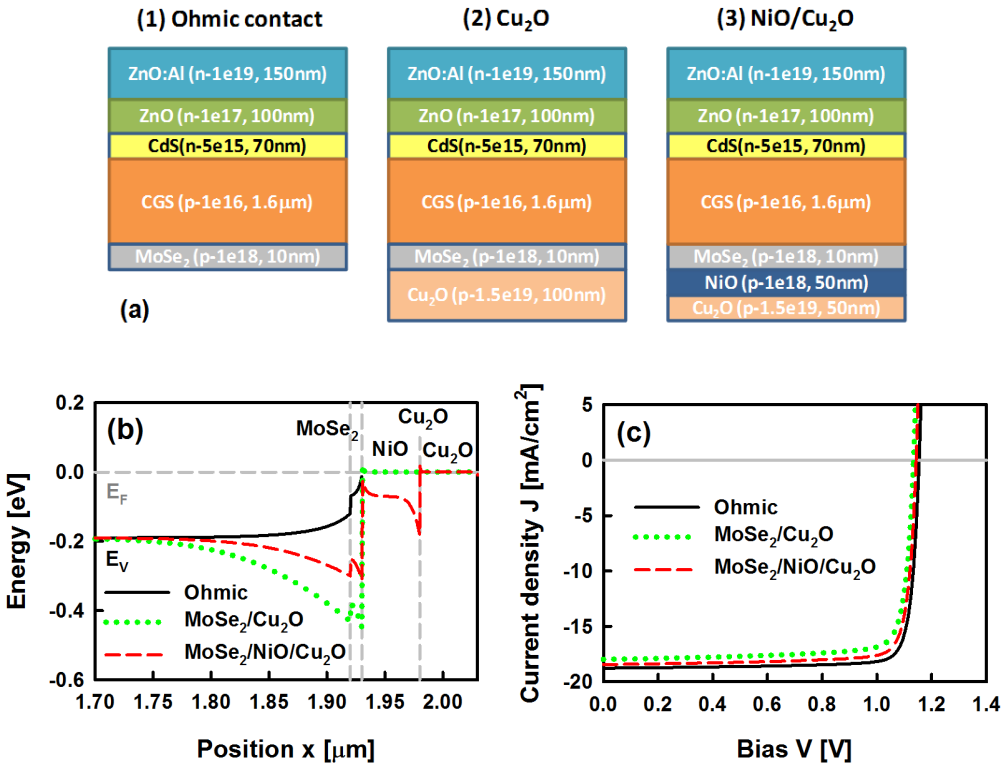


Figure 5.7. (a) Three top solar cell structures with different bottom contacts for comparison (1) an ohmic contact, (2) using $Cu_2O$ only, and (3) using $Cu_2O$ with a NiO buffer layer and comparison of calculated (b) valence band diagrams and (c) I-V characteristics of $CuGaSe_2$ top solar cells with different bottom contacts.

Figure 5.7 (b) shows the valence band diagrams near the interface between the top solar cell and ideal ohmic contact (solid lines), $Cu_2O$ (dotted line) and NiO buffer and $Cu_2O$ (dashed line). When the bottom contact is ideal ohmic, the valence band of CGS bends toward the Fermi level. Holes in valence band of CGS move easily to the bottom contact because there is no barrier between the top solar cell and the bottom contact. The reported valence band edges of $MoSe_2$ and $Cu_2O$ are 5.6 eV [48] and 5.1 eV [29] below

the vacuum level, respectively, so that a 0.5 eV energy difference exists between these two materials. Therefore, when $Cu_2O$ is directly contacted with $MoSe_2$ an energy barrier is formed on the valence band of CGS. Since the extremely thin layer of $MoSe_2$ is fully depleted and the dopant concentration of CGS is lower than that of $Cu_2O$, CGS is depleted from the bottom contact. This barrier would block hole transport to the tunnel junction. To reduce this barrier, we introduced a p-type buffer layer between the $MoSe_2$ and $Cu_2O$. The valence band edge of buffer materials is located between the valence band edge of CGS and $Cu_2O$. This kind of buffer can divide the 0.5 eV barrier between CGS and $Cu_2O$ into smaller barriers. NiO is a good candidate as shown in Table 5.1 [30]. When 50 nm of p-type ($10^{18}$ $cm^{-3}$) NiO is inserted between $MoSe_2$ and $Cu_2O$, the barrier height in CGS is reduced from 0.26 eV to 0.12 eV. Another barrier is generated in NiO at the interface between NiO and $Cu_2O$. Due to the high dopant concentration in NiO, the barrier height and width is narrow (7 nm) and low (0.1 eV) compared to the barrier between CGS and NiO. Therefore it does not affect hole transport.

The I-V characteristics and the performance summary of the top solar cells in Figure 5.7 (a) are shown in Figure 5.7 (c) and Table 5.2 respectively. With an ideal ohmic bottom contact (solid line in Figure 5.7 (c)), the short circuit current ($J_{SC}$) and open circuit voltage ($V_{OC}$) are 18.77 mA/$cm^2$ and 1.154 V respectively. The efficiency of the top solar cell is 18.7%. When $Cu_2O$ is connected with $MoSe_2$ (dotted line in Figure 5.7 (c)) $J_{SC}$ and $V_{OC}$ are 18 mA/$cm^2$ and 1.134 V. The efficiency decreases to 17.0%. The $J_{SC}$ loss, 5%, is the main factor in reducing the efficiency. The barrier between $MoSe_2$ and $Cu_2O$ hinders hole transport from CGS to the bottom contact and increases the recombination of

photogenerated electron-hole pairs (EHPs) in CGS. The insertion of the NiO buffer layer between $MoSe_2$ and $Cu_2O$ recovers $J_{SC}$ to 18.44 mA/cm$^2$ by reducing the barrier (dashed line in Figure 5.7 (c)). The efficiency rebounds to 17.9%, showing that the NiO buffer layer is effective in improving device efficiency.

Table 5.2. The simulation results of top PV cells shown in Figure 5.7 (a) with various different top contacts.

| | | Reference | BGJ | Buffer/BGJ |
|---|---|---|---|---|
| Structure | Top Cell | | ZnO:Al, n-type, $1\times10^{19}$, 150 nm<br>ZnO, n-type, $1\times10^{17}$, 100 nm<br>CdS, n-type, $5\times10^{15}$, 70 nm<br>$CuGaSe_2$, p-type, $1\times10^{16}$, 1.6 μm<br>$MoSe_2$, p-type, $1\times10^{18}$, 10 nm | |
| | Broken-gap junction | Ohmic Contact | $Cu_2O$, $1.5\times10^{19}$, 100 nm | NiO, $1\times10^{18}$, 50 nm<br>$Cu_2O$, $1.5\times10^{19}$, 50 nm |
| Perform-ance | Efficiency [%] | 18.66 | 16.99 | 17.90 |
| | $V_{oc}$ [V] | 1.154 | 1.134 | 1.144 |
| | $J_{SC}$ [mA/cm$^2$] | 18.77 | 17.97 | 18.44 |
| | FF [%] | 86.15 | 83.34 | 84.86 |

### 5.5.2. Bottom CIS solar cell to $In_2O_3$ heterojunction interface.

Figure 5.8 (a) shows the device structures that were simulated and the performance of bottom solar cells with a broken-gap heterojunction. A 100 nm thick n-

type ZnO ($10^{17}$ $cm^{-3}$) was used for the n-side of the p-n junction and a 70 nm thick n-type ($5\times10^{15}$ $cm^{-3}$) CdS buffer layer was placed between the n-type ZnO and 2 μm thick p-type ($10^{16}$ $cm^{-3}$) CIS absorber. In single junction solar cells, low resistivity TCOs are deposited on top of the ZnO window layer to reduce the series resistance due to lateral conduction in resistive ZnO. However, in the bottom cell, current only flows vertically. Lateral conduction occurs only in the top cell. Therefore, a TCO window layer is not required in the bottom solar cell.

Conduction band diagrams of bottom solar cells are shown in Figure 5.8 (b). With $In_2O_3$ on top of the bottom cell, an energy barrier is formed in the conduction band at the interface between ZnO and $In_2O_3$ (dotted line in Figure 5.8 (b)). This happens because the electron affinity of $In_2O_3$ is lower (5.1 eV [30] below the vacuum level) than that of ZnO (4.5 eV [24] below the vacuum level). It has been reported that a low resistivity TCO can be formed by co-deposition of $In_2O_3$ and ZnO [24]. Then the composition of $In_2O_3$-ZnO film (IZO) can be graded to eliminate the barrier. Figure 5.8 (b) shows the conduction band diagrams of top solar cells with100 nm thick $In_2O_3$ and 50 nm thick $In_2O_3$ and 50 nm thick compositionally graded ZnO to $In_2O_3$ from top surface of the bottom solar cell removing the energy barrier between $In_2O_3$ and ZnO.

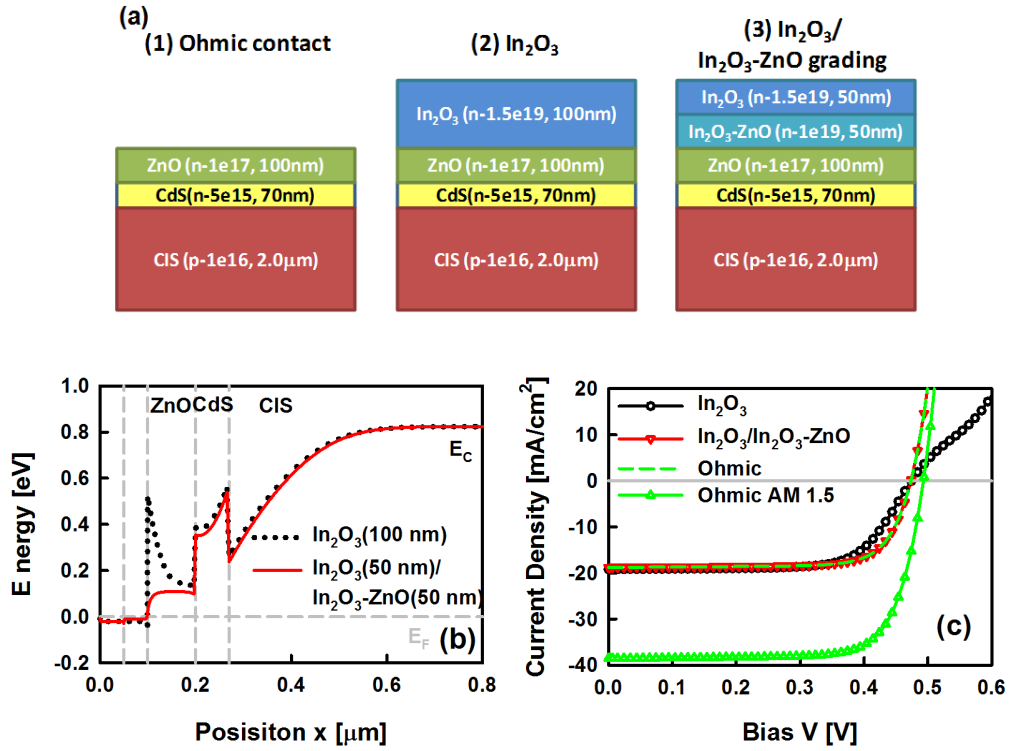


Figure 5.8. (a) Three bottom solar cell with top contact structures for comparison (1) an ohmic contact, (2) using $In_2O_3$ only, and (3) using $In_2O_3$/graded $In_2O_3$-ZnO layer, comparison of calculated (b) conduction band diagrams and (c) I-V characteristics of $CuInSe_2$ bottom solar cells with different top contacts.

The I-V characteristics and performance summary of top solar cells in Figure 5.8 (a) are shown in Figure 5.8 (c) and Table 5.3 respectively. With an ohmic contact on top of the bottom cell, $J_{SC}$ and $V_{OC}$ are 38.52 mA/cm$^2$ and 0.493 V respectively. The efficiency of the bottom solar cell is 14.3% under AM 1.5 illumination. However, the bottom solar cell must share the solar spectrum with top cell. We calculated the

component of the solar spectrum reaching the bottom cell assuming the full tandem structure (screened spectrum). Then $J_{SC}$, FF, and $V_{OC}$ are 18.76 mA/cm$^2$, 75.1% and 0.473 V, respectively, and the efficiency decreases to 6.67%. With $In_2O_3$ on top of the bottom solar cell, the power conversion efficiency decreases to 5.77% under the screened spectrum. The decrease in efficiency is due to the reduction in the $J_{SC}$ and FF to 17.86 mA/cm$^2$ and 68.18% respectively compared to the bottom cell with an ohmic contact.

Table 5.3. The simulation results of bottom PV cells shown in Figure 5.8 (a) with various different top contacts.

| | | Reference | BGJ | Buffer/BGJ |
|---|---|---|---|---|
| Structure | Broken-gap junction | Ohmic Contact | $In_2O_3$, $1\times10^{19}$, 100 nm | $In_2O_3$, $1\times10^{19}$, 50 nm |
| | | | | IZO, $1\times10^{19}$, 50 nm |
| | Bottom Cell | ZnO, n-type, $1\times10^{17}$, 100 nm | | |
| | | CdS, n-type, $5\times10^{15}$, 70 nm | | |
| | | $CuInSe_2$, p-type, $1\times10^{16}$, 2.0 μm | | |
| Perform-ance | Intensity | 1 Sun | Top PV cell screened | |
| | Efficiency [%] | 14.26 | 6.67 | 5.77 | 6.65 |
| | $V_{oc}$ [V] | 0.493 | 0.473 | 0.474 | 0.473 |
| | $J_{SC}$ [mA/cm$^2$] | 38.52 | 18.76 | 17.86 | 18.70 |
| | FF [%] | 75.10 | 75.13 | 68.18 | 75.12 |

The energy barrier in ZnO at the interface between ZnO and $In_2O_3$ hinders electron transport and induces a kink in the I-V characteristic near the open circuit

voltage as shown in Figure 5.8 (c). This kink degrades the FF. According to Gloeckler et al. this forward bias kink is due to an electron barrier in the conduction band at the CIGS/CdS interface. The kink occurs when the conduction band edge of CdS is higher than that of CIGS and the conduction band discontinuity between CdS and CIGS is large [49]. Similarly, the large conduction band discontinuity between $In_2O_3$ and ZnO depletes electrons in ZnO and moves the conduction band of CdS upward compared to the bottom cell with an ohmic contact (Figure 8 (b)). This shift in the conduction band of CdS blocks electron transport at high forward bias and degrades the FF. A graded $In_2O_3$-ZnO layer between $In_2O_3$ to ZnO restores the efficiency to 6.65%, the $J_{SC}$ to 18.7 mA/cm$^2$ and the fill factor to 75.1%.

### 5.6. CGS/CIS Tandem solar cell

Figure 5.9 (a) shows the structure and band diagram for an optimized CGS/CIS tandem solar cell. The design shown in Figure 5.9 (a) incorporates the lessons from previous sections. Specifically, the top solar cell is comprised of a 1.6 μm thick p-type CGS absorber with ZnO:Al/ZnO window layers, a CdS buffer layer and a $MoSe_2$ contact layer. The bottom solar cell is comprised of a 2 μm thick p-type CIS absorber with a ZnO window layer and a CdS buffer layer. The $Cu_2O$-$In_2O_3$ broken-gap heterojunction is used to connect the top and bottom solar cells in series. A NiO buffer layer is used in the top cell between the $MoSe_2$ and the $Cu_2O$ layers. Similarly, a graded $In_2O_3$-ZnO layer is inserted in the bottom cell between the $In_2O_3$ and ZnO layers. The band diagram at thermal equilibrium is shown on the right of Figure 5.9 (a).

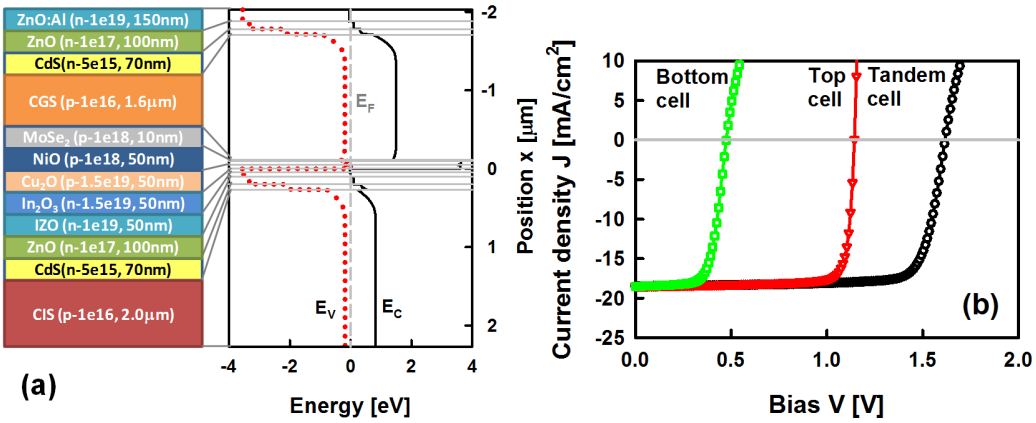


Figure 5.9. (a) The optimized tandem CGS/CIS solar cell structure and its band diagram and (b) I-V characteristics of just the CGS (top cell), just the CIS (bottom cell) and the tandem CGS/CIS tandem solar cell in (a).

The performance of the CGS/CIS tandem solar cell is shown in Table 5.4 and Figure 5.9 (a). Figure 5.9 (b) shows the I-V characteristics of the top, bottom, and tandem solar cells. With a p-$Cu_2O$/n-$In_2O_3$ broken-gap heterojunction, the tandem CGS/CIS solar cell works successfully. The efficiency of the tandem solar cell is 24.1% while the efficiencies of the top and bottom cells are 17.5% and 6.7% respectively. The $V_{oc}$ of the tandem device (1.62 V) is equal to the sum of the $V_{oc}$ for the top and bottom PV cells (1.14 V, and 0.47 V, respectively). Due to current continuity, the $J_{SC}$ of a tandem cell is limited by lowest value of the two cells. For this device, $J_{SC}$ is 18.5 mA/cm$^2$, close to that of the top cell. Further structure optimization could be done to increase the current generated by the top cell thereby improving the overall efficiency. The FF of the tandem PV cells is substantially lower than that for the top cell (82.9%). Due to the narrower

bandgap of CIS compared to CIGS, a higher energy barrier forms at the CdS/CIS interface. This barrier impedes electron transport, reducing the FF of the bottom cell to 75.1% (Figure 5.9 (b)). The FF of the tandem cell is determined by the sum of FFs of top and bottom solar cells weighted by efficiency. Thus it becomes 80.5%. The efficiency of a tandem solar cell is the sum of the efficiencies of top and bottom solar cells. The efficiencies of top and bottom cell in tandem solar cell are similar to the results of single solar cells when one takes into account screening by top solar cell. The ideal maximum efficiency of a CGS/CIS tandem solar cells is 25.3%, the sum of the top and bottom solar cells with ohmic contacts. With p-$Cu_2O$/n-$In_2O_3$ broken-gap heterojunction, the efficiency of CGS/CIS tandem cell is 24.1% in this work. This efficiency degradation is mainly due to the energy barrier between the top cell and p-$Cu_2O$. New process techniques such as compositional grading can reduce this barrier and improve the efficiency to a value close to the ideal case. The broken-gap heterojunction is a promising tunnel junction candidate for connecting top and bottom solar cells in a multi-junction PV device without performance loss.

Table 5.4. The performance of top, bottom and CGS/CIS tandem PV cells.

| | Top Cell | Bottom Cell | Tandem Cell |
|---|---|---|---|
| Efficiency [%] | 17.5 | 6.47 | 24.1 |
| $V_{oc}$ [V] | 1.14 | 0.473 | 1.62 |
| $J_{SC}$ [mA/cm$^2$] | 18.5 | 18.5 | 18.5 |
| FF [%] | 82.9 | 73.9 | 80.5 |

Finally, we wish to point out that the quoted efficiencies can be further improved through the types of compositional and dopant grading used in single junction CIGS devices.

**5.7. Conclusion.**

A broken-gap p-n heterojunction, where the conduction band edge of the n-type material is equal to or lower in energy than the valence band edge of the p-type material, is studied as a potential tunnel junction in CIGS-based tandem solar cells. The broken-gap junction has a low resistance and linear I-V characteristic in both forward and reverse bias. The effectiveness of a specific broken-gap heterojunction between p-type $Cu_2O$ and n-type $In_2O_3$ in a multi-junction solar cell was studied using numerical simulation with DESSIS, a commercially available device simulator. Carrier transport across the p-$Cu_2O$/n-$In_2O_3$ broken-gap heterojunction occurs by ballistic transport. The junction has linear I-V characteristics with a resistance much lower than conventional tunnel junctions even when $Cu_2O$ is only moderately ($2\times10^{17}$ $cm^{-3}$) doped. Junction properties were improved further by inserting buffer layers between the tunnel junction and the absorbers in both top and the bottom cells. Specifically, a NiO buffer layer was inserted under CGS, the absorber in the top solar cell, and graded ZnO/$In_2O_3$ was inserted above the CIS, the absorber in the bottom solar cell. These buffer layers minimized the energy barriers between the tunnel junction and the solar cells. With an optimized tunnel junction structure, the efficiency of a CGS/CIS tandem PV cells was 24.1%. Importantly, there are no significant losses in efficiency due to the presence of the p-$Cu_2O$/n-$In_2O_3$ tunnel

junctions as compared to the total efficiency of separate bottom and top solar cells. Thus, a p-$Cu_2O$/n-$In_2O_3$ broken-gap tunnel junction is an attractive approach for connecting solar cells in polycrystalline CIGS-based multi-junction PV devices.

**References**


[1] W. Shockley, H. J. Queisser, J. Appl. Phys., 32 (1961) 510-519.

[2] M. A. Green, Prog. Photovolt.: Res. Appl., 9 (2001) 123-135.

[3] M. A. Green, Prog. Photovolt.: Res. Appl., 20 (2012) 12–20.

[4] H. Cotal, C. Fetzer, J. Boisvert, G. Kinsey, R. King, P. Hebert, H. Yoon, N. Karam, Energy & Environmental Sci., 2 (2009) 174-192.

[5] S. M. Sze, K. K. Ng, Physics of Semiconductor Devices 3rd ed., Wiley, New York, 2007.

[6] T. I. Kamins, J. Manoliu, R. N. Tucker, J. Appl. Phys., 43 (1972) 83-91.

[7] K. Mochizuki, T. Nakamura, Appl. Phys. Lett., 65 (1994) 2066-2068.

[8] Y. Zhao, C. Persson, S. Lany, A. Zunger, Appl. Phys. Lett., 85 (2004) 5860-5862.

[9] S. B. Zhang, S. Wei, A. Zunger, J. Appl. Phys., 83 (1998) 3192-3196.

[10] D. L. Young, J. Abushama, R. Noufi, X. Li, J. Keane, T. A. Gessert, J. S. Ward, M. Contreras , M. Symko-Davies, T. J. Coutts, Proceedings of 29th IEEE Photovolt. Spec. Conf., 2002, 608-611.

[11] M. Symko-Davies, Proceedings of 31th IEEE Photovolt. Spec. Conf., 2005, 410-413.

[12] P. J. Rostan, J. Mattheis, G. Bilger, U. Rau, J. H. Werner, Thin Solid Films, 480-481 (2005) 67-70.

[13] D. J. L. Brémaud, Investigation and development of CIGS solar cells on flexible substrates and with alternative electrical back contacts, Zurich, 2009.

[14] T. Nakada, Y. Hirabayashi, T. Tokado, D. Ohmori, T. Mise, Sol. Cells, 77 (2004) 739–747.

[15] H. Sakaki, L. L. Chang, R. Ludeke, C. Chang, G. A. Sai-Halasz, L. Esaki, Appl. Phys. Lett., 31 (1977) 211-213.

[16] G. J. Gualtieri, G. P. Schwartz, R. G. Nuzzo, R. J. Malik, J. F. Walker, J. Appl. Phys., 61 (1987) 5337-5341.

[17] M. P. Mikhilova, A. N. Titkov, Semicond. Sci. Technol., 9 (1994) 1279–1295.

[18] M. P. Mikhailova, K. D. Moiseev, Y. P. Yakovlev, Semicond. Sci. Technol., 19 (2004) R109–R128.

[19] A. K. Srivastava, J. L. Zyskind, R. M. Lum, B. V. Dutt, J. K. Klingert, Appl. Phys. Lett., 49 (1986) 41-43.

[20] D. A. Collins, E. T. Yu, Y. Rajakarunanayake, J. R. Söderström, D. Z.-Y. Ting, D. H. Chow, T. C. McGill, Appl. Phys. Lett., 57 (1990) 683-685.

[21] B. M. Borg, M. Ek, K. A. Dick, B. Ganjipour, A. W. Dey, C. Thelander, L. Wernersson, Appl. Phys. Lett., 99 (2011) 213101.

[22] K. Vizbaras, M. Törpe, S. Arafin, M. Amann, Semicond. Sci. Technol., 26 (2011) 075021.

[23] K. L Chopra, S. Major, D. K. Pandya, Thin Solid Films, 102 (1983) 1-46.

[24] T. Minami, MRS Bulletin, 25 (2000) 38-44.

[25] C. G. Granqvis, Sol. Energy Mater. Sol. Cells, 91 (2007) 1529–1598.

[26] J. Robertson, S. J. Clark, Phys. Rev. B, 83 (2011) 075205.

[27] A. Zunger, Appl. Phys. Lett., 83 (2003) 57-59.

[28] H. Tanaka, T. Shimakawa, T. Miyata, H. Sato, T. Minami, Thin Solid Films, 469-470 (2004) 80-85.

[29] J. Deuermeier, J. Gassmann, J. Brötz, A. Klein, J. Appl. Phys., 109 (2011) 113704.

[30] A. Facchetti, T. J. Marks. Transparent Electronics: From Synthesis to Applications, Wiley, New York, 2010.

[31] ISE DESSIS Manual Release: 9.5, Synopsys, Mountain View, 2004.

[32] G. Hanna, A. Jasenek, U. Rau, H. W. Schock, Thin Solid Films, 387 (2001) 71-73.

[33] V. Nadenau, U. Rau, A. Jasenek, H. W. Schock, J. Appl. Phys., 87 (2000) 584-593.

[34] S. H. Song, K. Nagaich, E. S. Aydil, R. Feist, R. Haley, S. A. Campbell, Proceedings of 35th IEEE Photovolt. Spec. Conf., 2010, 002488 - 002492.

[35] D. L. Young, Y. J. Keane, A. Duda, J. A. M. AbuShama, C. L. Perkins, M. Romero, R. Noufi , Prog. Photovolt.: Res. Appl., 11 (2003) 535–541.

[36] J. Song, S. S. Li, L. Chen, R. Noufi, T. J. Anderson, O. D. Crisalle, Proceedings of 4th World Conf. on Photovolt. Energy Conversion, 2006, 534–537.

[37] R. L. Anderson, Sol. State Elec., 5 (1962) 341-351.

[38] S. O. Koswatta, S. J. Koester, W. Haensch, IEEE Trans. on Electron Devices, 57 (2010) 3222-3230.

[39] J. Knoch, J. Appenzeller, IEEE Electron Device Lett., 31 (2010) 305-307.

[40] H. Kroemer, W. Chien, J. S. Harris, D. D. Edwall, Appl. Phys. Lett., 36 (1980) 295-297.

[41] T. Tomizawa, Numerical simulation of submicron semiconductor devices, Artech house, Boston, 1993.

[42] A. G. Zhilich, J. Halpern, B. R. Zakharchenya, Phys. Rev., 188 (1969) 1294–1302.

[43] I. Hamberg, C. G. Granqvist, J. Appl. Phys., 60 (1986) R123-R159.

[44] M. Hermle, G. Létay, S. P. Philipps, A. W. Bett, Prog. Photovolt.: Res. Appl., 16 (2008) 409-418.

[45] A. Martí, G. L. Araújo, Sol. Energy Mater. Sol. Cells, 43 (1996) 203–222.

[46] B. J. Stanbery, Critical Reviews in Sol. State and Mater. Sci., 27 (2002) 73-117.

[47] A. Mallouky, J. C. Bernede, Thin Solid Films, 158 (1988) 285-498.

[48] M. Bär, S. Nishiwaki, L. Weinhardt, S. Pookpanratana, W. N. Shafarman, C. Heske, Appl. Phys. Lett., 93 (2008) 042110.

[49] A. O. Pudov, A. Kanevce, H. A. Al-Thani, J. R. Sites, F. S. Hasoon, J. Appl. Phys., 97 (2005) 064901.

# Chapter 6

## Conclusion and Future Work

### 6.1. Summary.

Even though the maximum efficiency of CIGS solar cells is higher than any other thin film solar cells, the average efficacies of mass production CIGS solar cell are low. We examined the low efficiency CIGS solar cell on stainless steel substrates supplied by Dow Chemical. In addition to the recombination currents in junction depletion regions, F-N tunneling currents increased the dark current at low bias and decreased the shunt resistances of CIGS solar cells at not only dark but also illumination. The low shunt resistance degraded the efficiencies due to low fill factors. For trap characterization, we used thermal admittance spectroscopy and performed the analytical modeling for it. Since the density of minority carriers should be lower than the density of majority carriers, the maximum possible ratio of capacitance difference to high frequency capacitance due to minority traps is 0.12. If the ratio is lower than 0.12 both majority and minority traps are possible however above 0.12 only the majority traps are possible. Analytical model results were well matched with numerical simulation results. The activation energies of traps were directly affected on the shunt resistances than the trap densities. The activation energy of trap is a tunneling barrier energy of traps so that the high activation energy reduces the F-N tunneling currents. And, low activation rate due to high activation energy

decrease the total free carrier density and electric field near in depletion region such as junction interface and grain boundaries thus F-N tunneling current is reduced.

Reliable solar cell is high required for an affordable renewable energy source. Air anneals decreased the efficiency monotonically from 7.74% to 5.18% after a 150 $^{o}$C, 1000 hour anneal with increasing anneal temperature. The increase of F-N tunneling current and series resistance degraded the efficiencies of solar cells. New majority deep traps were generated by air anneal. The activation energies of new traps were 0.251 eV ~ 0.288 eV at 125 $^{o}$C and 150 $^{o}$C anneal. The deep trap densities increased $6.44\times10^{15}$ $cm^{-3}$ to $1.11\times10^{16}$ $cm^{-3}$ after 150 $^{o}$C anneal. Air anneal used to increase the efficiency by increasing majority career concentrations. In our work, however, air anneal decreased carrier density from $6.66\times10^{15}$ $cm^{-3}$ to 0.76 ~ $2.67\times10^{15}$ $cm^{-3}$. Minority traps were also generated by air anneals and compensated the majority careers and traps. The Minority carriers are presumed the interstitial Cu defect ($Cu_i$) because of minority type defect and mobile characteristics. Metastability was observed in the CIGS solar cells after 150 $^{o}$C anneal and the density of metastable carriers was matched with the minority carrier density. Since the oxygen atoms are more likely to passivate $V_{Se}$ defects at the grain boundaries by oxidation, mobile $Cu_i$ model is well explained the metastability in CIGS solar cell by oxidation.

One of the significant problems in CIGS solar cells is that the maximum efficiency is achieved at Ga composition, x=0.3 and the efficiencies degrade in the wide band gaps. A misfit model between the layers in a CIGS solar cell can explain the general dependence of the behavior of these devices with Ga composition. The misfits of 35.08$^{o}$

rotated (220/204) CIGS to r-plane (102) $MoSe_2$ layers are 1% ~-4% while the misfits of (112) CIGS to (001) $MoSe_2$ are 20.2% ~20.7%. High misfits generate the high density of dislocations thus film qualities and the efficiencies can be worse. Thus, the (220) oriented CIGS films can be the high efficiencies. The lattice constant of 35.08$^o$ rotated (220/204) in short distance is matched with r-plane (102) $MoSe_2$ at x=0.35 around. This result explains well the Ga composition of high efficiency CIGS solar cells. The treading dislocations and bulk trap densities of CIGS films were calculated from the dislocation spacing and critical thickness calculation due to Ga composition. Numerical simulation showed that the maxim efficiency of CIGS solar cells was x=0.35 with the misfit bulk trap model and the efficiencies decreased at wide band gap CIGS films. Misfit between CIGS and CdS generated the dislocations in CdS layer as the interface traps. The S vacancy ($V_S$) defects are the most possible donor-like defects. The activation energies of $V_S$ defects is 0.2 ~ 0.25 eV from the conduction band edge. The thermionic emission of holes from the valence band of CIGS to the interface traps limit on the open circuit voltage ($V_{OC}$) at above x=0.55 in our model because the activation energies of $V_s$ are fixed from the conduction band edged of CdS. The interface misfit model was well explained the VOC saturation at the wide band gap CIGS. Numerical simulation results with bulk and interface misfit trap models were well matched with the experimental results of CIGS solar cells due to Ga composition and explained the behavior of CIGS solar cells well.

To overcome the difficulties of tunnel junction formation in poly crystalline multi junction solar cells, we suggested a metal oxide broken-gap p-n heterojunction and

investigated its characteristics using numerical simulation. Broke-gap junction is the conduction band edge of the n-type material is equal to or lower in energy than the valence band edge of the p-type material thus the current can flow in both direction due to energy band banding. P-type $Cu_2O$ and n-type $In_2O_3$ broken-gap heterojunction is effective with the CIGS tandem solar cells. Since the balance between drift-diffusion current at near the junction interface inhibits the current flow when the majority carriers are accumulated, ballistic transport mechanism is effective to explain the current mechanisms due to energy band bending. The junction has linear I-V characteristics with moderate carrier concentration ($2\times10^{17}$ $cm^{-3}$) and the resistance is lower than GaAs tunnel junction. To minimize the performance degradation due to broken band-gap junction, buffer layers are suggested - NiO layers at the CGS/$Cu_2O$ interface and $Cu_2O$ and graded ZnO/$In_2O_3$ at the $In_2O_3$/ZnO interface. The efficiency of a CGS/CIS tandem PV cells was 24.1% with both buffer layers. And no significant degradations are expected due to the broken gap junction. A p-$Cu_2O$/n-$In_2O_3$ broken-gap tunnel junction is an attractive approach for connecting solar cells in polycrystalline CIGS-based multi-junction PV devices.

**6.2. Future works.**

In this work, we studied the degradation mechanism of CIGS solar cells and suggested new methods for high efficiency tandem CIGS solar cells. Most of all, the defect model due to the lattice mismatch between layers in CIGS solar cells is well explained the long mystery in the performance of wide band gap CIGS solar cell. Even

though it is well known that the residual stress in CIGS films performs an important role in the performance of thin film polycrystalline CIGS solar cells, it is hardly studied regarding heteroepitaxy and residual stress between layers in CIGS solar cells until now. Especially, the importance of $MoSe_2$ layers is generally ignored except back contact resistance because $MoSe_2$ layers are grown *in situ* during CIGS deposition. Thus, it is highly required to systematic experimental study and analysis for heteroepitaxy and dislocations between layers in CIGS solar cells. Additionally, the defects can exist not only in CIGS films but also in other layers such as CdS buffer layer however most studies assumed that all defects exist inside absorber layer and ignored the possibility due to other layers. Since it is difficult to analyze and distinguish interface defects, it should be carefully analyzed the causes and characteristics of interface defects.

Misfit model can apply numerous polycrystalline solar cells such as CdTe and CZTS. Based on this modeling method, we can design the combination of materials for high efficiency solar cells and expect to improve solar cells performance.

## Bibliography

D. Abou-Ras, G. Kostorz, A. Romeo, D. Rudmann, A.N. Tiwari, Thin Solid Films 480–481 (2005) 118– 123.

T. Ameri, G. Dennler, C. Lungenschmied, C. J. Brabec, Energ. Environ. Sci. 2 (2009) 347–363.

R. L. Anderson, Sol. State Elec., 5 (1962) 341-351.

A. Banerjee, T. Su, D. Beglau, G. Pietka, F. S. Liu, S. Almutawalli, J. Yang, S. Guha, IEEE J. Photovolt. 2 (2011), 99-103.

BBC, http://www.bbc.co.uk/news/business-16611040.

B. M. Borg, M. Ek, K. A. Dick, B. Ganjipour, A. W. Dey, C. Thelander, and L. Wernersson, Appl. Phys. Lett., 99 (2011) 213101.

K. Branker, M.J.M. Pathak, J.M. Pearce, Renew. Sust. Energ. Rev. 15 (2011) 4470–4482.

K. Brankera, M.J.M. Pathaka, J.M. Pearcea, Renew. Sust. Energ. Rev. 15 (2011) 4470–4482.

D. J. L. Brémaud, Investigation and development of CIGS solar cells on flexible substrates and with alternative electrical back contacts, Zurich, 2009.

H.-G. Brühl, H. Neumann, G. Kühn, Solid State Commun. 34 (1980) 225-227.

R. Caballero, S. Siebentritt, K. Sakurai, C.A. Kaufmann, H.W. Schock, M.Ch. Lux-Steiner, Thin Solid Films, 515 (2007) 5862–5866.

D. Cahen, R. Noufi, Appl. Phys. Lett., 54 (1989) 558-560.

S. Chaisitsak, A. Yamada, M. Konagai, Jpn. J. Appl. Phys. 41 (2002) 507.

R. Chakrabarti, B. Maiti, S. Chaudhuri, A.K. Pal, Sol. Energy Mater. Sol. Cells, 43 (1996), 237-247.

L. Chernyak, K. Gartsman, D. Cahen, O. M. Stafsudd, J. Phys. Chem. Solids 56 (1995) 1165-I 191.

K. L. Chopra, P. D. Paulson, V. Dutta, Prog. Photovolt.: Res. Appl. 12 (2004) 69–92.

K. L. Chopra, P. D. Paulson, V. Dutta, Prog. Photovolt.: Res. Appl. 12 (2004) 69–92.

D. A. Collins, E. T. Yu, Y. Rajakarunanayake, J. R. Söderström, D. Z.-Y. Ting, D. H. Chow, T. C. McGill, Appl. Phys. Lett., 57 (1990) 683-685.

M. A. Contreras, L. M. Mansfield, B. Egaas, J. Li, M. Romero, R. Noufi, E. Rudiger-Voigt and W. Mannstadt, Prog. Photovolt.: Res. Appl. 20 (2012) 843–850.

M. A. Contreras, M. J. Romero, B. To, F. Hasoon, R. Noufi, S.Ward, K.Ramanathan, Thin Solid Films 403 –404 (2002) 204–211.

M. A. Contreras, K. Ramanathan, J. AbuShama, F. Hasoon, D. L. Young, B. Egaas, R. Noufi, Prog. Photovolt.: Res. Appl. 13 (2005) 209–216.

M. A. Contreras, L. M. Mansfield, B. Egaas, J. Li, M. Romero, R. Noufi, E. Rudiger-Voigt, W. Mannstadt, Prog. Photovolt.: Res. Appl. 20 (2012) 843–850.

M. A. Contreras, M. Romero, D. Young, Conference Record, 3rd World Conference on Photovoltaic Energy Conversion, Osaka, May 2003, 2864.

M. A. Contreras, B. Egaas, D. King, A. Swartzlander, T. Dullweber, Thin Solid Films 361-362 (2000) 167-171.

M. A. Contreras, L. M. Mansfield, B. Egaas, J. Li, M. Romero, R. Noufi, E. Rudiger-Voigt, W. Mannstadt, Conference Record, 37th IEEE Photovolt. Spec. Conf., Seattle, June 2011; 000026 – 000031.

H. Cotal, C. Fetzer, J. Boisvert, G. Kinsey, R. King, P. Hebert, H. Yoon, N. Karam, Energy & Environmental Sci., 2 (2009) 174-192.

J. Deuermeier, J. Gassmann, J. Brötz, A. Klein, J. Appl. Phys., 109 (2011) 113704.

J. Dietrich, D. Abou-Ras, T. Rissom, T. Unold, H.-W. Schock, C. Boit, IEEE J. Photovolt., 2 (2012) 364-370.

B. Dimmler, M. Powalla, H. W. Schock, Prog. Photovolt.: Res. Appl. 10 (2002) 149–157

T. Dullweber, O. Lundberg, J. Malmström, M. Bodegård, L. Stolt, U. Rau, H.W. Schock, J. H. Werner, Thin Solid Films 387 (2001) 11-13.

P. R. Ehrlich, P. M. Kareiva, Gretchen C. Daily, Securing natural capital and expanding equity to rescale civilization, Nature, 468 (2012) 68-73.

EIA, History of energy consumption history in US, 2010.

EIA, Annual energy outlook 2012, 2012.

EIA, Average price of photovoltaic cells and modules, 2002-2011.

T. Eisenbarth, T. Unold, R. Caballero, C.A. Kaufmann, D. Abou-Ras, H.-W. Schock, Thin Solid Films 517 (2009) 2244–2247.

S. H. El-Mahalawy, B. L. Evans, J. Appl. Cryst., 9 (1976), 403-406.

A. Facchetti, T. J. Marks. Transparent Electronics: From Synthesis to Applications, Wiley, New York, 2010.

Federal Ministry for the Environment, Nature Conservation and Nuclear Safety, http://www.bmu.de/english/nuclear_safety/response_to_fukushima/questions_and_answers/doc/49010.php, 2012.

B. Fernandez, S.M. Wasim, Phys. Stat. Sol. (a), 122 (1990) 235–242.

First Solar Annual Report, Phoenix, 2011.

First Solar First Quarter Financial Report, Phoenix, 2013.

R. Fouquet, P. J.G. Pearson, Energy Policy 50 (2012) 1–7

L. B. Freund, Mater. Res. Soc. Bull. 17 (1992) 52.

L. B. Freund, S. Suresh, Thin Film Materials Stress, Defect Formation and Surface Evolution, Cambridge University Press, New York, 2003.

A. M. Gabor, J. R. Tuttle, D. S. Albin, M. A. Contreras, R. Noufi, A. M. Hermann, Appl. Phys. Lett. 65(1994), 198-200.

K. Gartsman, L. Chernyak, V. Lyahovitskaya, D. Cahen, V. Didik, V. Kozlovsky, R. Malkovich, E. Skoryatina, V. Usacheva, J. Appl. Phys. 82 (1997) 4282-4285.

M. Gloeckler, J.R. Sites, Thin Solid Films 480–481 (2005) 241– 245.

C. G. Granqvis, Sol. Energy Mater. Sol. Cells, 91 (2007) 1529–1598.

M. A. Green, Prog. Photovolt.: Res. Appl. 9 (2001) 123-135.

M. A. Green, K. Emery, Y. Hishikawa, W. Warta, E. D. Dunlop, Prog. Photovolt.: Res. Appl., 20 (2012) 606–614.

M. A. Green, K. Emery, Y. Hishikawa, W. Warta, E. D. Dunlop, Prog. Photovolt.: Res. Appl., 21(2013) 1–11

M. A. Green, Prog. Photovolt.: Res. Appl., 9 (2001) 123-135.

M. A. Green, Prog. Photovolt.: Res. Appl., 20 (2012) 12–20.

C. Grill, G. Bastide, G. Sagnes, M. Rouzeyre, J. Appl. Phys., 50 (1979) 1375-1380.

G. J. Gualtieri, G. P. Schwartz, R. G. Nuzzo, R. J. Malik, J. F. Walker, J. Appl. Phys., 61 (1987) 5337-5341.

M. Hafemeister, S. Siebentritt, J. Albert, M. Ch. Lux-Steiner, S. Sadewasser, Phys. Rev. Lett. 104 (2010) 196602.

I. Hamberg, C. G. Granqvist, J. Appl. Phys., 60 (1986) R123-R159.

G. Hanna, A. Jasenek, U. Rau, H. W. Schock, Thin Solid Films, 387 (2001) 71-73.

S. S. Hegedus, W. N. Shafarman, Prog. Photovolt.: Res. Appl. 12 (2004) 155–176.

S. Hegedus, Prog. Photovolt.: Res. Appl. 14 (2006) 393–411.

R. Herberholz, M. Igalson, H. W. Schock, J. Appl. Phys. 83 (1998) 318-325.

R. Herberholz, H.W. Schock, U. Rau, J.H.Werner, T. Haalboom, T. Godecke, F. Ernst, C. Bleilharz, K.W. Benz, D. Cahen, Proceedings of 26th IEEE Photovolt. Spec. Conf., 1997, Anaheim, 323-326.

R. Herberholz, V. Nadenau, U. Rühle, C. Köble, H.W. Schock, B. Dimmler, Sol. Energy Mater. Sol. Cells 49 (1997) 227-237.

R. Herberholz, M. Igalson, H. W. Schock, J. Appl. Phys., 83 (1998) 318-325.

M. Hermle, G. Létay, S. P. Philipps, A. W. Bett, Prog. Photovolt.: Res. Appl., 16 (2008) 409-418.

G. A. M. Hurkx, D. B. M. Klaassen, M. P. G. Knuvers, IEEE Trans. Electron Devices, 39 (1992) 331-338.

M. Hussein, G. Lleti, G. Sagnes, G. Bastide, M. Rouzeyre, J. Appl. Phys., 52 (1981) 261-268.

IEA, Key energy world statistics, Paris, 2012.

IEC, standard IEC 61215.

IEC, standard IEC 61646.

M. Igalson, A. Urbaniak, M. Edoff, Thin Solid Films 517 (2009) 2153–2157.

IPCC, Climate Change 2007: Synthesis Report, 2007.

IPCC, Climate Change 2007: Working group II technical summary, 2007.

IPCC, Renewable Energy Sources and Climate Change Mitigation Special Report of the Intergovernmental Panel on Climate Change, Cambridge university press, New York,2012

IPCC, Renewable Energy Sources and Climate Change Mitigation Special Report of the Intergovernmental Panel on Climate Change, Cambridge university press, New York,2012

P. Jackson, D. Hariskos, E. Lotter, S. Paetel, R. Wuerz, R. Menner, W. Wischmann, M. Powalla, Prog. Photovolt.: Res. Appl. 19 (2011) 894-897.

C.-S. Jiang, M. A. Contreras, I. Repins, H. R. Moutinho, Y. Yan, M. J. Romero, L. M. Mansfield, R. Noufi, M. M. Al-Jassim, Appl. Phys. Lett. 101 (2012) 033903.

D. C. Jordan, S. R. Kurtz, Prog. Photovolt.: Res. Appl. 21 (2013) 12–29.

T. I. Kamins, J. Manoliu, R. N. Tucker, J. Appl. Phys., 43 (1972) 83-91.

L. L. Kazmerski, O. Jamjoum, P. J. Ireland, S. K. Deb, R. A. Mickelsen, W. Chen, J. Vac. Scl. Technol., 19 (1981) 467-471.

L. L. Kazmerski, O. Jamjoum, J. F. Wager, P. J. Ireland, K. J. Bachmann, J. Vac. Scl. Technol. A, 1 (1983) 668-669.

S. Kijima, T. Nakada, Appl. Phys. Express 1 (2008) 075002.

J. Knoch, J. Appenzeller, IEEE Electron Device Lett., 31 (2010) 305-307.

S. R. Kodigala, $CuIn_{1-x}Ga_xSe_2$ Based Thin Film Solar Cells - Thin Films and Nanostructures Volume 35, Academic Press, New York, 2010.

S. R. Kodigala, Thin films and nanostructures $Cu(In_{1-x}Ga_x)Se_2$ based thin film solar cells Vol. 35, (2010).

S. O. Koswatta, S. J. Koester, W. Haensch, IEEE Trans. on Electron Devices, 57 (2010) 3222-3230.

H. Kroemer, W. Chien, J. S. Harris, D. D. Edwall, Appl. Phys. Lett., 36 (1980) 295-297.

L. Kronik, D. Cahen, H. W. Schock, Adv. Mater. 10 (1998) 33-36.

D. V. Lang, J. Appl. Phys., 45 (1974) 3023-3032.

S. Lany, A. Zunger, J. Appl. Phys. 100 (2006) 113725.

S. Lany, A. Zunger, J. Appl. Phys. 100 (2006) 113725.

C. H. Lei, A. A. Rockett, I. M. Robertson, N. Papathanasiou, S. Siebentritt, J. Appl. Phys., 100 (2006) 114915.

D. L. Losee, J. Appl. Phys., 46 (1975) 2204-2214.

A. Luque, Handbook of Photovoltaic Science and Engineering, John Wiley & Sons, West Sussex, England, 2003.

M. Bär, S. Nishiwaki, L. Weinhardt, S. Pookpanratana, W. N. Shafarman, C. Heske, Appl. Phys. Lett., 93 (2008) 042110.

O. Madelung, Semiconductors: Data handbook 3rd ed., Springer, Berlin, 2004.

A. Mallouky, J. C. Bernede, Thin Solid Films, 158 (1988) 285-498.

S. Marsillac, S. Don, R. Rocheleau, E. Miller, Sol. Energy Mater. Sol. Cells 82 (2004) 45.

A. Martí, G. L. Araújo, Sol. Energy Mater. Sol. Cells, 43 (1996) 203–222.

R. J. Matson, O. Jamjoum, A.D. Buonaquisti, P. E. Russell, L. L. Kazmerski, P. Sheldon, R. K. Ahrenkiel, Solar Cells, 11 (1984) 301-305.

J. W. Matthews, J. Vac. Sci. Technol., 12 (1975) 126-133.

J. W. Matthews, A. E. Blakeslee, J. Cryst. Growth, 27 (1974) 118-125.

T. J. McMahon, Prog. Photovolt.: Res. Appl. 12 (2004) 235–248.

V. Mertens, J, Parisi, J. Appl. Phys., 101 (2007) 104507.

M. A. Meyers, H.Jarmakani, E.M.Bringa, B.A.Remington. Dislocations in Solids, vol. 15, (2009) chap. 89.

R. A. Mickelsen, W. S. Chen, Proceedings of 15th IEEE Photovolt. Spec. Conf., 1981, 800 - 804.

M. P. Mikhailova, K. D. Moiseev, Y. P. Yakovlev, Semicond. Sci. Technol., 19 (2004) R109–R128.

M. P. Mikhilova and A. N. Titkov, Semicond. Sci. Technol., 9 (1994) 1279–1295.

T. Minami, MRS Bulletin, 25 (2000) 38-44.

K. Mochizuki, T. Nakamura, Appl. Phys. Lett., 65 (1994) 2066-2068.

V. Nadenau, U. Rau, A. Jasenek, H. W. Schock, J. Appl. Phys. 87 (2000) 584-593.

V. Nadenau, D. Hariskos, H.-W. Schock, M. Krejci, F.-J. Haug, A. N. Tiwari, H. Zogg, G. Kostorz, J. Appl. Phys., 85 (1999) 534-542.

V. Nadenau, U. Rau, A. Jasenek, H. W. Schock, J. Appl. Phys., 87 (2000) 584-593.

T. Nakada, Y. Hirabayashi, T. Tokado, D. Ohmori, T. Mise, Sol. Cells, 77 (2004) 739–747.

S. Nishiwaki, N. Kohara, T. Negami, T. Wada, Jpn. J. Appl. Phys. 37 (1998) L71.

R. Noufi, P. Souza, C. Osterwald, Solar Cells, 15 (1985) 87 - 91

NREL, International energy outlook, Golden, 2011.

NREL, Best research-cell efficiency record chart, Golden, 2013.

K. Orgassa, H.W. Schock, J.H. Werner, Thin Solid Films 431-432 (2003) 387–391.

J. Oualid, J. L. Granier, D. Sarti, J. Phys. C: Solid State Phys. 12 (1979) 5323-5331.

P. D. Paulson, R. W. Birkmire, W. N. Shafarmana J. Appl. Phys., 94 (2003) 879-888.

R. People, J. C. Bean, Appl. Phys. Lett. 49 (1986), 229.

C. Persson, A. Zunger, Phys. Rev. Lett. 91 (2003) 196602.

A. O. Pudov, A. Kanevce, H. A. Al-Thani, J. R. Sites, F. S. Hasoon, J. Appl. Phys., 97 (2005) 064901.

U. Rau, K. Taretto, S. Siebentritt, Appl. Phys. A 96 (2009) 221–234.

U. Rau, D. Braunger, R. Herberholz, H. W. Schock, J.-F. Guillemoles, L. Kronik, D. Cahen, J. Appl. Phys., 86 (1999) 497-505.

U. Rau, H.W. Schock, Appl. Phys. A 69 (1999) 131–147.

U. Rau, K. Taretto, S. Siebentritt, Appl. Phys. A 96 (2009) 221–234.

REN21, Renewables 2012 Global status report, 2012.

I. Repins, M. A. Contreras, B. Egaas, C. DeHart, J. Scharf, C. L. Perkins, B. To, R. Noufi, Prog. Photovolt: Res. Appl.16 (2008) 235–23.

J. Robertson, S. J. Clark, Phys. Rev. B, 83 (2011) 075205.

A. Romeo, M. Terheggen, D. Abou-Ras, D. L. Bätzner1, F.-J. Haug, M. Kälin, D. Rudmann, A. N. Tiwari, Prog. Photovolt.: Res. Appl.12 (2004) 93–111.

P. J. Rostan, J. Mattheis, G. Bilger, U. Rau, J. H. Werner, Thin Solid Films, 480-481 (2005) 67-70.

P. E. Russell, O. Jamjoum, R. K. Ahrenkiel, L. L. Kazmerski, R. A. Mickelsen, W. S. Chen, Appl. Phys. Lett., 40 (1982) 995-997.

C.-T. Sah, R. N. Noyce, W. Shockley, Proc. the IRE, 45 (1957) 1228 – 1243.

T. Saitoh, H. Hashigami, S. Rein, S. Glunz, Prog. Photovolt.: Res. Appl. 8 (2000) 426-436

H. Sakaki, L. L. Chang, R. Ludeke, C. Chang, G. A. Sai-Halasz, L. Esaki, Appl. Phys. Lett., 31 (1977) 211-213.

J. Santamaria, G. Gonzalez Diaz, E Iborra, I. Martil, and F. SanchezQuesada, J. Appl. Phys. 65 (1989) 3236-3241.

S.-i. Sato, H. Sai, T. Ohshima, M. Imaizumi, K. Shimazaki, M. Kondo, Prog. Photovolt: Res. Appl. 21 (2012).

R. Scheer, H. Schock, Chalcogenide Photovoltaics Physics, Technologies, and Thin Film Devices, Wiley-VCH, Weinheim, 2011.

S. M. Schleussner, T. Törndahl, M. Linnarsson, U. Zimmermann, T. Wätjen, M. Edoff, Prog. Photovolt.: Res. Appl. 20 (2012) 284–293.

D. K. Schroder, Semiconductor material and device characterization, John Wiley & Sons, Hoboken, Wiley, 2006.

O. E. Semonin, J. M. Luther, S. Choi, H. Chen, J. Gao, A. J. Nozik, Matthew C. Beard, Science 334 (2011) 1530-1533.

W. N. Shafarman, R. Klenk, B.E. McCandless, 25th IEEE Photovolt. Spec. Conf., May, 1996; Washington, D.C. 783.

W. N. Shafarman, R. Klenk, B. E. McCandless, J. Appl. Phys. 79 (1996) 7324-7328.

A. Shah, P. Torres, R. Tscharner, N. Wyrsch, H. Keppner, Science 30 (1999) 692-698.

D. H. Shin, Y. M. Shin, J. H. Kim, B. T. Ahn, K. H. Yoon, J. Electrochem. Soc., 159 (2012) B1-B5.

W. Shockley, H. J. Queisser, J. Appl. Phys., 32 (1961), 510-519.

S. Siebentritt, M. Igalson, C. Persson, S. Lany, Prog. Photovolt: Res. Appl. 18 (2010) 390–410

S. H. Song, K. Nagaich, E. S. Aydil, R. Feist, R. Haley, S. A. Campbell, Conference Record, 35th IEEE Photovol. Spec. Conf., Honolulu, June 2010; 002488 - 002492.

J. Song, S. S. Li, L. Chen, R. Noufi, T. J. Anderson, O. D. Crisalle, Proceedings of 4th World Conf. on Photovolt. Energy Conversion, 2006, pp. 534–537.

M. Souilah, A. Lafond, C. Guillot-Deudon, S. Harel, M. Evain, J. Solid State Chem., 183 (2010) 2274–2280.

A. K. Srivastava, J. L. Zyskind, R. M. Lum, B. V. Dutt, J. K. Klingert, Appl. Phys. Lett., 49 (1986) 41-43.

B. J. Stanbery, Critical Reviews in Sol. State and Mater. Sci., 27 (2002) 73-117.

R. Stangl, M.Kriegel, M. Schmidt, Conference Record, 4th World Conference on Photovoltaic Energy Conversion, Waikoloa, May 2006, 1350-1353.

R. M. Swanson, Science 324 (2009) 891-892.

M. Symko-Davies, Proceedings of 31th IEEE Photovolt. Spec. Conf., 2005, pp. 410-413.

ISE DESSIS Manual Release: 9.5, Synopsys, Mountain View, 2004.

S. M. Sze, Physics of semiconductor devices, John Wiley & Sons, Hoboken, 2007.

H. Tanaka, T. Shimakawa, T. Miyata, H. Sato, T. Minami, Thin Solid Films, 469-470 (2004) 80-85.

The National Diet of Japan, The official report of Executive summary The Fukushima Nuclear Accident Independent Investigation Commission exclusive summary, 2011.

T. Tomizawa, Numerical simulation of submicron semiconductor devices, Artech house, Boston, 1993.

A. Tonejc, S. Popovic, B. Grzeta-Plenkovic, J. Appl. Crystallogr. 13 (1980) 24.

M. Turcu, I. M. Kötschau, U. Rau, J. Appl. Phys., 91 (2002) 1391-1399.

Tüv, Basic understanding of IEC standard testing for photovoltaic panels, Peabody,.

UNFCC, Kyoto protocol to the united nations framework convention on climate change, 1998.

UNFCC, United nations framework convention on climate change, 1992.

J. H. Van Der Merwe, J. Appl. Phys. 34 (1963) 117-122.

K. Vizbaras, M. Törpe, S. Arafin, M. Amann, Semicond. Sci. Technol., 26 (2011) 075021.

T. Wada, N. Kohara, T. Negami, M. Nishitani, Jpn. J. Appl. Phys. 35 (1996) L1253.

T. Walter, R. Herberholz, C. Müller, H. W. Schock, J. Appl. Phys. 80 (1968) 4411–4420.

X Wang, L. Kurdgelashvili, J. Byrne, Allen Barnett, Renew. Sust. Energ. Rev. 15 (2011) 4248– 4254.

K. Wang, R. R. Reeber, Mat. Sci. Eng. R23 (1998) 101-137.

L. R. Weisberg, H. Schade, J. Appl. Phys. 39 (1968) 5149–5151.

R. M. White, IEEE Trans. Electron Devices, 14 (1967) 181-189.

M. Woodhouse, A. Goodrich, R. Margolis, T. James, R. Dhere, T. Gessert, T. Barnes, R. Eggert, D. Albin, “Perspectives on the pathways for cadmium telluride photovoltaic

module manufacturers to address expected increases in the price for tellurium", Sol. Energy Mater. Sol. Cells, (2012) in press.

R. W. G. Wyckoff, Crystal Structures, John Wiley and Sons, New York, 1963.

D. L. Young, J. Abushama, R. Noufi, X. Li, J. Keane, T. A. Gessert, J. S. Ward, M. Contreras , M. Symko-Davies, T. J. Coutts, Proceedings of 29th IEEE Photovolt. Spec. Conf., 2002, pp. 608-611.

D. L. Young, Y. J. Keane, A. Duda, J. A. M. AbuShama, C. L. Perkins, M. Romero, R. Noufi , Prog. Photovolt.: Res. Appl., 11 (2003) 535–541.

P. Zabierowski, M. Edoff, Thin Solid Films 480–481 (2005) 301– 306.

S. B. Zhang, S.-H. Wei, A. Zunger, Phys. Rev. B, 57 (1998) 9642-9656.

S. B. Zhang, S. Wei, A. Zunger, J. Appl. Phys., 83 (1998) 3192-3196.

Y. Zhao, C. Persson, S. Lany, A. Zunger, Appl. Phys. Lett., 85 (2004) 5860-5862.

A. G. Zhilich, J. Halpern, B. R. Zakharchenya, Phys. Rev., 188 (1969) 1294–1302.

Y. Zohta, Solid-State Electronics 16 (1973) 1029-1035.

Y. Zohta, J. Appl. Phys. 43 (1972) 1713–1716.

A. Zunger, S. B. Zhang, S.-H. Wei, Conference Record, 26th IEEE Photovolt. Spec. Conf., Anaheim, June 1997; 313-318.

A. Zunger, Appl. Phys. Lett., 83 (2003) 57-59.

**Appendix 1.**

A1.1. Majority traps

A1.1.1. Depletion width with majority traps in thermal equilibrium.

P-n junction should satisfy the charge neutrality in both regions. Charge neutrality and total depletion width ($W$) with majority traps are given by

$$N_D x_n = N_A x_p + N_T x_T = (N_A + N_T) x_p - N_T \lambda , \tag{A1}$$

and

$$W = x_n + x_p = \frac{N_D + N_A + N_T}{N_D} x_p - \frac{N_T}{N_D} \lambda \tag{A2}$$

where

$$x_p = x_T + \lambda , \tag{A3}$$

$$\Delta E_{TF} = E_T - E_F , \tag{A4}$$

and

$$\lambda = \sqrt{\frac{2\varepsilon_p}{qN_A} \Delta E_{TF}} , \tag{A5}$$

$N_{D,A}$, $x_{n,p}$, $N_T$, $E_T$ and $E_F$ are the dopant concentration in the n-type (subscript n) and p-type region (subscript p), the depletion width in n-type and p-type region, the carrier concentration of traps, the energy level of the trap and the Fermi level. $\lambda$ is the trap inactivated depletion width from the junction edge [1].

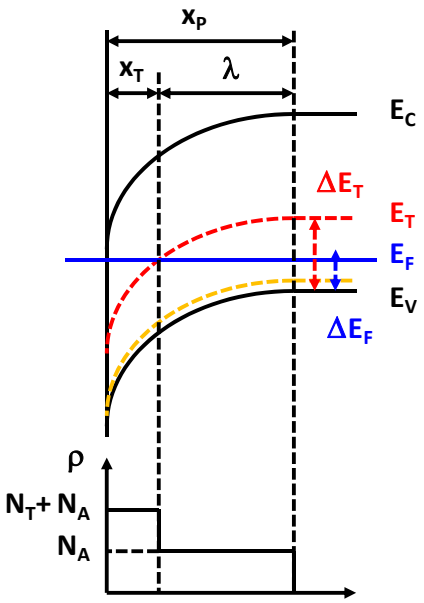


Figure A1.1. Schematic diagram of energy band diagram and charge density.

The built-in potential ($V_{bi}$) is

$$V_{bi} - V = \frac{q}{2\varepsilon_n} N_D x_n^2 + \frac{q}{2\varepsilon_p} N_A x_p^2 + \frac{q}{2\varepsilon_p} N_T \left(x_p - \lambda\right)^2 \qquad \text{(A6)}$$

where, $\varepsilon_{n,p}$ and $V$ are relative dielectric constant of n-type and p-type materials and applied bias.

Solving equation (A2) and (A6), the total depletion width ($W$) is

$$W = \frac{N_D + N_A + N_T}{N_D} \times \sqrt{\frac{2}{N_A + N_T}\left[\frac{\varepsilon_p \varepsilon_n N_D}{\varepsilon_p \left(N_A + N_T\right) + \varepsilon_n N_D}\right]\left[\frac{V_{bi} - V}{q} - \frac{N_T}{2}\left(\frac{N_T}{\varepsilon_n N_D} + \frac{1}{\varepsilon_p}\right)\lambda^2\right] + \left(\frac{N_T \lambda}{N_A + N_T}\right)^2} + \frac{N_T}{N_A + N_T}\lambda \qquad \text{(A7)}$$

If the diode is a one-sided abrupt junction ($N_D >> N_A + N_T$) then the depletion width is

$$W \approx x_p = \sqrt{\frac{2\varepsilon_p}{q(N_A + N_T)}(V_{bi} - V) - m(1-m)\lambda^2} + m\lambda\,, \tag{A8}$$

where

$$m = \frac{N_T}{N_A + N_T} \tag{A9}$$

[1].

A1.1.2. Junction capacitance with majority traps.

The charge difference in the p-n junction is

$$\Delta Q = qN_A\Delta x_p + qN_T(\omega)\Delta(x_p - \lambda). \tag{A10}$$

The voltage difference is

$$\Delta V = \frac{q}{\varepsilon_p}N_A x_p \Delta x_p + \frac{q}{\varepsilon_p}N_T(\omega)(x_p - \lambda)\Delta(x_p - \lambda). \tag{A11}$$

The junction capacitance ($C_{maj}$) is

$$C_{maj} = \frac{\Delta Q}{\Delta V} = \frac{qN_A\Delta x_p + qN_T(\omega)\Delta(x_p - \lambda)}{\frac{q}{\varepsilon_p}N_A x_p \Delta x_p + \frac{q}{\varepsilon_p}N_T(\omega)(x_p - \lambda)\Delta(x_p - \lambda)} \tag{A12}$$

$$= \frac{\varepsilon_p}{x_p - \lambda\dfrac{N_T(\omega)\dfrac{\Delta(x_p - \lambda)}{\Delta x_p}}{N_A + N_T(\omega)\dfrac{\Delta(x_p - \lambda)}{\Delta x_p}}} = \frac{\varepsilon_p}{x_p - \lambda\dfrac{N_T(\omega)}{N_A + N_T(\omega)}} \tag{A13}$$

where

$$\frac{\Delta\left(x_p-\lambda\right)}{\Delta x_p}=1 \tag{A14}$$

because $\lambda$ is constant.

$N_T(\omega)$ is

$$N_T\left(\omega\right)=\frac{N_T}{\frac{\omega}{\omega_0}+1}, \tag{A15}$$

where

$$\omega_0=\frac{2\pi}{\tau}=2\pi\sigma_{e,h}\upsilon_{th}N_{V,C}\exp\left(\frac{E_{V,C}-E_T}{kT}\right), \tag{A16}$$

$N_{C,V}$, $E_{C,V}$, k and T are the density of states and the energy band edges of the conduction (subscript $_C$) and valence band (subscript $_V$), and $\sigma_{n,p}$, $\nu_{th}$ are the capture cross-sections of electrons (n) and holes (p), the thermal velocity of carriers, Boltzmann's constant, and temperature, respectively. [2].

The junction capacitance at low frequency ($C_{maj\_lf}$) and high frequency ($C_{maj\_hf}$) are

$$C_{maj\_lf}=\frac{\varepsilon_p}{x_p-\lambda\frac{N_T}{N_A+N_T}}=\frac{\varepsilon_p}{\sqrt{\frac{2\varepsilon_p}{q\left(N_A+N_T\right)}\left(V_{bi}-V\right)-m\left(1-m\right)\lambda^2}}, \tag{A17}$$

and

$$C_{maj\_hf}=\frac{\varepsilon_p}{x_p}=\frac{\varepsilon_p}{\sqrt{\frac{2\varepsilon_p}{q\left(N_A+N_T\right)}\left(V_{bi}-V\right)-m\left(1-m\right)\lambda^2}+m\lambda}. \tag{A18}$$

The ratio of capacitance difference to high frequency capacitance is

$$\frac{C_{\min\_lf} - C_{\min\_hf}}{C_{\min\_hf}} = \frac{m\lambda}{\sqrt{\frac{2\varepsilon_p}{q(N_A + N_T)}(V_{bi} - V) - m(1-m)\lambda^2}} = \frac{m}{\sqrt{(1-m)}\sqrt{\frac{V_{bi} - V}{\Delta E_{TF}} - m}} \quad \text{(A19)}$$

The difference between equivalent depletion widths at high and low frequency is

$$\Delta W = \varepsilon_p \left( \frac{1}{C_{maj\_hf}} - \frac{1}{C_{maj\_lf}} \right) = \frac{N_T}{N_A + N_T} \lambda = \frac{N_T}{N_A + N_T} \sqrt{\frac{2\varepsilon_p}{qN_A} \Delta E_{TF}} \le \sqrt{\frac{2\varepsilon_p}{qN_A} \Delta E_{TF}} \,. \quad \text{(A20)}$$

A1.2. Minority traps

A1.2.1. Depletion width with minority traps in thermal equilibrium.

The P-n junction should satisfy the charge neutrality in both regions. With minority charges and a total depletion width ($W$),

$$N_D x_n = (N_A - N_T) x_p + N_T x_T = (N_A - N_T) x_p + N_T (x_P - \lambda) = N_A x_p - N_T \lambda, \quad \text{(A21)}$$

where

$$x_n = \frac{N_A - N_T}{N_D} x_p + \frac{N_T}{N_D} (x_P - \lambda) = \frac{N_A}{N_D} x_p - \frac{N_T}{N_D} \lambda, \quad \text{(A22)}$$

$$W = x_n + x_p = \frac{N_D + N_A}{N_D} x_p - \frac{N_T}{N_D} \lambda, \quad \text{(A23)}$$

and

$$\lambda = \sqrt{\frac{2\varepsilon_p}{q(N_A - N_T)} (\Delta E_{TF} - V)} \,. \quad \text{(A24)}$$

The built-in potential ($V_{bi}$) is

$$V_{bi} - V = \frac{q}{2\varepsilon_n} N_D x_n^2 + \frac{q}{2\varepsilon_p}\left(N_A - N_T\right)x_p^2 + \frac{q}{2\varepsilon_p} N_T\left(x_p - \lambda\right)^2 \tag{A25}$$

Solving equation (A23) and (A25), the total depletion width ($W$) is

$$W = \frac{N_D + N_A}{N_D}\sqrt{\frac{2}{qN_A}\left(\frac{\varepsilon_p\varepsilon_n N_D}{\varepsilon_p N_A + \varepsilon_n N_D}\right)\left(V_{bi} - V\right) - \lambda^2\frac{N_T}{N_A}\left(\frac{\varepsilon_p N_T + \varepsilon_n N_D}{\varepsilon_p N_A + \varepsilon_n N_D} - \frac{N_T}{N_A}\right)} + \frac{N_T}{N_A}\lambda\,. \tag{A26}$$

If $N_D >> N_A + N_T$,

$$W = \sqrt{\frac{2\varepsilon_p}{qN_A}\left(V_{bi} - V\right) - n\left(1-n\right)\lambda^2} + n\lambda \tag{A27}$$

where

$$n = \frac{N_T}{N_A}\,. \tag{A28}$$

A1.2.2. Junction capacitance with minority traps.

The charge difference is

$$\Delta Q = -qN_T(\omega)\Delta\left(x_p - \lambda\right) + qN_A\Delta x_p\,. \tag{A29}$$

The voltage difference is

$$\Delta V = \frac{q}{\varepsilon_p} N_A x_p \Delta x_p\,. \tag{A30}$$

The junction capacitance ($C_{min}$) is

$$C_{\min} = \frac{\Delta Q}{\Delta V} = \frac{-qN_T(\omega)\Delta\left(x_p - \lambda\right) + qN_A\Delta x}{\frac{q}{\varepsilon_p} N_A x_p \Delta x_p} = \frac{N_T(\omega)}{N_A}\frac{\varepsilon_p}{x_p}\left(\frac{x_p}{\lambda} - 1\right) + \frac{\varepsilon_p}{x_p}\,, \tag{A31}$$

since

$$\frac{\Delta\left(x_p-\lambda\right)}{\Delta x_p}=-\frac{x_p-\lambda}{\lambda}. \tag{A32}$$

The junction capacitance at low frequency ($C_{\min\_lf}$) and high frequency ($C_{\min\_hf}$) are

$$C_{\min\_lf}=\frac{N_T}{N_A}\varepsilon_p\left(\frac{1}{\lambda}-\frac{1}{x_p}\right)+\frac{\varepsilon_p}{x_p}=\frac{N_T}{N_A}\frac{\varepsilon_p}{\lambda}+\left(1-\frac{N_T}{N_A}\right)\frac{\varepsilon_p}{x_p}=n\frac{\varepsilon_p}{\lambda}+\left(1-n\right)\frac{\varepsilon_p}{x_p} \tag{A33}$$

and

$$C_{\min\_hf}=\frac{\varepsilon_P}{x_P}. \tag{A34}$$

The ratio of capacitance difference to high frequency capacitance is

$$\frac{C_{\min\_lf}-C_{\min\_hf}}{C_{\min\_hf}}=n\left(\frac{x_p}{\lambda}-1\right)=n\left[\sqrt{1-n}\sqrt{\frac{V_{bi}-V}{\Delta E_{TF}-V}-n}+n-1\right] \tag{A35}$$

and capacitance difference is

$$\Delta C_{\min}=C_{\min\_lf}-C_{\min\_hf}=n\varepsilon_p\left(\frac{1}{\lambda}-\frac{1}{x_p}\right). \tag{A36}$$

**Appendix 2.**

A2.1. Grid and device structure for simulation.

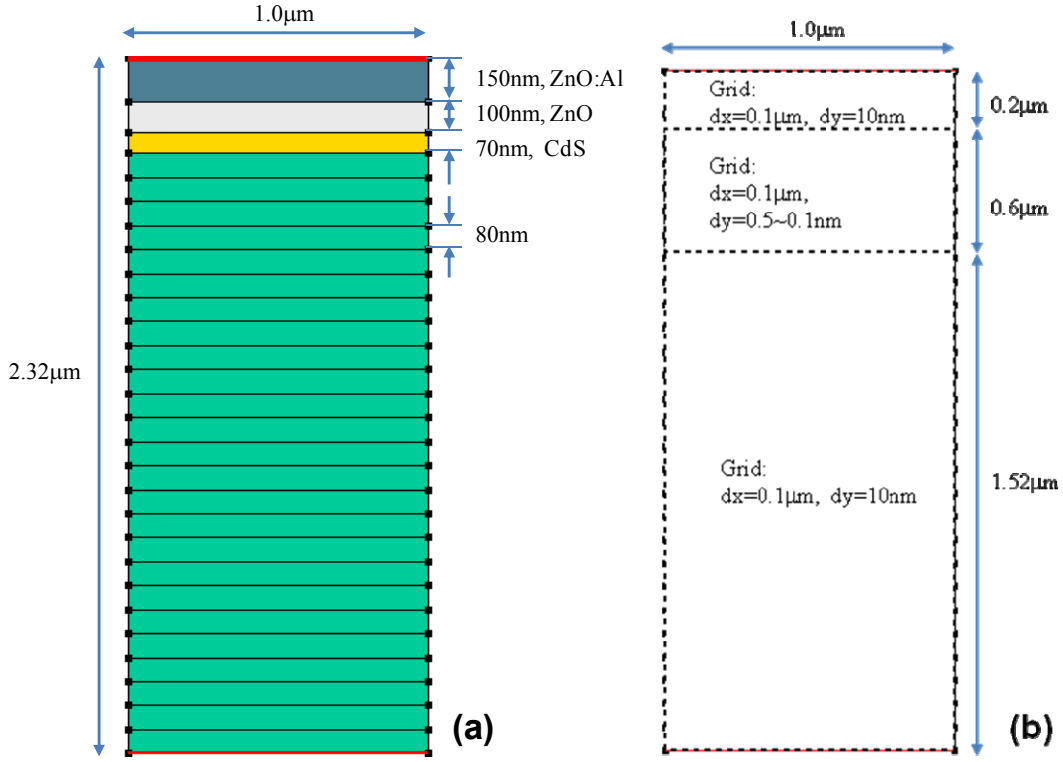


Figure A2.1. (a) Device structure and (b) grids for simulation.

A2.2. Optical parameters.

A2.2.1 AM 1.5 solar spectrum.

*Intensity unit: W/cm$^2$-nm

| λ [nm] | Intensity | λ [nm] | Intensity | λ [nm] | Intensity | λ [nm] | Intensity |
|---|---|---|---|---|---|---|---|
| 281.5 | 7.52E-22 | 367.0 | 1.77E-04 | 527.0 | 7.58E-04 | 935.0 | 8.11E-04 |
| 283.0 | 1.01E-19 | 370.0 | 2.13E-04 | 533.0 | 9.32E-04 | 953.0 | 6.19E-04 |
| 285.0 | 3.04E-17 | 372.5 | 1.57E-04 | 539.0 | 9.10E-04 | 972.0 | 9.92E-04 |
| 286.5 | 2.26E-15 | 375.5 | 1.88E-04 | 545.0 | 9.25E-04 | 992.0 | 1.39E-03 |

| | | | | | | | |
|---|---|---|---|---|---|---|---|
| 288.0 | 9.01E-14 | 378.5 | 2.30E-04 | 551.0 | 9.25E-04 | 1012.0 | 1.45E-03 |
| 290.0 | 5.52E-12 | 381.5 | 1.94E-04 | 557.0 | 9.09E-04 | 1033.0 | 1.46E-03 |
| 291.5 | 5.91E-11 | 384.0 | 1.39E-04 | 563.0 | 9.07E-04 | 1055.0 | 1.45E-03 |
| 293.0 | 5.09E-10 | 387.5 | 2.25E-04 | 570.0 | 1.04E-03 | 1078.0 | 1.41E-03 |
| 295.0 | 6.35E-09 | 390.5 | 2.41E-04 | 576.0 | 8.91E-04 | 1102.0 | 1.30E-03 |
| 297.0 | 3.94E-08 | 393.5 | 1.75E-04 | 583.0 | 1.07E-03 | 1127.0 | 5.86E-04 |
| 298.5 | 1.02E-07 | 396.5 | 2.03E-04 | 590.0 | 1.01E-03 | 1153.0 | 5.05E-04 |
| 300.5 | 3.92E-07 | 400.0 | 5.58E-04 | 597.0 | 1.02E-03 | 1180.0 | 1.08E-03 |
| 302.0 | 8.66E-07 | 403.0 | 3.47E-04 | 604.0 | 1.03E-03 | 1209.0 | 1.26E-03 |
| 304.0 | 2.59E-06 | 406.0 | 3.43E-04 | 612.0 | 1.17E-03 | 1240.0 | 1.42E-03 |
| 306.0 | 4.74E-06 | 409.0 | 3.46E-04 | 620.0 | 1.16E-03 | 1271.0 | 1.30E-03 |
| 308.0 | 7.96E-06 | 413.0 | 4.86E-04 | 627.0 | 9.84E-04 | 1305.0 | 1.35E-03 |
| 310.0 | 1.32E-05 | 416.0 | 3.65E-04 | 635.0 | 1.14E-03 | 1340.0 | 8.69E-04 |
| 311.5 | 1.44E-05 | 420.0 | 4.88E-04 | 644.0 | 1.30E-03 | 1377.0 | 4.12E-05 |
| 313.5 | 2.40E-05 | 423.0 | 3.68E-04 | 652.0 | 1.12E-03 | 1417.0 | 1.10E-05 |
| 315.5 | 2.73E-05 | 427.0 | 4.50E-04 | 661.0 | 1.21E-03 | 1458.0 | 2.12E-04 |
| 317.5 | 3.66E-05 | 431.0 | 4.35E-04 | 670.0 | 1.27E-03 | 1503.0 | 5.96E-04 |
| 320.0 | 5.59E-05 | 435.0 | 5.18E-04 | 679.0 | 1.26E-03 | 1550.0 | 1.24E-03 |
| 322.0 | 4.47E-05 | 438.0 | 3.80E-04 | 688.0 | 1.12E-03 | 1600.0 | 1.25E-03 |
| 324.0 | 5.62E-05 | 442.0 | 5.68E-04 | 698.0 | 1.28E-03 | 1653.0 | 1.22E-03 |
| 326.0 | 7.70E-05 | 446.0 | 5.79E-04 | 708.0 | 1.30E-03 | 1710.0 | 1.40E-03 |
| 328.0 | 7.86E-05 | 450.0 | 6.19E-04 | 718.0 | 1.17E-03 | 1770.0 | 8.77E-04 |
| 330.5 | 1.09E-04 | 455.0 | 7.70E-04 | 729.0 | 1.21E-03 | 1835.0 | 1.18E-04 |
| 332.5 | 8.51E-05 | 459.0 | 6.23E-04 | 740.0 | 1.33E-03 | 1905.0 | 3.87E-07 |
| 335.0 | 1.09E-04 | 463.0 | 6.27E-04 | 751.0 | 1.36E-03 | 1980.0 | 2.49E-04 |
| 337.0 | 8.14E-05 | 467.0 | 6.16E-04 | 763.0 | 9.85E-04 | 2065.0 | 5.41E-04 |
| 339.5 | 1.20E-04 | 472.0 | 7.83E-04 | 775.0 | 1.36E-03 | 2155.0 | 7.88E-04 |
| 342.0 | 1.23E-04 | 476.0 | 6.36E-04 | 787.0 | 1.38E-03 | 2250.0 | 7.12E-04 |
| 344.0 | 8.84E-05 | 481.0 | 8.05E-04 | 800.0 | 1.42E-03 | 2360.0 | 6.09E-04 |
| 346.5 | 1.21E-04 | 486.0 | 7.32E-04 | 813.0 | 1.33E-03 | 2480.0 | 3.22E-04 |
| 349.0 | 1.24E-04 | 491.0 | 7.76E-04 | 826.0 | 1.16E-03 | 2610.0 | 6.59E-06 |
| 351.5 | 1.32E-04 | 496.0 | 7.91E-04 | 840.0 | 1.36E-03 | 2755.0 | 2.55E-19 |
| 354.0 | 1.48E-04 | 501.0 | 7.61E-04 | 855.0 | 1.45E-03 | 2915.0 | 8.01E-06 |
| 356.5 | 1.25E-04 | 506.0 | 7.79E-04 | 870.0 | 1.44E-03 | 3100.0 | 6.81E-05 |
| 359.0 | 1.27E-04 | 511.0 | 7.80E-04 | 885.0 | 1.40E-03 | 3305.0 | 9.65E-05 |
| 362.0 | 1.66E-04 | 516.0 | 7.22E-04 | 901.0 | 1.25E-03 | 3540.0 | 2.11E-04 |
| 364.5 | 1.59E-04 | 522.0 | 9.18E-04 | 918.0 | 1.17E-03 | 3815.0 | 2.62E-04 |
| | | | | | | 4000.0 | 1.29E-04 |

A2.2.2 n-k values of materials.

| λ | x=0.00 | | x=0.05 | | x=0.10 | | x=0.15 | |
|---|---|---|---|---|---|---|---|---|
| [nm] | n | k | n | k | n | k | n | k |
| 269.57 | 2.84 | 1.276 | 2.83 | 1.277 | 2.82 | 1.279 | 2.80 | 1.281 |
| 275.56 | 2.77 | 1.178 | 2.76 | 1.183 | 2.75 | 1.189 | 2.74 | 1.194 |
| 281.82 | 2.71 | 1.099 | 2.71 | 1.107 | 2.70 | 1.116 | 2.70 | 1.125 |
| 288.37 | 2.66 | 1.037 | 2.66 | 1.049 | 2.66 | 1.060 | 2.66 | 1.072 |
| 295.24 | 2.62 | 0.995 | 2.63 | 1.009 | 2.63 | 1.022 | 2.63 | 1.036 |
| 302.44 | 2.60 | 0.970 | 2.60 | 0.986 | 2.60 | 1.002 | 2.60 | 1.018 |
| 310.00 | 2.58 | 0.964 | 2.58 | 0.981 | 2.59 | 0.999 | 2.59 | 1.016 |
| 317.95 | 2.57 | 0.976 | 2.57 | 0.995 | 2.58 | 1.013 | 2.59 | 1.032 |
| 326.32 | 2.57 | 1.006 | 2.58 | 1.026 | 2.58 | 1.045 | 2.59 | 1.065 |
| 335.14 | 2.58 | 1.055 | 2.59 | 1.075 | 2.60 | 1.095 | 2.60 | 1.112 |
| 344.44 | 2.61 | 1.051 | 2.61 | 1.080 | 2.62 | 1.091 | 2.63 | 1.090 |
| 354.29 | 2.62 | 1.039 | 2.62 | 1.070 | 2.62 | 1.082 | 2.63 | 1.082 |
| 364.71 | 2.61 | 1.042 | 2.62 | 1.073 | 2.62 | 1.087 | 2.63 | 1.088 |
| 375.76 | 2.63 | 1.059 | 2.64 | 1.091 | 2.65 | 1.106 | 2.65 | 1.107 |
| 387.50 | 2.68 | 1.090 | 2.69 | 1.124 | 2.69 | 1.138 | 2.70 | 1.141 |
| 400.00 | 2.76 | 1.136 | 2.76 | 1.170 | 2.77 | 1.185 | 2.78 | 1.188 |
| 413.33 | 2.86 | 1.196 | 2.87 | 1.205 | 2.87 | 1.183 | 2.88 | 1.161 |
| 427.59 | 3.00 | 1.066 | 3.00 | 1.048 | 3.00 | 1.030 | 3.00 | 1.012 |
| 442.86 | 3.16 | 0.930 | 3.14 | 0.915 | 3.12 | 0.900 | 3.11 | 0.885 |
| 459.26 | 3.13 | 0.816 | 3.13 | 0.804 | 3.13 | 0.792 | 3.13 | 0.780 |
| 476.92 | 3.09 | 0.722 | 3.09 | 0.713 | 3.09 | 0.703 | 3.09 | 0.694 |
| 496.00 | 3.06 | 0.645 | 3.06 | 0.639 | 3.06 | 0.632 | 3.06 | 0.624 |
| 516.67 | 3.04 | 0.584 | 3.04 | 0.580 | 3.04 | 0.575 | 3.04 | 0.569 |
| 539.13 | 3.02 | 0.536 | 3.02 | 0.533 | 3.02 | 0.530 | 3.02 | 0.526 |
| 563.64 | 3.00 | 0.499 | 3.00 | 0.498 | 3.00 | 0.496 | 3.00 | 0.493 |
| 590.48 | 2.99 | 0.471 | 2.99 | 0.470 | 2.99 | 0.469 | 2.99 | 0.468 |
| 620.00 | 2.98 | 0.449 | 2.98 | 0.449 | 2.98 | 0.449 | 2.98 | 0.448 |
| 635.90 | 2.97 | 0.439 | 2.97 | 0.440 | 2.97 | 0.440 | 2.97 | 0.440 |
| 652.63 | 2.97 | 0.431 | 2.97 | 0.432 | 2.97 | 0.432 | 2.97 | 0.432 |
| 670.27 | 2.97 | 0.423 | 2.97 | 0.424 | 2.97 | 0.425 | 2.97 | 0.424 |
| 688.89 | 2.97 | 0.415 | 2.97 | 0.417 | 2.97 | 0.417 | 2.97 | 0.416 |
| 708.57 | 2.97 | 0.407 | 2.97 | 0.409 | 2.97 | 0.409 | 2.97 | 0.408 |
| 729.41 | 2.97 | 0.398 | 2.97 | 0.401 | 2.97 | 0.401 | 2.97 | 0.400 |

| | | | | | | | | |
|---|---|---|---|---|---|---|---|---|
| 751.52 | 2.97 | 0.389 | 2.97 | 0.392 | 2.97 | 0.392 | 2.97 | 0.390 |
| 775.00 | 2.98 | 0.379 | 2.98 | 0.382 | 2.98 | 0.382 | 2.98 | 0.380 |
| 800.00 | 2.98 | 0.368 | 2.98 | 0.370 | 2.98 | 0.370 | 2.98 | 0.368 |
| 826.67 | 2.98 | 0.355 | 2.98 | 0.358 | 2.98 | 0.358 | 2.98 | 0.355 |
| 855.17 | 2.99 | 0.341 | 2.99 | 0.343 | 2.99 | 0.343 | 2.99 | 0.339 |
| 885.71 | 3.00 | 0.324 | 3.00 | 0.326 | 3.00 | 0.326 | 3.00 | 0.322 |
| 918.52 | 3.01 | 0.305 | 3.01 | 0.307 | 3.01 | 0.306 | 3.01 | 0.301 |
| 953.85 | 3.01 | 0.283 | 3.01 | 0.286 | 3.01 | 0.284 | 3.01 | 0.279 |
| 992.00 | 3.02 | 0.259 | 3.02 | 0.261 | 3.02 | 0.259 | 3.02 | 0.253 |
| 1033.33 | 3.04 | 0.231 | 3.04 | 0.233 | 3.04 | 0.231 | 3.04 | 0.223 |
| 1078.26 | 3.05 | 0.200 | 3.05 | 0.202 | 3.05 | 0.199 | 3.05 | 0.190 |
| 1127.27 | 3.06 | 0.165 | 3.06 | 0.167 | 3.06 | 0.163 | 3.05 | 0.153 |
| 1180.95 | 3.07 | 0.126 | 3.05 | 0.128 | 3.03 | 0.123 | 3.00 | 0.113 |
| 1240.00 | 3.02 | 0.082 | 3.00 | 0.084 | 2.98 | 0.079 | 2.97 | 6.71E-02 |
| 1305.26 | 2.98 | 0.034 | 2.96 | 3.61E-02 | 2.95 | 3.03E-02 | 2.93 | 1.70E-02 |
| 1377.78 | 2.94 | 6.54E-03 | 2.93 | 6.78E-03 | 2.92 | 5.83E-03 | 2.90 | 4.16E-03 |
| 1458.82 | 2.92 | 1.72E-03 | 2.91 | 1.78E-03 | 2.89 | 1.50E-03 | 2.88 | 1.04E-03 |
| 1550.00 | 2.90 | 3.98E-04 | 2.89 | 4.11E-04 | 2.88 | 3.41E-04 | 2.87 | 2.27E-04 |
| 1653.33 | 2.89 | 8.07E-05 | 2.88 | 8.33E-05 | 2.87 | 6.77E-05 | 2.86 | 4.35E-05 |

| λ | x=0.20 | | x=0.25 | | x=0.30 | | x=0.35 | |
|---|---|---|---|---|---|---|---|---|
| [nm] | n | k | n | k | n | k | n | k |
| 269.57 | 2.79 | 1.283 | 2.77 | 1.285 | 2.76 | 1.287 | 2.79 | 1.290 |
| 275.56 | 2.73 | 1.200 | 2.72 | 1.205 | 2.71 | 1.211 | 2.74 | 1.222 |
| 281.82 | 2.69 | 1.133 | 2.69 | 1.142 | 2.68 | 1.151 | 2.70 | 1.168 |
| 288.37 | 2.66 | 1.084 | 2.65 | 1.095 | 2.65 | 1.107 | 2.67 | 1.130 |
| 295.24 | 2.63 | 1.050 | 2.63 | 1.064 | 2.63 | 1.078 | 2.65 | 1.106 |
| 302.44 | 2.61 | 1.034 | 2.61 | 1.050 | 2.61 | 1.066 | 2.64 | 1.097 |
| 310.00 | 2.60 | 1.034 | 2.60 | 1.051 | 2.61 | 1.069 | 2.63 | 1.104 |
| 317.95 | 2.59 | 1.051 | 2.60 | 1.069 | 2.61 | 1.088 | 2.64 | 1.119 |
| 326.32 | 2.60 | 1.084 | 2.60 | 1.104 | 2.61 | 1.104 | 2.65 | 1.080 |
| 335.14 | 2.61 | 1.101 | 2.62 | 1.088 | 2.62 | 1.073 | 2.67 | 1.054 |
| 344.44 | 2.63 | 1.081 | 2.64 | 1.068 | 2.64 | 1.056 | 2.66 | 1.041 |
| 354.29 | 2.63 | 1.074 | 2.63 | 1.063 | 2.63 | 1.052 | 2.66 | 1.042 |
| 364.71 | 2.63 | 1.081 | 2.63 | 1.071 | 2.64 | 1.062 | 2.67 | 1.055 |
| 375.76 | 2.66 | 1.102 | 2.66 | 1.093 | 2.67 | 1.085 | 2.71 | 1.082 |
| 387.50 | 2.71 | 1.136 | 2.71 | 1.128 | 2.72 | 1.121 | 2.78 | 1.122 |
| 400.00 | 2.78 | 1.184 | 2.79 | 1.177 | 2.79 | 1.171 | 2.86 | 1.175 |
| 413.33 | 2.88 | 1.140 | 2.88 | 1.118 | 2.89 | 1.098 | 2.97 | 1.057 |

| | | | | | | | | |
|---|---|---|---|---|---|---|---|---|
| 427.59 | 3.00 | 0.994 | 2.99 | 0.976 | 2.98 | 0.958 | 3.11 | 0.923 |
| 442.86 | 3.09 | 0.871 | 3.07 | 0.856 | 3.05 | 0.841 | 3.16 | 0.811 |
| 459.26 | 3.13 | 0.768 | 3.13 | 0.756 | 3.13 | 0.744 | 3.13 | 0.719 |
| 476.92 | 3.09 | 0.684 | 3.09 | 0.675 | 3.09 | 0.665 | 3.09 | 0.644 |
| 496.00 | 3.06 | 0.617 | 3.06 | 0.609 | 3.06 | 0.601 | 3.06 | 0.584 |
| 516.67 | 3.04 | 0.564 | 3.04 | 0.557 | 3.04 | 0.551 | 3.04 | 0.538 |
| 539.13 | 3.02 | 0.522 | 3.02 | 0.517 | 3.02 | 0.512 | 3.02 | 0.501 |
| 563.64 | 3.00 | 0.490 | 3.00 | 0.486 | 3.00 | 0.482 | 3.00 | 0.472 |
| 590.48 | 2.99 | 0.465 | 2.99 | 0.462 | 2.99 | 0.459 | 2.99 | 0.450 |
| 620.00 | 2.98 | 0.446 | 2.98 | 0.443 | 2.98 | 0.440 | 2.98 | 0.430 |
| 635.90 | 2.97 | 0.438 | 2.97 | 0.435 | 2.97 | 0.431 | 2.97 | 0.421 |
| 652.63 | 2.97 | 0.430 | 2.97 | 0.427 | 2.97 | 0.423 | 2.97 | 0.412 |
| 670.27 | 2.97 | 0.422 | 2.97 | 0.419 | 2.97 | 0.414 | 2.97 | 0.402 |
| 688.89 | 2.97 | 0.414 | 2.97 | 0.411 | 2.97 | 0.406 | 2.97 | 0.392 |
| 708.57 | 2.97 | 0.406 | 2.97 | 0.402 | 2.97 | 0.396 | 2.97 | 0.381 |
| 729.41 | 2.97 | 0.397 | 2.97 | 0.392 | 2.97 | 0.386 | 2.97 | 0.368 |
| 751.52 | 2.97 | 0.387 | 2.97 | 0.382 | 2.97 | 0.375 | 2.97 | 0.354 |
| 775.00 | 2.98 | 0.376 | 2.98 | 0.370 | 2.98 | 0.362 | 2.98 | 0.339 |
| 800.00 | 2.98 | 0.364 | 2.98 | 0.356 | 2.98 | 0.347 | 2.98 | 0.321 |
| 826.67 | 2.98 | 0.349 | 2.98 | 0.341 | 2.98 | 0.330 | 2.98 | 0.301 |
| 855.17 | 2.99 | 0.333 | 2.99 | 0.324 | 2.99 | 0.311 | 2.99 | 0.278 |
| 885.71 | 3.00 | 0.314 | 3.00 | 0.304 | 3.00 | 0.290 | 3.00 | 0.252 |
| 918.52 | 3.01 | 0.293 | 3.01 | 0.281 | 3.01 | 0.265 | 3.01 | 0.223 |
| 953.85 | 3.01 | 0.269 | 3.01 | 0.255 | 3.01 | 0.238 | 3.01 | 0.191 |
| 992.00 | 3.02 | 0.242 | 3.02 | 0.226 | 3.02 | 0.207 | 3.02 | 0.154 |
| 1033.33 | 3.04 | 0.211 | 3.04 | 0.194 | 3.04 | 0.172 | 3.01 | 0.114 |
| 1078.26 | 3.05 | 0.177 | 3.05 | 0.157 | 3.02 | 0.133 | 2.97 | 0.069 |
| 1127.27 | 3.03 | 0.138 | 3.00 | 0.117 | 2.98 | 0.090 | 2.93 | 0.019 |
| 1180.95 | 2.98 | 0.095 | 2.96 | 0.072 | 2.94 | 0.042 | 2.90 | 0.004 |
| 1240.00 | 2.95 | 0.048 | 2.93 | 0.022 | 2.91 | 0.008 | 2.88 | 1.09E-03 |
| 1305.26 | 2.92 | 0.009 | 2.90 | 4.78E-03 | 2.88 | 2.10E-03 | 2.85 | 2.41E-04 |
| 1377.78 | 2.89 | 2.46E-03 | 2.88 | 1.21E-03 | 2.86 | 4.90E-04 | 2.84 | 4.63E-05 |
| 1458.82 | 2.87 | 5.83E-04 | 2.86 | 2.68E-04 | 2.85 | 1.01E-04 | 2.82 | 7.71E-06 |
| 1550.00 | 2.86 | 1.21E-04 | 2.85 | 5.21E-05 | 2.83 | 1.80E-05 | 2.81 | 1.11E-06 |
| 1653.33 | 2.85 | 2.20E-05 | 2.84 | 8.81E-06 | 2.83 | 2.78E-06 | 2.81 | 1.36E-07 |

| λ | x=0.40 | | x=0.45 | | x=0.50 | | x=0.55 | |
|---|---|---|---|---|---|---|---|---|
| [nm] | n | k | n | k | n | k | n | k |
| 269.57 | 2.79 | 1.290 | 2.78 | 1.292 | 2.77 | 1.294 | 2.77 | 1.296 |

| | | | | | | | | |
|---|---|---|---|---|---|---|---|---|
| 275.56 | 2.74 | 1.222 | 2.74 | 1.227 | 2.73 | 1.233 | 2.73 | 1.238 |
| 281.82 | 2.70 | 1.168 | 2.70 | 1.177 | 2.70 | 1.186 | 2.69 | 1.194 |
| 288.37 | 2.67 | 1.130 | 2.67 | 1.141 | 2.67 | 1.153 | 2.67 | 1.164 |
| 295.24 | 2.65 | 1.106 | 2.66 | 1.120 | 2.66 | 1.134 | 2.66 | 1.148 |
| 302.44 | 2.64 | 1.097 | 2.65 | 1.113 | 2.65 | 1.129 | 2.66 | 1.145 |
| 310.00 | 2.63 | 1.104 | 2.65 | 1.121 | 2.66 | 1.139 | 2.67 | 1.150 |
| 317.95 | 2.64 | 1.119 | 2.65 | 1.110 | 2.67 | 1.107 | 2.69 | 1.110 |
| 326.32 | 2.65 | 1.080 | 2.67 | 1.075 | 2.69 | 1.075 | 2.72 | 1.082 |
| 335.14 | 2.67 | 1.054 | 2.69 | 1.052 | 2.69 | 1.056 | 2.70 | 1.067 |
| 344.44 | 2.66 | 1.041 | 2.67 | 1.042 | 2.67 | 1.050 | 2.68 | 1.064 |
| 354.29 | 2.66 | 1.042 | 2.67 | 1.045 | 2.68 | 1.057 | 2.69 | 1.075 |
| 364.71 | 2.67 | 1.055 | 2.69 | 1.062 | 2.71 | 1.076 | 2.72 | 1.098 |
| 375.76 | 2.71 | 1.082 | 2.74 | 1.091 | 2.76 | 1.108 | 2.78 | 1.134 |
| 387.50 | 2.78 | 1.122 | 2.81 | 1.133 | 2.84 | 1.153 | 2.87 | 1.182 |
| 400.00 | 2.86 | 1.175 | 2.90 | 1.188 | 2.94 | 1.171 | 2.98 | 1.149 |
| 413.33 | 2.97 | 1.057 | 3.02 | 1.037 | 3.07 | 1.018 | 3.11 | 0.998 |
| 427.59 | 3.11 | 0.923 | 3.16 | 0.906 | 3.20 | 0.888 | 3.20 | 0.871 |
| 442.86 | 3.16 | 0.811 | 3.16 | 0.796 | 3.16 | 0.781 | 3.16 | 0.767 |
| 459.26 | 3.13 | 0.719 | 3.13 | 0.706 | 3.13 | 0.694 | 3.13 | 0.681 |
| 476.92 | 3.09 | 0.644 | 3.09 | 0.634 | 3.09 | 0.623 | 3.09 | 0.612 |
| 496.00 | 3.06 | 0.584 | 3.06 | 0.576 | 3.06 | 0.567 | 3.06 | 0.557 |
| 516.67 | 3.04 | 0.538 | 3.04 | 0.530 | 3.04 | 0.523 | 3.04 | 0.515 |
| 539.13 | 3.02 | 0.501 | 3.02 | 0.495 | 3.02 | 0.488 | 3.02 | 0.481 |
| 563.64 | 3.00 | 0.472 | 3.00 | 0.467 | 3.00 | 0.460 | 3.00 | 0.454 |
| 590.48 | 2.99 | 0.450 | 2.99 | 0.444 | 2.99 | 0.438 | 2.99 | 0.431 |
| 620.00 | 2.98 | 0.430 | 2.98 | 0.424 | 2.98 | 0.417 | 2.98 | 0.409 |
| 635.90 | 2.97 | 0.421 | 2.97 | 0.414 | 2.97 | 0.407 | 2.97 | 0.398 |
| 652.63 | 2.97 | 0.412 | 2.97 | 0.404 | 2.97 | 0.396 | 2.97 | 0.387 |
| 670.27 | 2.97 | 0.402 | 2.97 | 0.394 | 2.97 | 0.385 | 2.97 | 0.375 |
| 688.89 | 2.97 | 0.392 | 2.97 | 0.383 | 2.97 | 0.373 | 2.97 | 0.361 |
| 708.57 | 2.97 | 0.381 | 2.97 | 0.371 | 2.97 | 0.359 | 2.97 | 0.346 |
| 729.41 | 2.97 | 0.368 | 2.97 | 0.357 | 2.97 | 0.344 | 2.97 | 0.329 |
| 751.52 | 2.97 | 0.354 | 2.97 | 0.342 | 2.97 | 0.327 | 2.97 | 0.310 |
| 775.00 | 2.98 | 0.339 | 2.98 | 0.324 | 2.98 | 0.307 | 2.98 | 0.288 |
| 800.00 | 2.98 | 0.321 | 2.98 | 0.304 | 2.98 | 0.286 | 2.98 | 0.264 |
| 826.67 | 2.98 | 0.301 | 2.98 | 0.282 | 2.98 | 0.261 | 2.98 | 0.237 |
| 855.17 | 2.99 | 0.278 | 2.99 | 0.257 | 2.99 | 0.233 | 2.99 | 0.206 |
| 885.71 | 3.00 | 0.252 | 3.00 | 0.229 | 3.00 | 0.202 | 3.00 | 0.172 |
| 918.52 | 3.01 | 0.223 | 3.01 | 0.197 | 3.01 | 0.167 | 3.01 | 0.133 |

| | | | | | | | | |
|---|---|---|---|---|---|---|---|---|
| 953.85 | 3.01 | 0.191 | 3.01 | 0.161 | 3.01 | 0.128 | 2.98 | 0.090 |
| 992.00 | 3.02 | 0.154 | 3.02 | 0.121 | 2.98 | 0.084 | 2.95 | 0.043 |
| 1033.33 | 3.01 | 0.114 | 2.98 | 0.077 | 2.95 | 0.036 | 2.92 | 0.008 |
| 1078.26 | 2.97 | 0.069 | 2.94 | 0.028 | 2.91 | 0.007 | 2.89 | 0.002 |
| 1127.27 | 2.93 | 0.019 | 2.91 | 0.006 | 2.89 | 0.002 | 2.86 | 0.000 |
| 1180.95 | 2.90 | 0.004 | 2.88 | 0.001 | 2.86 | 0.000 | 2.84 | 0.000 |
| 1240.00 | 2.88 | 0.001 | 2.86 | 0.000 | 2.84 | 0.000 | 2.82 | 1.71E-05 |
| 1305.26 | 2.85 | 0.000 | 2.84 | 6.30E-05 | 2.82 | 1.39E-05 | 2.81 | 2.57E-06 |
| 1377.78 | 2.84 | 4.63E-05 | 2.82 | 1.07E-05 | 2.81 | 2.06E-06 | 2.79 | 3.29E-07 |
| 1458.82 | 2.82 | 7.71E-06 | 2.81 | 1.57E-06 | 2.80 | 2.63E-07 | 2.79 | 3.57E-08 |
| 1550.00 | 2.81 | 1.11E-06 | 2.80 | 1.98E-07 | 2.79 | 2.83E-08 | 2.78 | 3.26E-09 |
| 1653.33 | 2.81 | 1.36E-07 | 2.80 | 2.11E-08 | 2.79 | 2.58E-09 | 2.78 | 2.49E-10 |

| λ | x=0.60 | | x=0.65 | | x=0.70 | | x=0.75 | |
|---|---|---|---|---|---|---|---|---|
| [nm] | n | k | n | k | n | k | n | k |
| 269.57 | 2.76 | 1.298 | 2.75 | 1.299 | 2.74 | 1.301 | 2.74 | 1.303 |
| 275.56 | 2.72 | 1.244 | 2.71 | 1.249 | 2.71 | 1.255 | 2.70 | 1.260 |
| 281.82 | 2.69 | 1.203 | 2.69 | 1.212 | 2.68 | 1.220 | 2.68 | 1.229 |
| 288.37 | 2.67 | 1.176 | 2.67 | 1.187 | 2.67 | 1.199 | 2.67 | 1.210 |
| 295.24 | 2.67 | 1.162 | 2.67 | 1.176 | 2.67 | 1.190 | 2.67 | 1.203 |
| 302.44 | 2.67 | 1.161 | 2.68 | 1.177 | 2.68 | 1.193 | 2.69 | 1.209 |
| 310.00 | 2.68 | 1.154 | 2.69 | 1.162 | 2.71 | 1.173 | 2.72 | 1.186 |
| 317.95 | 2.71 | 1.117 | 2.72 | 1.129 | 2.74 | 1.144 | 2.76 | 1.160 |
| 326.32 | 2.74 | 1.094 | 2.73 | 1.110 | 2.73 | 1.129 | 2.73 | 1.148 |
| 335.14 | 2.70 | 1.083 | 2.70 | 1.104 | 2.70 | 1.127 | 2.70 | 1.149 |
| 344.44 | 2.68 | 1.085 | 2.69 | 1.110 | 2.70 | 1.138 | 2.70 | 1.165 |
| 354.29 | 2.70 | 1.100 | 2.71 | 1.129 | 2.72 | 1.162 | 2.73 | 1.194 |
| 364.71 | 2.74 | 1.127 | 2.75 | 1.161 | 2.77 | 1.199 | 2.79 | 1.237 |
| 375.76 | 2.80 | 1.167 | 2.83 | 1.206 | 2.85 | 1.250 | 2.87 | 1.294 |
| 387.50 | 2.90 | 1.219 | 2.93 | 1.264 | 2.96 | 1.261 | 2.99 | 1.241 |
| 400.00 | 3.02 | 1.128 | 3.06 | 1.108 | 3.09 | 1.088 | 3.13 | 1.069 |
| 413.33 | 3.16 | 0.979 | 3.21 | 0.961 | 3.25 | 0.942 | 3.26 | 0.924 |
| 427.59 | 3.20 | 0.855 | 3.20 | 0.838 | 3.21 | 0.821 | 3.22 | 0.805 |
| 442.86 | 3.16 | 0.752 | 3.16 | 0.737 | 3.17 | 0.722 | 3.18 | 0.707 |
| 459.26 | 3.13 | 0.668 | 3.13 | 0.655 | 3.13 | 0.642 | 3.14 | 0.629 |
| 476.92 | 3.09 | 0.601 | 3.09 | 0.590 | 3.10 | 0.578 | 3.11 | 0.567 |
| 496.00 | 3.06 | 0.548 | 3.06 | 0.538 | 3.07 | 0.528 | 3.08 | 0.518 |
| 516.67 | 3.04 | 0.506 | 3.04 | 0.498 | 3.04 | 0.489 | 3.05 | 0.479 |
| 539.13 | 3.02 | 0.473 | 3.02 | 0.465 | 3.02 | 0.457 | 3.03 | 0.448 |

| | | | | | | | | |
|---|---|---|---|---|---|---|---|---|
| 563.64 | 3.00 | 0.446 | 3.00 | 0.439 | 3.01 | 0.430 | 3.01 | 0.421 |
| 590.48 | 2.99 | 0.423 | 2.99 | 0.415 | 2.99 | 0.406 | 3.00 | 0.396 |
| 620.00 | 2.98 | 0.401 | 2.98 | 0.391 | 2.98 | 0.381 | 2.99 | 0.370 |
| 635.90 | 2.97 | 0.389 | 2.97 | 0.379 | 2.98 | 0.367 | 2.99 | 0.355 |
| 652.63 | 2.97 | 0.377 | 2.97 | 0.365 | 2.98 | 0.353 | 2.99 | 0.339 |
| 670.27 | 2.97 | 0.363 | 2.97 | 0.350 | 2.98 | 0.336 | 2.99 | 0.321 |
| 688.89 | 2.97 | 0.348 | 2.97 | 0.334 | 2.98 | 0.318 | 2.99 | 0.301 |
| 708.57 | 2.97 | 0.331 | 2.97 | 0.315 | 2.98 | 0.298 | 2.99 | 0.278 |
| 729.41 | 2.97 | 0.313 | 2.97 | 0.294 | 2.98 | 0.274 | 2.99 | 0.253 |
| 751.52 | 2.97 | 0.291 | 2.97 | 0.271 | 2.98 | 0.248 | 2.99 | 0.224 |
| 775.00 | 2.98 | 0.267 | 2.98 | 0.244 | 2.99 | 0.219 | 3.00 | 0.192 |
| 800.00 | 2.98 | 0.241 | 2.98 | 0.214 | 2.99 | 0.186 | 3.00 | 0.155 |
| 826.67 | 2.98 | 0.210 | 2.98 | 0.181 | 3.00 | 0.149 | 2.99 | 0.114 |
| 855.17 | 2.99 | 0.176 | 2.99 | 0.143 | 2.97 | 0.108 | 2.96 | 0.069 |
| 885.71 | 3.00 | 0.138 | 2.96 | 0.101 | 2.94 | 0.061 | 2.93 | 0.018 |
| 918.52 | 2.98 | 0.096 | 2.93 | 0.055 | 2.91 | 0.010 | 2.90 | 0.004 |
| 953.85 | 2.94 | 0.049 | 2.90 | 0.011 | 2.89 | 0.003 | 2.88 | 0.001 |
| 992.00 | 2.91 | 0.009 | 2.88 | 0.003 | 2.86 | 0.001 | 2.85 | 0.000 |
| 1033.33 | 2.88 | 0.002 | 2.85 | 0.001 | 2.84 | 0.000 | 2.83 | 0.000 |
| 1078.26 | 2.86 | 0.001 | 2.83 | 0.000 | 2.82 | 0.000 | 2.82 | 0.000 |
| 1127.27 | 2.84 | 0.000 | 2.81 | 0.000 | 2.81 | 0.000 | 2.80 | 0.000 |
| 1180.95 | 2.82 | 0.000 | 2.80 | 0.000 | 2.79 | 0.000 | 2.79 | 0.000 |
| 1240.00 | 2.80 | 0.000 | 2.79 | 0.000 | 2.78 | 0.000 | 2.78 | 7.27E-09 |
| 1305.26 | 2.79 | 0.000 | 2.77 | 5.26E-08 | 2.77 | 5.81E-09 | 2.77 | 5.40E-10 |
| 1377.78 | 2.78 | 4.36E-08 | 2.77 | 4.78E-09 | 2.76 | 4.35E-10 | 2.76 | 3.28E-11 |
| 1458.82 | 2.77 | 3.97E-09 | 2.76 | 3.60E-10 | 2.76 | 2.67E-11 | 2.76 | 1.61E-12 |
| 1550.00 | 2.77 | 3.02E-10 | 2.76 | 2.24E-11 | 2.76 | 1.34E-12 | 2.75 | 6.39E-14 |
| 1653.33 | 2.77 | 1.89E-11 | 2.76 | 1.14E-12 | 2.76 | 5.39E-14 | 2.75 | 2.02E-15 |

| λ | x=0.80 | | x=0.85 | | x=0.90 | | x=0.95 | |
|---|---|---|---|---|---|---|---|---|
| [nm] | n | k | n | k | n | k | n | k |
| 269.57 | 2.73 | 1.305 | 2.72 | 1.307 | 2.71 | 1.309 | 2.71 | 1.311 |
| 275.56 | 2.70 | 1.266 | 2.69 | 1.271 | 2.69 | 1.276 | 2.68 | 1.282 |
| 281.82 | 2.68 | 1.238 | 2.67 | 1.246 | 2.67 | 1.255 | 2.67 | 1.264 |
| 288.37 | 2.67 | 1.222 | 2.67 | 1.233 | 2.67 | 1.245 | 2.67 | 1.256 |
| 295.24 | 2.68 | 1.217 | 2.68 | 1.231 | 2.68 | 1.245 | 2.69 | 1.259 |
| 302.44 | 2.70 | 1.225 | 2.70 | 1.241 | 2.71 | 1.257 | 2.72 | 1.265 |
| 310.00 | 2.73 | 1.199 | 2.74 | 1.209 | 2.75 | 1.213 | 2.76 | 1.208 |
| 317.95 | 2.77 | 1.174 | 2.78 | 1.183 | 2.77 | 1.184 | 2.77 | 1.171 |

| | | | | | | | | |
|---|---|---|---|---|---|---|---|---|
| 326.32 | 2.73 | 1.164 | 2.73 | 1.174 | 2.72 | 1.173 | 2.72 | 1.157 |
| 335.14 | 2.70 | 1.169 | 2.70 | 1.181 | 2.71 | 1.180 | 2.71 | 1.163 |
| 344.44 | 2.71 | 1.188 | 2.71 | 1.204 | 2.72 | 1.207 | 2.72 | 1.191 |
| 354.29 | 2.74 | 1.223 | 2.75 | 1.244 | 2.76 | 1.252 | 2.77 | 1.241 |
| 364.71 | 2.80 | 1.272 | 2.82 | 1.300 | 2.84 | 1.315 | 2.85 | 1.311 |
| 375.76 | 2.90 | 1.337 | 2.92 | 1.373 | 2.94 | 1.388 | 2.97 | 1.371 |
| 387.50 | 3.02 | 1.221 | 3.05 | 1.202 | 3.08 | 1.184 | 3.11 | 1.167 |
| 400.00 | 3.17 | 1.050 | 3.21 | 1.031 | 3.25 | 1.014 | 3.29 | 0.996 |
| 413.33 | 3.27 | 0.906 | 3.28 | 0.889 | 3.29 | 0.872 | 3.30 | 0.855 |
| 427.59 | 3.23 | 0.788 | 3.23 | 0.772 | 3.24 | 0.756 | 3.25 | 0.740 |
| 442.86 | 3.18 | 0.693 | 3.19 | 0.678 | 3.20 | 0.663 | 3.21 | 0.648 |
| 459.26 | 3.15 | 0.616 | 3.15 | 0.602 | 3.16 | 0.589 | 3.17 | 0.576 |
| 476.92 | 3.11 | 0.555 | 3.12 | 0.543 | 3.13 | 0.531 | 3.13 | 0.519 |
| 496.00 | 3.08 | 0.507 | 3.09 | 0.497 | 3.10 | 0.486 | 3.11 | 0.474 |
| 516.67 | 3.06 | 0.470 | 3.07 | 0.460 | 3.07 | 0.449 | 3.08 | 0.439 |
| 539.13 | 3.04 | 0.439 | 3.05 | 0.429 | 3.05 | 0.419 | 3.06 | 0.409 |
| 563.64 | 3.02 | 0.412 | 3.03 | 0.402 | 3.04 | 0.392 | 3.04 | 0.381 |
| 590.48 | 3.01 | 0.386 | 3.02 | 0.375 | 3.02 | 0.364 | 3.03 | 0.351 |
| 620.00 | 3.00 | 0.358 | 3.01 | 0.345 | 3.02 | 0.331 | 3.03 | 0.317 |
| 635.90 | 3.00 | 0.342 | 3.01 | 0.328 | 3.02 | 0.313 | 3.02 | 0.297 |
| 652.63 | 3.00 | 0.324 | 3.01 | 0.309 | 3.01 | 0.292 | 3.02 | 0.274 |
| 670.27 | 3.00 | 0.305 | 3.01 | 0.287 | 3.01 | 0.268 | 3.02 | 0.248 |
| 688.89 | 3.00 | 0.283 | 3.01 | 0.263 | 3.02 | 0.242 | 3.03 | 0.219 |
| 708.57 | 3.00 | 0.258 | 3.01 | 0.235 | 3.02 | 0.212 | 3.03 | 0.187 |
| 729.41 | 3.00 | 0.230 | 3.01 | 0.205 | 3.02 | 0.178 | 3.03 | 0.149 |
| 751.52 | 3.00 | 0.198 | 3.02 | 0.170 | 3.03 | 0.140 | 3.00 | 0.108 |
| 775.00 | 3.01 | 0.162 | 3.02 | 0.130 | 3.00 | 0.097 | 2.98 | 0.061 |
| 800.00 | 3.01 | 0.122 | 2.99 | 0.086 | 2.97 | 0.048 | 2.95 | 0.012 |
| 826.67 | 2.97 | 0.077 | 2.96 | 0.037 | 2.94 | 0.009 | 2.92 | 0.003 |
| 855.17 | 2.94 | 0.027 | 2.93 | 0.007 | 2.91 | 0.002 | 2.90 | 0.001 |
| 885.71 | 2.92 | 0.005 | 2.90 | 0.002 | 2.89 | 0.000 | 2.88 | 0.000 |
| 918.52 | 2.89 | 0.001 | 2.88 | 0.000 | 2.87 | 0.000 | 2.86 | 0.000 |
| 953.85 | 2.87 | 0.000 | 2.86 | 0.000 | 2.85 | 0.000 | 2.84 | 0.000 |
| 992.00 | 2.85 | 0.000 | 2.84 | 0.000 | 2.83 | 0.000 | 2.82 | 0.000 |
| 1033.33 | 2.83 | 0.000 | 2.82 | 0.000 | 2.81 | 0.000 | 2.81 | 0.000 |
| 1078.26 | 2.81 | 0.000 | 2.80 | 0.000 | 2.80 | 0.000 | 2.79 | 0.000 |
| 1127.27 | 2.80 | 0.000 | 2.79 | 0.000 | 2.79 | 0.000 | 2.78 | 0.000 |
| 1180.95 | 2.78 | 0.000 | 2.78 | 0.000 | 2.77 | 0.000 | 2.77 | 0.000 |
| 1240.00 | 2.77 | 0.000 | 2.77 | 0.000 | 2.77 | 0.000 | 2.76 | 2.44E-13 |

| | | | | | | | | |
|---|---|---|---|---|---|---|---|---|
| 1305.26 | 2.76 | 0.000 | 2.76 | 2.78E-12 | 2.76 | 1.54E-13 | 2.75 | 7.19E-15 |
| 1377.78 | 2.76 | 2.05E-12 | 2.75 | 1.06E-13 | 2.75 | 4.58E-15 | 2.75 | 1.63E-16 |
| 1458.82 | 2.75 | 7.97E-14 | 2.75 | 3.21E-15 | 2.75 | 1.06E-16 | 2.75 | 2.84E-18 |
| 1550.00 | 2.75 | 2.46E-15 | 2.75 | 7.59E-17 | 2.75 | 1.88E-18 | 2.74 | 3.74E-20 |
| 1653.33 | 2.75 | 5.95E-17 | 2.75 | 1.39E-18 | 2.75 | 2.55E-20 | 2.74 | 3.70E-22 |

| λ | x=1.00 | | AZO/ZnO | | CdS | |
|---|---|---|---|---|---|---|
| [nm] | n | k | n | k | n | k |
| 269.57 | 2.70 | 1.312 | 1.77 | 0.429 | 2.78 | 0.436 |
| 275.56 | 2.67 | 1.287 | 1.80 | 0.439 | 2.74 | 0.439 |
| 281.82 | 2.66 | 1.273 | 1.83 | 0.449 | 2.71 | 0.442 |
| 288.37 | 2.67 | 1.268 | 1.85 | 0.459 | 2.68 | 0.445 |
| 295.24 | 2.69 | 1.273 | 1.88 | 0.470 | 2.66 | 0.448 |
| 302.44 | 2.73 | 1.260 | 1.91 | 0.481 | 2.63 | 0.451 |
| 310.00 | 2.78 | 1.188 | 1.93 | 0.493 | 2.61 | 0.454 |
| 317.95 | 2.76 | 1.141 | 1.96 | 0.506 | 2.59 | 0.457 |
| 326.32 | 2.72 | 1.119 | 1.98 | 0.519 | 2.58 | 0.460 |
| 335.14 | 2.71 | 1.123 | 2.01 | 0.533 | 2.56 | 0.462 |
| 344.44 | 2.73 | 1.151 | 2.02 | 0.548 | 2.55 | 0.464 |
| 354.29 | 2.78 | 1.204 | 2.10 | 0.564 | 2.54 | 0.466 |
| 364.71 | 2.87 | 1.283 | 2.22 | 0.031 | 2.54 | 0.467 |
| 375.76 | 2.99 | 1.356 | 2.41 | 2.53E-05 | 2.54 | 0.468 |
| 387.50 | 3.14 | 1.151 | 2.33 | 2.06E-08 | 2.54 | 0.468 |
| 400.00 | 3.33 | 0.979 | 2.26 | 1.68E-11 | 2.55 | 0.466 |
| 413.33 | 3.31 | 0.839 | 2.21 | 1.37E-14 | 2.56 | 0.464 |
| 427.59 | 3.26 | 0.725 | 2.17 | 1.12E-17 | 2.57 | 0.459 |
| 442.86 | 3.22 | 0.634 | 2.14 | 9.20E-21 | 2.59 | 0.450 |
| 459.26 | 3.18 | 0.562 | 2.11 | 7.54E-24 | 2.60 | 0.437 |
| 476.92 | 3.14 | 0.506 | 2.09 | 6.19E-27 | 2.62 | 0.415 |
| 496.00 | 3.11 | 0.463 | 2.07 | 5.09E-30 | 2.70 | 0.363 |
| 516.67 | 3.09 | 0.428 | 2.05 | 4.19E-33 | 2.77 | 1.08E-03 |
| 539.13 | 3.07 | 0.398 | 2.03 | 3.46E-36 | 2.68 | 8.95E-07 |
| 563.64 | 3.05 | 0.369 | 2.02 | 2.86E-39 | 2.59 | 7.40E-10 |
| 590.48 | 3.04 | 0.338 | 2.01 | 2.36E-42 | 2.50 | 6.12E-13 |
| 620.00 | 3.03 | 0.302 | 1.99 | 1.96E-45 | 2.47 | 5.08E-16 |
| 635.90 | 3.03 | 0.280 | 1.99 | 5.66E-47 | 2.45 | 1.47E-17 |
| 652.63 | 3.03 | 0.255 | 1.99 | 1.63E-48 | 2.44 | 4.23E-19 |
| 670.27 | 3.03 | 0.227 | 1.98 | 4.72E-50 | 2.42 | 1.22E-20 |
| 688.89 | 3.04 | 0.196 | 1.98 | 1.36E-51 | 2.41 | 3.53E-22 |

| | | | | | | |
|---|---|---|---|---|---|---|
| 708.57 | 3.04 | 0.160 | 1.97 | 3.94E-53 | 2.40 | 1.02E-23 |
| 729.41 | 3.01 | 0.119 | 1.97 | 1.14E-54 | 2.39 | 2.95E-25 |
| 751.52 | 2.98 | 0.074 | 1.97 | 3.30E-56 | 2.38 | 8.56E-27 |
| 775.00 | 2.95 | 0.023 | 1.96 | 9.58E-58 | 2.37 | 2.48E-28 |
| 800.00 | 2.93 | 4.50E-03 | 1.96 | 2.78E-59 | 2.36 | 7.20E-30 |
| 826.67 | 2.91 | 1.04E-03 | 1.96 | 8.08E-61 | 2.35 | 2.09E-31 |
| 855.17 | 2.88 | 2.05E-04 | 1.95 | 2.35E-62 | 2.35 | 6.09E-33 |
| 885.71 | 2.86 | 3.40E-05 | 1.95 | 6.84E-64 | 2.34 | 1.77E-34 |
| 918.52 | 2.85 | 4.72E-06 | 1.95 | 1.99E-65 | 2.34 | 5.17E-36 |
| 953.85 | 2.83 | 5.42E-07 | 1.95 | 5.82E-67 | 2.33 | 1.51E-37 |
| 992.00 | 2.81 | 5.08E-08 | 1.94 | 1.70E-68 | 2.33 | 4.41E-39 |
| 1033.33 | 2.80 | 3.86E-09 | 1.94 | 4.99E-70 | 2.33 | 1.29E-40 |
| 1078.26 | 2.79 | 2.34E-10 | 1.94 | 1.46E-71 | 2.33 | 3.79E-42 |
| 1127.27 | 2.78 | 1.13E-11 | 1.94 | 4.30E-73 | 2.33 | 1.11E-43 |
| 1180.95 | 2.77 | 4.27E-13 | 1.94 | 1.27E-74 | 2.33 | 3.28E-45 |
| 1240.00 | 2.76 | 1.25E-14 | 1.93 | 3.74E-76 | 2.33 | 9.69E-47 |
| 1305.26 | 2.75 | 2.82E-16 | 1.93 | 1.11E-77 | 2.33 | 2.87E-48 |
| 1377.78 | 2.75 | 4.84E-18 | 1.93 | 3.29E-79 | 2.33 | 8.51E-50 |
| 1458.82 | 2.74 | 6.24E-20 | 1.93 | 9.78E-81 | 2.32 | 2.53E-51 |
| 1550.00 | 2.74 | 5.98E-22 | 1.93 | 2.92E-82 | 2.32 | 7.57E-53 |
| 1653.33 | 2.74 | 4.23E-24 | 1.93 | 8.76E-84 | 2.32 | 2.27E-54 |

**References**


[1] Y. Zohta, Solid-State Electronics 16 (1973) 1029-1035.

[2] Y. Zohta, J. Appl. Phys. 43 (1972) 1713–1716.